Brushless Self-Excited Synchronous Field-Winding Machine With Five- and Higher-Phase Design Using Independently Controlled Spatial Harmonics

by

Jake Sungwoo Chung

A dissertation submitted in partial fulfillment
of the requirements for the degree of
Doctor of Philosophy
(Electrical and Computer Engineering)
in the University of Michigan
2023

Doctoral Committee:

Professor Heath Hofmann, Chair
Professor Al-Thaddeus Avestruz
Professor Bogdan Epureanu
Professor Ian Hiskens

Jake Sungwoo Chung

jswchung@umich.edu

ORCID iD: 0000-0002-1530-1071

TABLE OF CONTENTS

LIST OF FIGURES

LIST OF TABLES

TABLE

ABSTRACT

Electric machines used in a variety of sustainable energy applications need to possess high power density, high efficiency, and low manufacturing cost. While permanent-magnet machines and synchronous field-winding machines are the popular option for variable-speed drives, these topologies have undesirable aspects. The magnets in permanent-magnet machines are typically made of rare-earth materials which have high price volatility and are prone to demagnetization, risking machine operation. The synchronous field-winding machines require additional electrical and mechanical components requiring regular maintenance and replacement and add extra volume, weight, and cost to the drive system.

In this dissertation, a novel brushless self-excitation scheme for synchronous field-winding machines is presented. This scheme uses an AC stator with five or higher phases to create two independently controlled rotating magnetic fields at different spatial harmonics, allowing independent magnetic coupling with different rotor windings. The rotor of the proposed machine possesses a field winding, transformer windings, and a diode rectifier that converts induced AC voltages in the transformer windings into a DC voltage for the field winding. A design for a five-phase stator configuration is developed using finite-element analysis tools, and simulation results are presented. Torque and power characteristics of the design are compared with similarly-sized interior permanent-magnet and induction machines.

CHAPTER 1

Introduction

1.1 Review on Relevant Concepts and Theories

1.1.1 On Electric Machines

The importance of clean and sustainable energy is widely appreciated in modern industry over the last decade. Electric machines, as one way to accelerate this transition, are actively researched and used in wide applications to replace devices that use fossil fuels. These applications range from brushless DC motors used in small electronics such as CD drives, servomotors, and actuators for industrial robots to induction or permanent magnet machines used for electric vehicles, ship propulsion, construction machines, and heating, ventilation, and air conditioning (HVAC) applications.

There are two types of electric machines depending on the motion of the mechanical system. Linear or translational machines have a moving part the so-called "mover" that has one-directional movement. Applications for linear motors include industrial automation equipment, machine tools, etc. Rotational machines are another type of electric machine, where the movement of the rotating part (rotor) is periodic and continuous. Such characteristics make rotational machines widely used in electric vehicles, wind turbines, etc. Considering their relevance, we will be focusing on rotating machines.

An electric machine can be defined as an energy conversion device or an electromechanical device because it is capable of converting energies between electrical power and mechanical power,
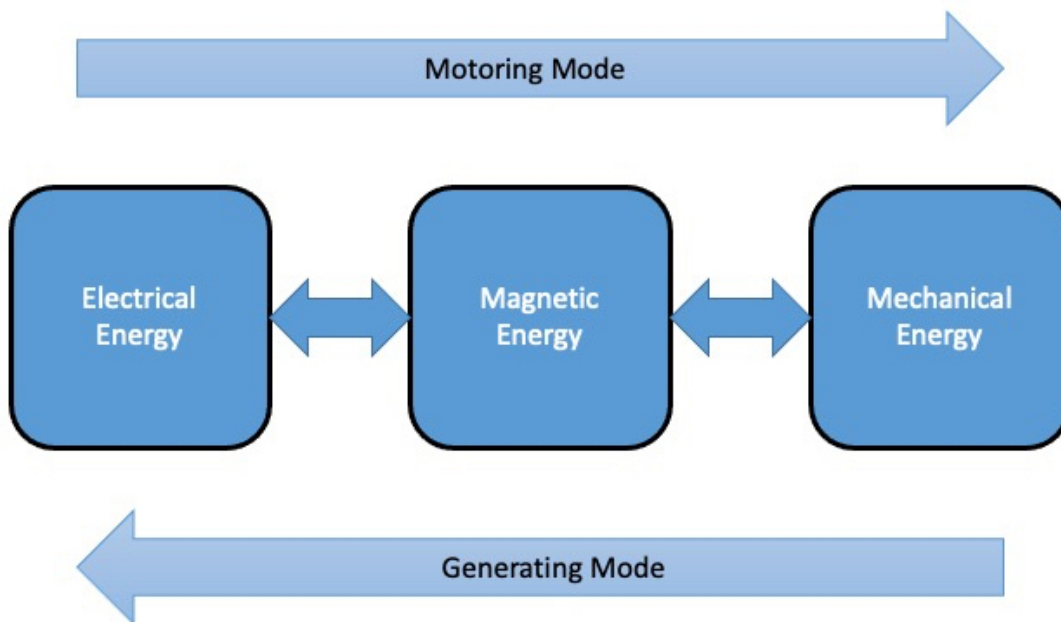
Figure 1.1: Energy conversions of an electromechanical device

as shown in Figure 1.1. For example, an electric motor in vehicles generates motion and acceler-ates the vehicle by transforming the electrical energy from a battery pack to mechanical energy. This type of energy conversion is referred to as the motoring mode. On the other hand, when an electric vehicle reduces speed, the electric motor changes its operating mode and converts the ki-netic energy from the vehicle motion back to electrical energy which is then stored in the battery. This type of energy conversion is referred to as the generating (or alternating) mode [1].

Electric machines were first introduced around 1821 by British scientist Michael Faraday, who built a primitive motor using stiff wire in a container of mercury and a permanent magnet [2]. Since then, electric machines have evolved for many decades following improvements in power electronic devices, and various types of motors have been invented to expand their usage in many industrial fields. Until the 1950s, induction motors, invented by Nikola Tesla in 1887, were the main type of electric motor. However, these motors operated only at a relatively constant speed due to the lack of variable-speed drives at that time. When transistors were invented around 1947, Sigma Instruments introduced the Cyclonome Stepping Motor in 1952 which became the main-
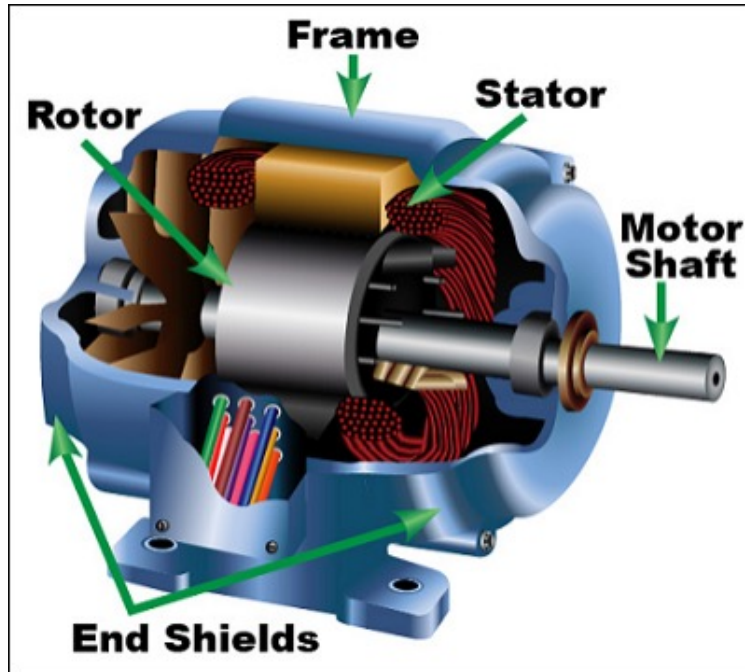
Figure 1.2: Electric machine structure [4]

stream electric motor for low-power applications [3]. The first DC motors and stepper motors that could be operated at variable speeds were realized with the invention of power thyristors in 1957. These power thyristors allowed the development of high-power DC machines which expanded their application. In the late 1970s, AC permanent-magnet (PM) and induction machines (IM) gained popularity and became viable alternatives to DC machines thanks to the Darlington transistor module used for high-power inverters. Since then, both AC PMs and IMs are widely used until the present day due to their increased efficiency and reduced costs.

Rotational AC machines are generally constructed with two parts: a stator and a rotor. Figure 1.2 shows a conventional AC machine structure where the rotor is located inside the stator. The stator is a stationary part where electrical wires are typically wound to provide electrical power to the machine through an inverter. The rotor is a rotating part connected to a shaft with bearings at the center point and couples with the external loads to transfer mechanical power. Both the stator and rotor are typically made of highly permeable grade electrical steels so that applied magnetic fields produced by the stator windings can be excited efficiently.
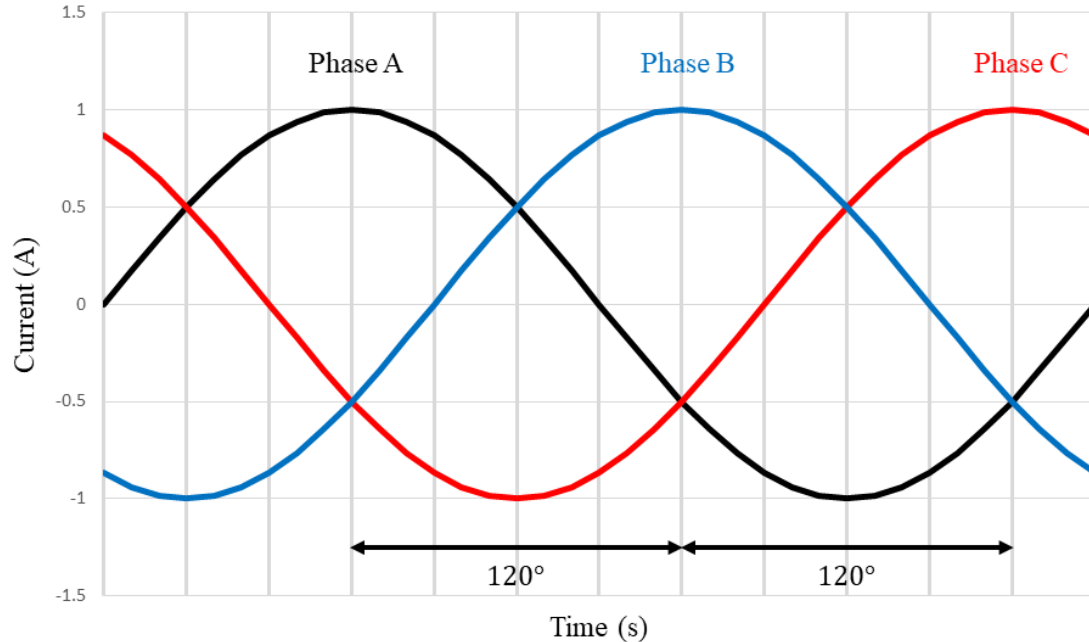
Figure 1.3: Balanced three-phase currents

Conventional AC machines regardless of different typologies have a three-phase stator design. Although a two-phase AC stator configuration is feasible, the three-phase machine has several advantages over the two-phase design. The primary reason is the fact that the three-phase config- uration can make the AC phase currents such that the sum of balanced, steady-state three-phase currents becomes always zero. Figure 1.3 shows that the balanced three-phase currents that are 120 degrees out of phase result in the cancellation of currents. This inherent characteristic of the three-phase stator makes a single neutral possible using a wye connection as shown in Figure 1.4. Therefore, the three-phase stator winding requires only three electrical terminals whereas the two- phase winding requires four terminals. Moreover, this makes the three-phase machine need three half-bridges instead of four half-bridges, making the overall electric drive system simple and less expensive. For those reasons, the three-phase winding configuration has become the most used stator design in most electric machine topologies.

What differentiates various electric machine topologies is the design of the rotor as shown in Figure 1.5. Each topology has its own merits and drawbacks based upon different requirements of performance and applications.

4
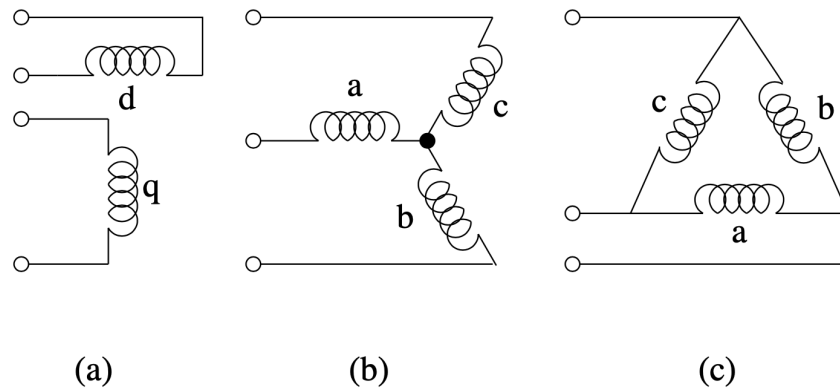
Figure 1.4: Phase-winding connections: (a) Two-phase, (b) three-phase ungrounded-wye configuration, and (c) three-phase delta configuration electrical connections [5]

The IM is one of the widely used electric machines because of its relatively simple structures and low costs. The rotor of this machine topology can be constructed with either wound electrical wires in the rotor slots or a squirrel-cage design with a cylinder of steel laminations and embedded conductors on its surface. The rotor is excited when voltages are induced in the rotor conductors by the stator phase currents and relative motion created between the stator and rotor. Hence, the machine has an asynchronous nature of operation, and it is capable of operating over a wide speed range. In general, the IMs have relatively low manufacturing costs when compared to other machine topologies. However, the IMs suffer from relatively low power density and poor power factor as power decreases at high speeds [6].

The reluctance machine (RM) is a type of electric machine that exploits a built-in magnetic saliency of the rotor. The rotor of the RMs does not have electrical conductors. Instead, it has a salient rotor structure as shown in Figure 1.5-(b). Because of a lack of electrical conductors in the rotor, there is no conduction (i.e., I^2R) loss in the rotor of this machine type which benefits its efficiency aspect. Using the saliency of the rotor, controls of the stator magnetic flux become relatively simple making the operation over a wide speed range possible. However, the RMs have relatively low power density, low power factor, and relatively high manufacturing costs, making this machine type less common than IMs [7].

5
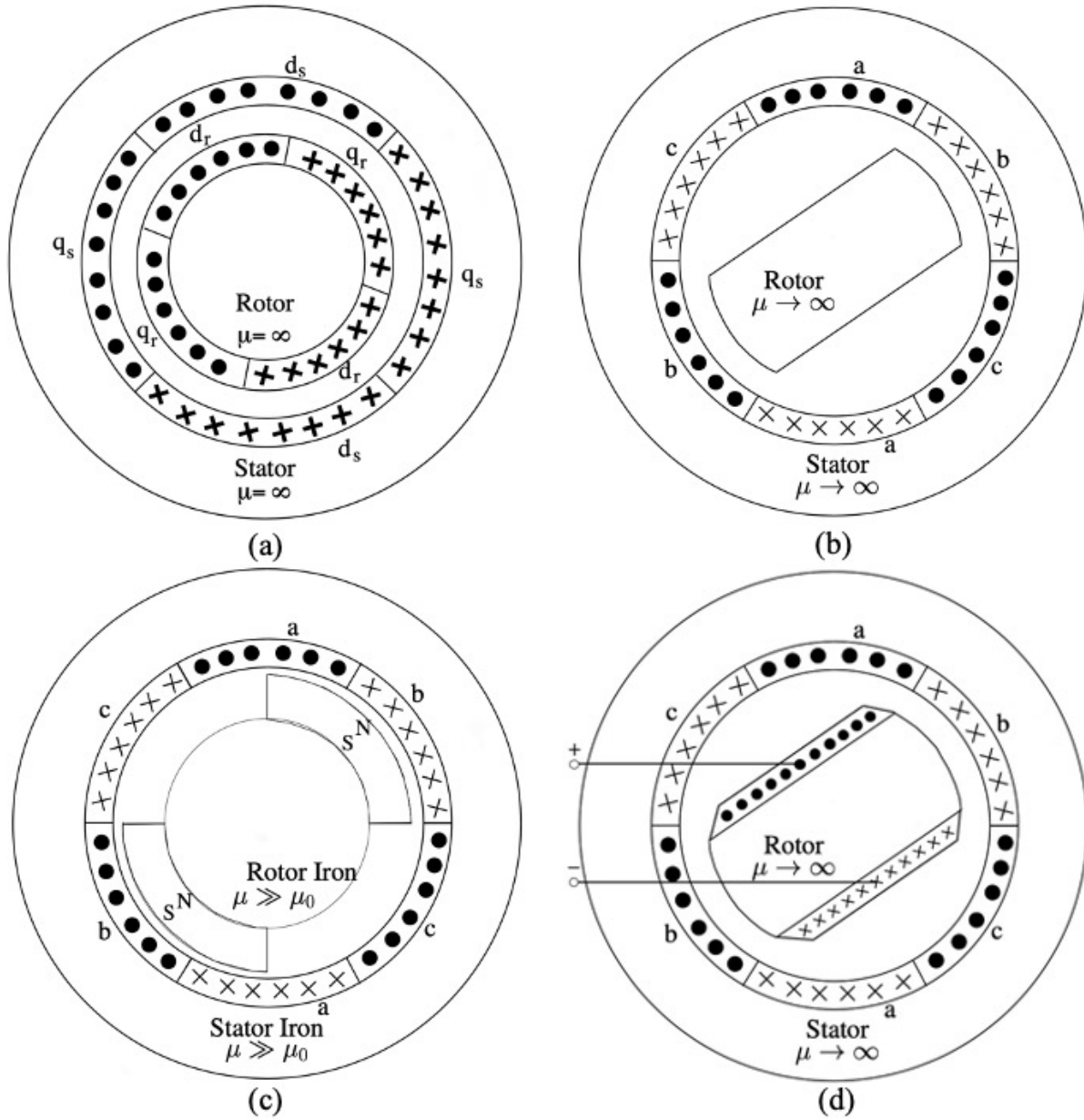
Figure 1.5: AC electric machine topologies: (a) Induction, (b) Synchronous reluctance, (c) Permanent magnet (Surface-mounted), and (d) Synchronous field winding machines [5]

The synchronous field-winding machine (SFM) is another type of synchronous machine that possesses high torque density and independent magnetic excitation in the rotor. The standard rotor of this machine type has field coils which are powered by a dedicated DC power supply provided through additional mechanical parts brushes and slip rings. Basically, the SFM utilizes a DC electromagnet to generate a magnetic field instead of the permanent magnet for the PMs. A main advantage of the field-winding machine is that the rotor field is controllable by the separate power supply. Hence, it provides a degree of freedom in control of the rotor field over a wide speed range. By utilizing the capability of independent magnetic excitation of the rotor, the SFMs can achieve high power density, unity power factor, and CPWSR similar to the PMs. However, the need for an additional power supply and mechanical components to excite the field winding in the rotor becomes a main disadvantage of this machine type [8].

The PM is a synchronous machine that is widely used in applications that require high power density and high efficiency. The rotor of this machine type has permanent magnets that are either mounted on the rotor surface or located inside the rotor iron. The major advantage of the magnets in the rotor is their ability to produce magnetic fields without an additional power source. Hence, there is no conduction loss in the rotor which increases overall efficiency. Unlike SFMs, a dedicated DC supply and mechanical connections using brushes and slip rings are not needed to generate the rotor fields. Moreover, this machine type is capable of producing constant power above the base speed of the machine under the imposed voltage and current constraints. However, the costs of the magnets used for this machine type are becoming more expensive and volatile because they are made of rare-earth materials. Recently, the high price volatility increases interest in the development of alternative electric machine topologies [9].

The four fundamental electric machine topologies can be combined in various ways to create superior electric machines. For example, the interior permanent-magnet machine (IPM) is an electric machine type based on RM and PM topologies. The IPMs have magnets embedded inside the rotor iron which creates a magnetic saliency. This allows the IPMs to achieve better torque capability because of the addition of the reluctance torque from the magnetic saliency on top of the

7

permanent-magnet torque from the independent magnetic excitation [5].

1.1.2   On Electric Drives

An electric drive is an essential hardware and software package that is used to operate almost all types of electric machines in the modern industry. Before electric drives were readily available, electric motors were usually powered by an AC voltage with a fixed frequency (e.g., 60 Hz) provided by the electric utility or a DC power supply such as an electrochemical battery. Using these power sources directly to electric machines effectively results in constant speed operation which was undesirable for variable-speed drive applications. The electric drive, which is also referred to as a variable-speed drive, or VSD, was introduced with the development of power electronic devices and microcontrollers and enabled electric machines to operate over a wide range of speeds.

Electric drives in many applications provide control of electromechanical force or torque, or the position or angular velocity of the rotor of the machines. The feedback control approach is commonly used to achieve such control by measuring the stator currents and rotor position or speed through sensors attached to the machines and using them to calculate the commanded or reference voltages to achieve the desired behaviors of the machines.

In general, the electromagnetic torque of AC machines is controlled indirectly by the stator currents due to a close relationship between the torque and current. Moreover, since measuring the machine torque requires the use of a sophisticated measurement device, therefore it is much harder to measure the quantity of the torque accurately than the stator currents. In this section, we focus on a torque/current regulation of electric machines based on the field-oriented control (FOC) technique as shown in Figure 1.6.

The FOC-based current regulator of the electric drive system consists of three main subsystems: control circuitry, power electronic circuitry, and electric machines. The control circuitry or controller subsystem contains an algorithm that generates the desired voltages for the electric machine using the commanded or reference currents and the measured currents from the machine. As shown in Figure 1.6, the controller calculates error signals first using the commanded currents and the measured currents from the sensors which are then fed into the controllers. One way to implement the current regulation is to use proportional-integral (PI) feedback controllers. The PI
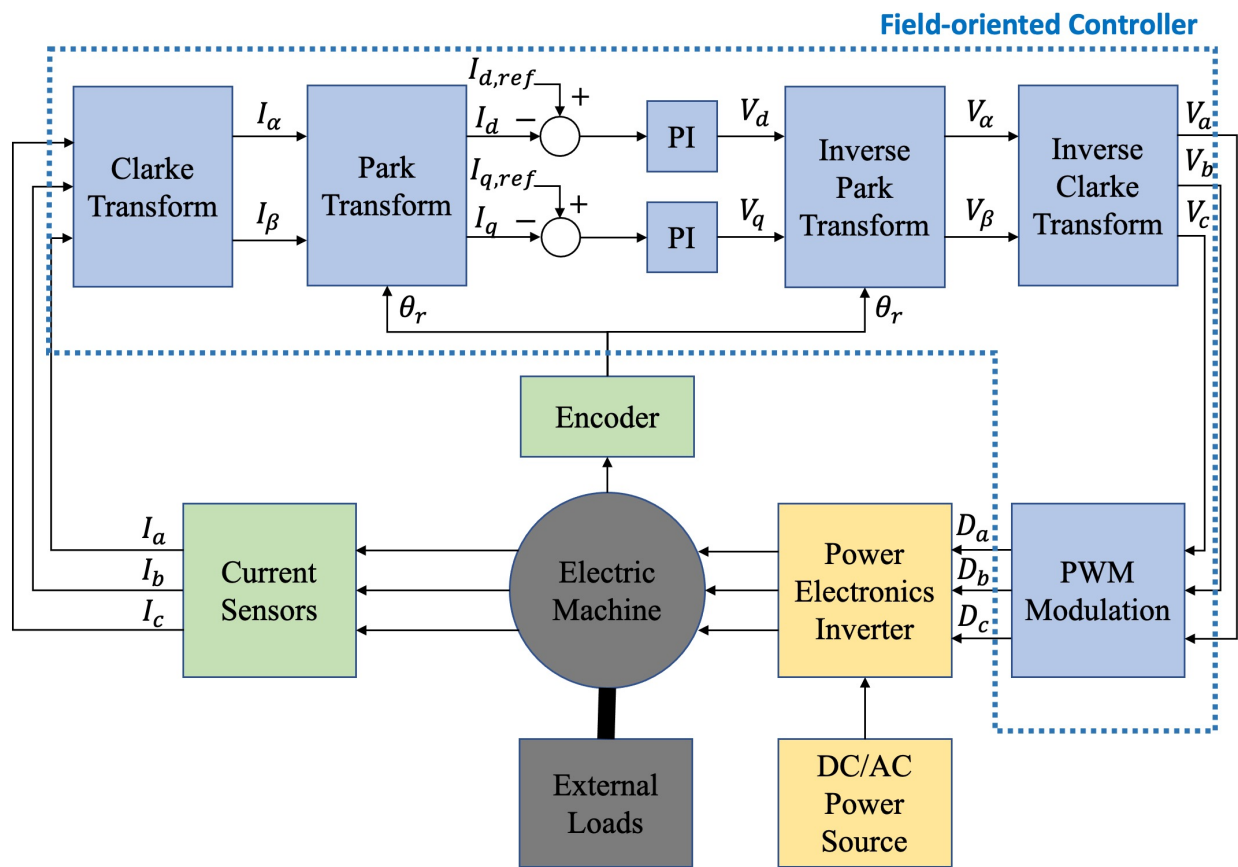
Figure 1.6: An example of torque/current regulation using FOC [5]

controller is a feedback technique that utilizes these error signals so that the closed-loop feedback system continuously adjusts the output of the controller until the measured currents of the machine track the commanded currents. In this technique, the Clarke and Park transformations convert the measured AC currents of the machine from the stationary reference frame to the synchronous reference frame. The resulting currents in the synchronous reference frame become constant in the steady-state and are used for generating the error signals. The generated commanded or reference voltages in the synchronous reference frame are then converted to the AC voltages in the stationary reference frame using the inverse Clarke and Park transformations. Finally, the PWM modulation calculates duty cycles based on the output AC voltages from the controller, which are then used in the power electronic circuitry to generate the command voltage in an average-value sense [10].

In order to achieve the control algorithm, the control subsystem requires measurement hardware (e.g., ammeter, encoder, etc). The current measurement devices are attached to either inverters or machines and measure the multi-phase stator currents for feedback control purposes. Another sensing device that may be used for some machines is an encoder or a resolver that provides the position or speed information of the rotor or shaft and is attached to the machine. In some applications, the position-sensing device can be removed for the sensorless estimation method. This position of the rotor is used not only in the reference frame transformation (e.g., the Park transformation) of the currents and voltages for the torque/current regulator in the control system but also as a reference value for the position/speed regulator. Therefore, in one approach, the position/speed regulator can be constructed with an outer mechanical loop and an inner torque loop. For such a control system, the outer mechanical loop uses the commanded and measured or estimated position or speed to generate the torque command. Then, the inner torque loop takes this commanded torque/current to generate appropriate voltages for the rest of the subsystems.

The power electronic subsystem consists of multi-phase inverters depending on the number of phases of electric machines. The multi-phase inverters are generally supplied by a DC bus voltage either directly from an electrochemical battery or converted from AC power provided by the electric utility. The inverters use the bus voltage and the duty cycles from the controller to

11
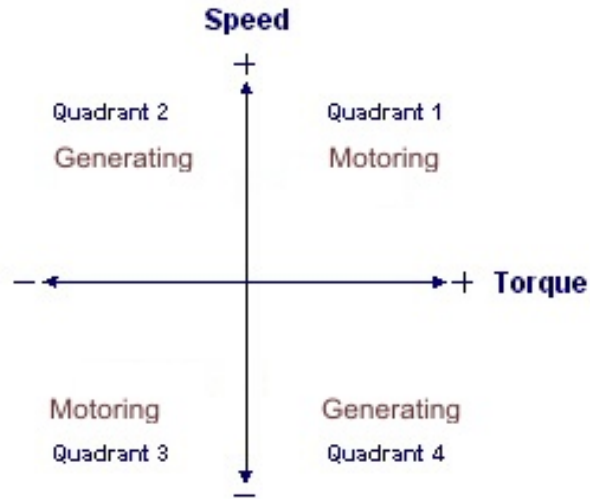
Figure 1.7: Four-quadrant operation [12]

generate desired commanded voltages in an average-value sense which are used to excite the stator winding of electric machines. Lastly, the electric machine subsystem includes the machine itself and external loads which are mechanically coupled with the main electric machine.

There are several desired features to consider when designing an electric drive system for variable-speed drive applications. The electric drive system needs to control the torque of electric machines in both clockwise and counterclockwise directions, enabling the electric machines to operate both in motoring and generating modes. This is often referred to as the "four-quadrant" operation as shown in Figure 1.7. When the motoring mode is requested, the drive system controls both the speed and torque in the same direction (Quadrants 1 and 3), which means that the electrical energy is converted to mechanical energy for the desired external loads. In contrast, when the generating mode is requested, the drive system controls the speed and torque in opposite directions (Quadrants 2 and 4), making the energy conversion occur from mechanical power to electrical power [11].

1.2 Motivation

Electric machines are an essential device in a variety of sustainable energy applications. Recent industrial applications require these machines to possess high power density, high efficiency, and low manufacturing cost. Most AC machines are based on the four fundamental AC electric machine topologies of IM, RM, PM, and SFM or variants based on combinations of these topologies (e.g., IPM).

Among the different AC machine topologies, PM and SFM stand out for variable-speed drive applications. These topologies have an independent magnetic excitation in the rotor, hence the stator and rotor magnetic fields can be controlled independently to achieve optimal operating conditions, allowing higher torque densities and power factors, unlike IM and RM. The stator voltage consists of a resistive drop component and an electromotive force (EMF) component which is a time derivative of the stator flux linkage. At sufficiently high speeds, the magnitude of the stator voltage is approximately equal to the electrical frequency of the rotor times the flux linkage magnitude, hence machines become voltage constrained. Under this condition, the stator flux linkage and the electrical frequency of the rotor have an inverse relationship, therefore the flux linkage decreases as the rotor speed increases. Since the torque of the PMs and SFMs is directly proportional to the magnitude of the stator flux linkage and also decreases, the mechanical power which is the torque times the rotor speed becomes constant above the base speed [5]. Therefore, certain PMs and SFMs have Constant Power over a Wide Speed Range (CPWSR) capability, which is a desirable feature for variable-speed drive applications [13].

Conversely, IMs and RMs have an inherent characteristic where the induced flux linkage in the rotor is restricted by the stator current and flux linkage. Under strictly flux-constrained conditions, the torque of the IMs becomes inversely proportional to the square of the rotor speed, therefore the mechanical power decreases as the rotor speed increases [5]. The qualitative power-speed characteristics of different machine topologies are shown in Fig. 1.8. It shows a clear advantage in the power capability of the PMs and SFMs for variable-speed drive applications.

Moreover, PMs and SFMs can achieve near unity power factor. Hence, the variable-speed

13
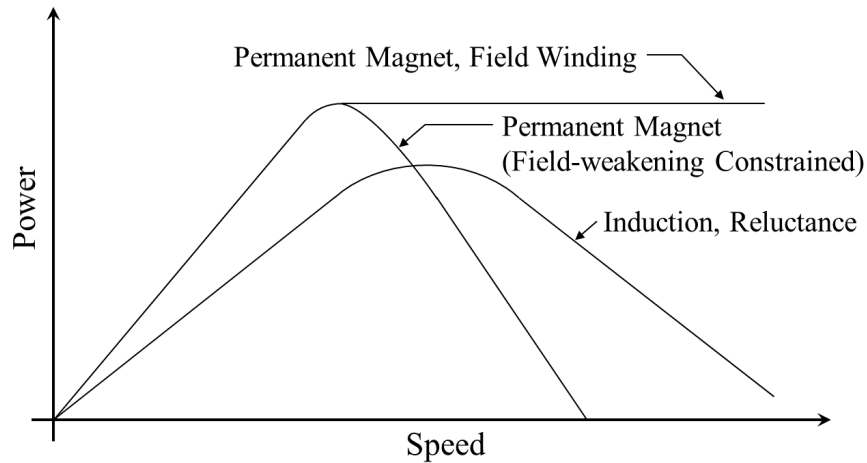
Figure 1.8: Qualitative power-speed characteristics of different machine topologies driven by same variable-speed drive with fixed output voltage, current limitations.

drive (VSD) can provide its peak power capability to the machine based on its voltage and current specifications. Conversely, it allows these machines to operate using power electronic components (e.g., transistors) with lower voltage and/or current ratings which reduce the cost of the VSD.

As a result, PMs and SFMs have been chosen for many industrial applications. In fact, the majority of traction drive systems have relied on variants of PMs because permanent magnets can produce magnetic fields in the rotor without conduction losses. In one survey, it is expected that the industrial use of permanent magnet machines is rapidly increasing and projected to grow to near 60% by 2026 [14].

Although PMs have been the topology of choice in wide applications, the use of permanent magnets creates issues from both performance and economic standpoints. Demagnetization of magnets in PMs is one issue that occurs when the permanent magnets experience extensive periods of aging, field weakening controls, high temperature, or other environmental stresses while in operation [15].

Another issue is related to the constant magnetic flux produced by permanent magnets during high-speed operations. Although producing the magnetic flux without any conduction losses in the rotor is a great advantage of the PMs, the constant rotor fields imposed on the machine at all times can damage other VSD components if the machine loses control during operation. For example,

14
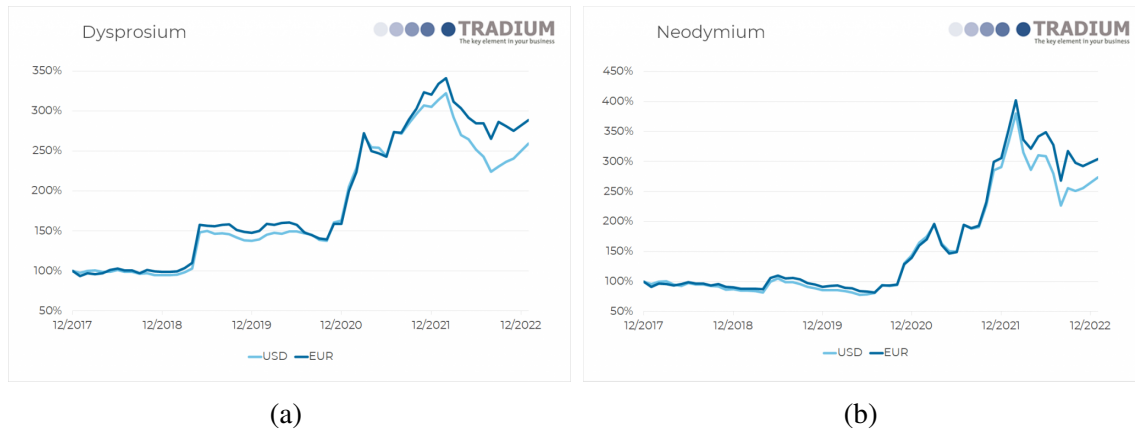
Figure 1.9: 5-year price charts of (a) Dysprosium. (b) Neodymium. [17]

when the rotor of the PMs spins above base speed, field weakening techniques are implemented by the stator currents to cancel the rotor fields generated by magnets. It is a common control scheme used so that these machines could operate at high speeds without losing their mechanical power. However, under some fault conditions (e.g., power surge), constantly generated magnetic fields and resulting electromotive forces (EMFs) by the magnets could damage connected power electronic components if the machine is uncontrolled during high-speed operation [16].

From an economic standpoint, increasing demands of permanent magnets for PMs and their applications have created price volatility of rare-earth materials due to challenges stemming from its long-term and stable supply of relevant materials. For example, the price of dysprosium and neodymium, the rare-earth materials used for PMs, have increased with high volatility for the past five years, as shown in Figure 1.9. In 2017, the price of neodymium reached $73/kg, double when compared to the previous year. More recently, its price has gone up by nearly 200% because many industries are moving toward electrification in the transportation and manufacturing fields [9]. As a result, there is increasing interest in the development of alternative electric machine topologies that do not use these magnets.

The SFM is another electric machine topology that has a similarity to PMs in that the rotor has an independent magnetic excitation through electromagnets instead of permanent magnets. This allows the SFMs to have higher torque densities and efficiencies than induction machines.

For example, under assumptions of linear magnetic behavior, the SFMs can produce up to 30% higher torque than the IMs for a given amount of I^2R losses or conduction losses in the stator and rotor [5]. Conversely, the SFMs can generate up to 30% fewer conduction losses than the IMs for given power specifications. Furthermore, rotor fields produced by the electromagnets can be independently controlled by an external power source which allows the machine to operate under optimal conditions. Finally, as the main materials used in the SFMs are iron and copper, the material costs are relatively inexpensive, unlike PMs.

The requirement for additional electrical and mechanical components is a main drawback of the standard SFM topology. The operation of the SFM typically requires that the field winding current enters the rotor through the use of slip rings and brushes to produce a magnetic field in the rotor. The excitation of the rotor winding requires a rotating mechanical contact that is subject to wear, hence it requires regular maintenance and replacement. Furthermore, the need for a direct current (DC) power supply and an auxiliary circuit to generate and regulate the field winding current adds extra volume, weight, and cost to the drive system.

Brushless and self-excited SFMs have been actively studied and used in many applications to eliminate these additional electrical and mechanical components. The fundamental operation approach of this machine type is based on the process of induction and rectification. In such machines, an auxiliary magnetic field source is used to induce alternating voltages in a winding mounted on the rotor, then the induced voltage is rectified and produces a DC field current in the rotor field winding to operate the machine.

The motivation of this dissertation is to create a new brushless self-excitation scheme and electric machine topology that does not use magnets on the rotor, additional mechanical parts such as brushes and slip rings, and an auxiliary power supply for the field winding on the rotor, but has advantages of the power characteristics of PMs and SFMs like the CPWSR capability.

16

1.3 Literature Review on Related Works and State of The Art

The growing interest in alternative electric machine topologies without using PM materials has introduced several brushless schemes and designs based on the existing SFM topology. Several brushless machine designs have been proposed where the main differences among the previous works of literature lie in different methods of inducing alternating voltages in the additional rotor winding and different control schemes.

A standard brushless SFM design configuration uses a rotating transformer, which has windings and magnetic cores on both the stationary side and the rotating side [18]. The stationary windings of the rotating transformer can be connected to a DC or AC exciter. In the case of a DC exciter, the rotor must be spinning in order to induce AC voltages in the transformer windings, which limits its usage to alternator applications [19]. An AC exciter circuit can be used to generate field current at zero-speed operation. Regardless, the exciter circuit and rotating transformer add volume, mass, and cost.

In an effort to eliminate the magnetic cores of the rotating transformer, Vithayathil [20] proposed the idea of incorporating the transformer into the stator and rotor irons of the machine. This is achieved through the generation by the stator of an auxiliary rotating magnetic field in addition to the main rotating field. With this approach, the auxiliary rotating field is used to induce voltages in the transformer windings, while the main rotating field produced by the stator interacts with that produced by the field winding to generate torque.

One approach based upon this concept is to add an auxiliary winding into the stator slots with the main AC stator windings. In these designs, the auxiliary winding and the transformer windings on the rotor have the same number of poles, which differs from the number of poles of the main stator winding and field winding. The resulting magnetic fields occur at different spatial harmonics. This allows the auxiliary windings to magnetically couple with the transformer windings independently from the main stator windings coupling with the field winding. Nonaka [21] presented a design having a stator with a four-pole three-phase main winding and six-pole single-phase auxiliary winding. The auxiliary winding is supplied by a DC exciter circuit, limiting the

design to alternator applications. In [22], the design has a three-phase auxiliary winding in the stator with different pole numbers than the main winding and a three-phase AC exciter circuit. However, while the magnetic cores of the rotating transformer are removed with this approach, it still requires a separate exciter circuit.

Bukhari et. al. [23] presented an approach to eliminate a separate exciter circuit by connecting auxiliary stator windings to the main AC stator windings through a diode rectifier. The stator consists of a three-phase four-pole winding and a single two-pole auxiliary winding that are connected with an uncontrolled three-phase diode rectifier. On the rotor side, there are four-pole field windings and two-pole harmonic windings that are also connected with a diode rectifier. An improved version of [23] is also presented by Bukhari et. al. [24] with the use of an open-winding AC stator. Although this approach eliminates a separate exciter circuit and can drive the machine with a single inverter, it still requires auxiliary windings on the stator.

Aoyama et. al. [25] presented a line-start type self-excited machine approach utilizing secondary conductor bars on the rotor in addition to induction coils and field coils. Hence, the rotor with a salient pole structure is wound with the two rotor coils, and an auxiliary pole is placed between salient poles on the outer diameter side of the rotor where the secondary conductor bars are arranged to create a magnetic circuit. This configuration allows self-excitation at the time of starting using an induction torque generated by an induced current having a slip frequency flowing through the secondary conductor bars. After the initial acceleration, a rotor field is formed by the second spatial harmonic and rotates at a synchronous speed. Experimental verification was presented in [26]. However, the requirement of the secondary conductor bars and two types of coils on the same rotor core is the main drawback of this approach.

Instead of the inductive power transfer approach, Ludois et. al. [27] introduced a method of capacitive power transfer for rotor field current in the brushless SFM topology. This is accomplished through the use of a rotating capacitor allowing for relative motion between the plates of a parallel plate capacitor while maintaining a constant relative surface area and air gap between the plates. An implementation of this approach was presented in [28]. The design demonstrated

18

specific torque and power densities suitable for electric vehicle traction applications. However, this approach requires a dedicated exciter circuitry for the capacitive power transfer method. From a practical standpoint, there are possible stability issues regarding mechanical plate gap tolerances, vibrations, and resonances for rotor field current generation [27].

In order to remove the need for an exciter circuit and auxiliary stator windings or secondary conductor bars on the rotor, several approaches have exploited the existence of the multiple spatial harmonics produced by a conventional three-phase stator winding. These implementations attempt to exploit the third or fifth spatial harmonic in the magnetomotive force (MMF) produced by the three-phase stator to achieve brushless operation. Nonaka and Kawaguchi [29] presented a method to use these spatial harmonic components to induce an EMF on the transformer coils by superimposing multiple rotating fields with different speeds. An implementation using two modulation schemes of pulse width modulation (PWM) converter is presented in [30], where the approach uses both fundamental and fifth harmonics in the stator to achieve the brushless scheme. Inoue et. al. [31] used the fifth spatial harmonic component for the transformer action. In [32], airgap slot harmonics are used to excite the rotor coils. However, as they are produced by the same currents, the magnitude of these rotating waves are dependent upon one another. Hence these approaches suffer from a lack of ability to control the value of the field current independently from the torque-producing stator current, which severely limits the achievable operating points of the machines.

More recently, a three-phase self-excited field-winding machine approach was introduced in [33] where field-oriented control techniques were used to generate an AC "carrier" field aligned with the transformer winding in the rotor reference frame. This approach allows for independent control of the current in the field winding. An implementation of this approach was presented in [34]. However, the resulting stator voltage components associated with generating the carrier field limit the inverter utilization.

Another approach to generating two independent rotating waves is through the use of different AC stator designs and power electronic topologies. For example, Lipo et. al. [35] used an open-winding three-phase AC stator with dual three-phase inverters connected at each end. This

configuration allows common-mode currents to flow in the stator windings, which are then used to generate an independent rotating wave based upon the third spatial harmonic. However, the use of the open-winding configuration with the dual three-phase inverters for the AC stator adds complexity to control algorithms while also increasing the cost of the drive system.

Conventionally, a three-phase stator design is largely adopted for existing machine topology because combined three-phase stator currents always cancel and become zero at all times. This eliminates all third harmonic sequences (3rd, 9th, 15th, etc) in the resulting total stator MMF which is usually preferable to conventional PMs or SFMs because these machine types require only the fundamental spatial harmonic field to produce torque. However, for independent control of the current in the field winding, the three-phase stator design is not desired because of its inability to produce and control a second rotating magnetic field at a different spatial harmonic that is independent of a field at the fundamental spatial harmonic [36].

The possibility of independent control of multiple spatial harmonics in AC stator designs with five or higher phases is introduced [36, 37]. For instance, a five-phase stator can produce a second rotating wave associated with the third spatial harmonic in addition to the main rotating wave at the fundamental spatial harmonic. These rotating waves can be independently controlled through the use of appropriate current regulation techniques. In [38, 39], a five-phase stator design is used to improve the torque generation in IMs and PMs using the additional third spatial harmonic field.

By utilizing this approach, a new brushless scheme and machine design based on the SFM topology can be developed. AC Stator with five- or higher phases is capable of producing multiple rotating magnetic fields that can be controlled independently. These multiple stator fields can be exploited to achieve separate excitations of the transformer winding and field winding on the rotor for brushless operation. Furthermore, the independent control capability of the multiple stator fields can bring a significant amount of flexibility in operation. For instance, this approach allows changing both the magnitude and electrical frequency of the stator currents associated with the excitation of the transformer winding separately which could achieve high inverter utilization.

1.4 Contribution of This Thesis

This dissertation develops a novel brushless scheme using independently controlled multiple rotating magnetic fields at two different spatial harmonics for designing a brushless self-excited synchronous field-winding machine (BSSFM). Unlike the conventional three-phase AC stator winding design, a stator with a higher number of phases is capable of producing multiple independent spatial harmonic components allowing simultaneous excitation of two different windings on the rotor. This brushless self-excitation approach with independent spatial harmonic fields has not been investigated in previous works of literature.

In this architecture, the machine consists of a five- or higher-phases stator to produce two main spatial harmonics and a rotor with both multi-phase transformer windings and a field winding, connected by a diode rectifier. The high-phase stator design allows independent control of two harmonic fields to excite and interact with each rotor winding. Therefore, one of the spatial harmonic fields can be used to excite the transformer windings in the rotor, transferring power from the stator and producing a rotor field, while another spatial harmonic component can interact with the resulting rotor field to generate an electromagnetic torque.

The BSSFM topology has advantages in reliability over conventional PM and SFM topologies by eliminating permanent magnets, mechanical parts of brushes and slip rings, and auxiliary power supply for the field winding on the rotor. The lack of magnets on the rotor eliminates demagnetization issues at high temperature conditions from the PM topology. Without additional mechanical parts and a power supply for the field winding, the proposed topology can have reduced maintenance costs. Moreover, the elimination of all those materials and components on the rotor contributes to significant material cost reductions.

The BSSFM topology has advantages in performance over conventional IM topology. The independent control capability of both magnitudes and electrical frequencies of the two rotating magnetic fields at different spatial harmonics allows for achieving relatively high power density, high efficiency, and CPWSR capability. Similar to PM and SFM topologies, the torque-producing stator field and the rotor field of the BSSFM can be produced and controlled independently so that

the two fields can achieve spatial orthogonality allowing for high torque density and power factor. Furthermore, the ability to set DC for the transformer-exciting stator field separate from the torque-producing field results in high utilization of the stator voltage at high speeds which contributes to maximizing performance and CPWSR capability.

In comparison to the recent literature works, the proposed BSSFM approach has better voltage utilization than the AC carrier injection method in [33, 34] using the independent control of the electrical frequency associated with the transformer-exciting field. Compared to the open-winding three-phase AC stator approach with dual three-phase inverters [35], the proposed topology has a five- or higher-phase stator configuration which can achieve higher power capability from the main inverters. Considering a metric of the total power capability of a machine divided by the total electrical power ratings of all transistors in inverters, the machine using the open-winding design results in inferior power capability than conventional three-phase AC stator machines, whereas the proposed BSSFM with a higher-phase stator configuration can have superior power capability than three-phase machines.

This dissertation presents the proposed harmonic excitation method, the modeling of system equations, and the development of two simulation tools for the proposed machine topology. For the first simulation tool, a linear magnetic model is developed using a commercial software package of MATLAB and Simulink based on the derivations of inductances for the flux-linkage and current relationship using the winding function approach. A control algorithm for the proposed machine is also developed using the Clarke and Park transformations for the high-phase stator design. The established FOC-based synchronous current regulator is implemented in the linear magnetic model which allows for fast investigations of machine operations with different machine parameters and spatial harmonic couplings.

For the second simulation tool, finite element analysis (FEA) is used to develop a nonlinear magnetic model using the commercial software of ANSYS Electromagnetics Suite based on the machine parameters tested using the first tool. One unique feature in the proposed BSSFM topology is the inclusion of a diode rectifier circuit on the rotor which is uncommon among conventional

machines. To achieve the nonlinear FEA simulation of the proposed machine designs, this dissertation develops a co-simulation environment by combining two different FEA packages (ANSYS Maxwell and ANSYS Circuit Design) in order to achieve the nonlinear simulation of the proposed machine topology. This FEA tool captures more accurate operating behaviors allowing further refinements of the machine designs including a relationship between the machine dimensions and performance improvement considering magnetic saturation.

In the design section, two specific machine designs are developed based on torque capability, transformer design, the feasibility of the rotor design, and ease of manufacturability. The first design focuses on achieving high peak torque capability of the machine by maximizing the magnetic core utilization while the second design focuses on minimizing torque ripple with multiple transformer designs. Finally, the performance of the second machine design is re-evaluated under forced convection where its maximum torque per ampere (MTPA) is observed, and compared with existing machine topologies (PM and IM) to validate its torque- and power-speed characteristics.

In summary, the organization of this dissertation is as follows. Section II will introduce the independent rotating MMF principle. Section III presents the relevant reference transformations for the new stator winding configurations for field-oriented control of the machine. Section IV describes an exemplary machine design and its operating principle. Analysis and simulation results are given in Section V. Finally, the torque and power characteristics of the proposed machine are compared with existing PM and IM topologies in Section VI.

CHAPTER 2

Background

2.1 Reference Frame Theory

The majority of existing AC electric machines have a three-phase stator design. However, analyzing the behavior of AC machines and the resulting rotating magnetic fields using the three variables is not the simplest approach, making it less desirable for the control purpose. In fact, any multi-phase AC stator of three or more can be represented into an equivalent two-phase design using the Stanley model, introduced by William Stanley, Jr. This section presents how the three-phase machines can be converted, analyzed, and controlled using an equivalent two-phase model.

The most basic three-phase AC stator with a two-pole design can be found in Figure 2.1. The three arrows of a, b, and c represent directions of magnetic fields produced by each of the stator phases. Since it is a two-pole stator, each magnetic fields imposed on the rotor create one north and one south pole. The three-phase magnetic fields (H_a, H_b, and H_c) can be converted to the two-phase variables (H_d, H_q, and H_0) using the relationships between the magnitudes and directions of the magnetic field as shown below.

$$\begin{bmatrix} H_d \\ H_q \\ H_0 \end{bmatrix} = \mathbf{T}_{23} \begin{bmatrix} H_a \\ H_b \\ H_c \end{bmatrix},$$

(2.1)

24

where

$$\mathbf{T}_{23} = \frac{2}{3} \begin{bmatrix} \cos(0°) & \cos(120°) & \cos(240°) \\ \sin(0°) & \sin(120°) & \sin(240°) \\ \frac{1}{2} & \frac{1}{2} & \frac{1}{2} \end{bmatrix}. \tag{2.2}$$

This conversion is called the Clarke Transformation and can be used for other variables in the machine, such as voltages, currents, flux linkages, etc. Therefore, the variable of H in Eq. (2.1) can be easily replaced with a variable of interest, which will be denoted as a variable of x. The third variable (H_0) in the two-phase representation is referred to as the "zero-sequence" component. In the three-phase stator with a wye configuration, this zero-sequence component is usually neglected in the analysis and control of the electric drives because the three magnetic fields or currents cancel and become zero. The two-phase stator in Figure 2.2 is essentially equivalent to the three-phase stator after the transformation.

The opposite conversion from the two-phase variables to the three-phase variables is possible using the Inverse Clarke Transformation. The Inverse Clarke Transformation can be determined by taking the inverse of the Clarke Transformation matrix as follows:

$$\begin{bmatrix} x_a \\ x_b \\ x_c \end{bmatrix} = \mathbf{T}_{23}^{-1} \begin{bmatrix} x_d \\ x_q \\ x_0 \end{bmatrix} = \mathbf{T}_{32} \begin{bmatrix} x_d \\ x_q \\ x_0 \end{bmatrix}, \tag{2.3}$$

where

$$\mathbf{T}_{32} = \begin{bmatrix} 1 & 0 & 1 \\ -\frac{1}{2} & \frac{\sqrt{3}}{2} & 1 \\ -\frac{1}{2} & -\frac{\sqrt{3}}{2} & 1 \end{bmatrix}. \tag{2.4}$$

The outputs of the Clarke Transformation, d-q variables, are not appropriate to use in the feed-back controller (e.g., PI controller) because they are still time-varying periodic waveforms. In fact, both the three-phase (a-b-c) and two-phase (d-q-0) variables are represented in the physical frame of reference based on the stator structure, often referred to as the stationary reference frame.
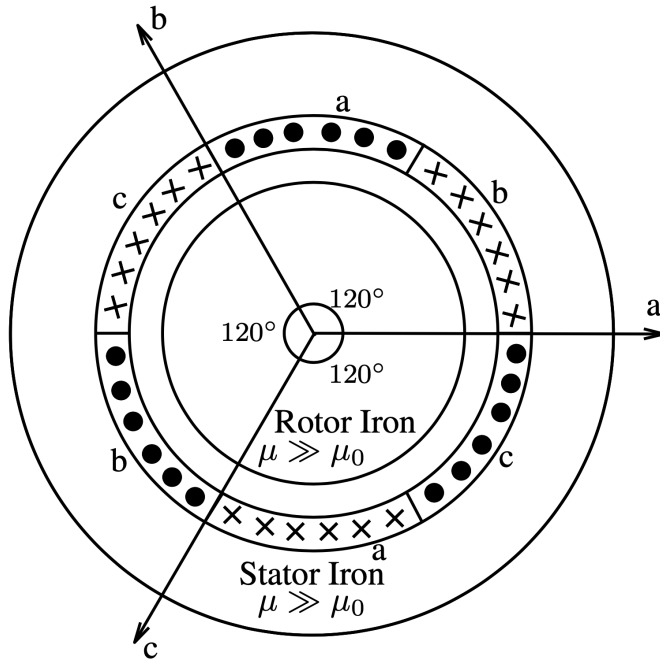
Figure 2.1: Three-phase, two-pole, smooth-airgap AC stator [5]
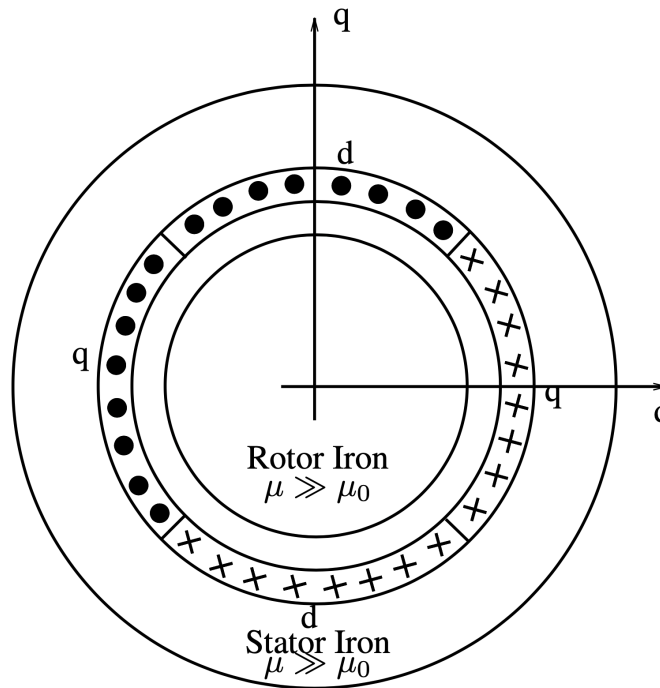
Figure 2.2: Two-phase, two-pole, smooth-airgap AC stator [5]
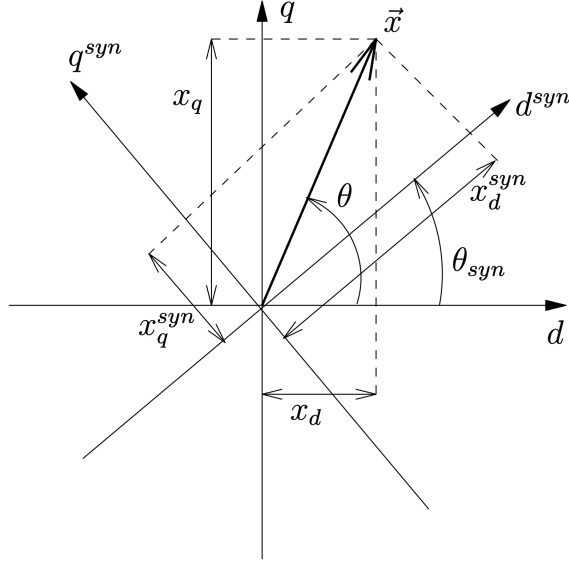
Figure 2.3: Reference frames and Park Transformation [5]

However, these vectors can be redefined in a different conceptual frame of reference. For AC synchronous machines, it is possible to represent the time-varying two-phase electrical variables in constant values by introducing a new frame of reference that rotates in synchronism with the rotor structure. The new coordinate system is called the synchronous reference frames.

A conceptual synchronous reference frame can be defined with an angle shift of θ_{syn} relative to the stationary reference frame in Figure 2.3. The vector $\vec{x}$ in Figure 2.3 can be represented in terms of direct and quadrature components in the stationary reference frame as follows.

$$
\begin{aligned}
x_d &= \|\vec{x}\| \cos(\theta), \\
x_q &= \|\vec{x}\| \sin(\theta),
\end{aligned}
\tag{2.5}
$$

$$
\begin{aligned}
\sin(x - y) &= \sin(x)\cos(y) - \cos(x)\sin(y), \\
\cos(x - y) &= \cos(x)\cos(y) + \sin(x)\sin(y).
\end{aligned}
\tag{2.6}
$$

27

By applying trigonometric identities in Eq. (2.6) to Eq. (2.5), the vector $\vec{x}$ can be expressed in the synchronous reference frame as follows.

$$
\begin{aligned}
x_d^{syn} &= \|\vec{x}\| \cos(\theta - \theta_{syn}) \\
&= \|\vec{x}\| [\cos(\theta) \cos(\theta_{syn}) + \sin(\theta) \sin(\theta_{syn})] \\
&= \cos(\theta_{syn}) x_d + \sin(\theta_{syn}) x_q, \\
x_q^{syn} &= \|\vec{x}\| \sin(\theta - \theta_{syn}) \\
&= \|\vec{x}\| [\sin(\theta) \cos(\theta_{syn}) - \cos(\theta) \sin(\theta_{syn})] \\
&= - \sin(\theta_{syn}) x_d + \cos(\theta_{syn}) x_q.
\end{aligned}
\tag{2.7}
$$

In matrix notation, it can be written as

$$
\begin{bmatrix} x_d^{syn} \\ x_q^{syn} \end{bmatrix} = \begin{bmatrix} \cos(\theta_{syn}) & \sin(\theta_{syn}) \\ -\sin(\theta_{syn}) & \cos(\theta_{syn}) \end{bmatrix} \begin{bmatrix} x_d \\ x_q \end{bmatrix}.
\tag{2.8}
$$

This conversion is called the Park Transformation. The expression shows that the Park Transformation requires a synchronous angle which is basically a difference between two angles associated with the two coordinate systems.

The opposite conversion of two-phase variables from the synchronous reference frame to the stationary reference frame is possible using the Inverse Park Transformation. The Inverse Park Transformation can be determined by taking the inverse of the Park Transformation matrix as follows:

$$
\begin{bmatrix} x_d \\ x_q \end{bmatrix} = \begin{bmatrix} \cos(\theta_{syn}) & -\sin(\theta_{syn}) \\ \sin(\theta_{syn}) & \cos(\theta_{syn}) \end{bmatrix} \begin{bmatrix} x_d^{syn} \\ x_q^{syn} \end{bmatrix}.
\tag{2.9}
$$

The Clarke and Park Transformations simplify analyses of electric machine modeling and are used for control algorithms for electric machines, where the measured three-phase electrical variables in the stationary frame need to be converted into their equivalent two-phase variables in the synchronous reference frame. The steady-state constant two-phase values become a source for the

feedback controller to produce the desired commands. Then, the Inverse Clarke and Park Transformations can be used to convert the two-phase commands in the synchronous reference frame to the three-phase variables in the stationary frame for the electric motors.

2.2 Winding Function Theory

The fundamental operations of the standard rotating electric machines rely on field distributions of magnetic energy produced by current-carrying wires in the stator of the machines. The field distributions of the machines are mainly determined by the winding patterns or arrangements that are mostly placed inside the core slots. Therefore, it is important to understand how winding arrangements determine the field distributions in the machines. The winding function approach allows us to derive the magnetomotive force (MMF) for different winding arrangements uniquely through the winding function under the simplifying assumptions. Furthermore, the winding functions can be utilized in the calculation of winding inductances which are an essential part of modeling electric machines. In this section, an expression of the MMF is derived using the winding function approach [40] for machines with an arbitrary placement of windings in the air gap between the stator and the rotor of machines.

A doubly cylindrical machine with a smooth-airgap model is considered as shown in Figure 2.4. The smooth-airgap model assumes an effective air-gap length is fixed with a constant value and neglects the ripple effects due to the core slots and core shape. It is also assumed that the air-gap length is small relative to the rotor radius, and wires carrying current into the page are considered as positive.

The example machine in Figure 2.4 shows that wires are wound back and forth through the air gap of the machine with N turns. A reference point for the angular circumferential measuring an angle ϕ along the air gap is arbitrarily determined as a point along the gap periphery. The placement of wires that enter into the page is located at 60 degrees from the reference point for the angular measure ϕ along the air gap while the wires that leave out of the page are placed at 240 degrees from the reference point. It is assumed that the counterclockwise direction of the angle ϕ is positive.

By applying the Ampere's Law, the following relationship can be defined for a defined closed

30
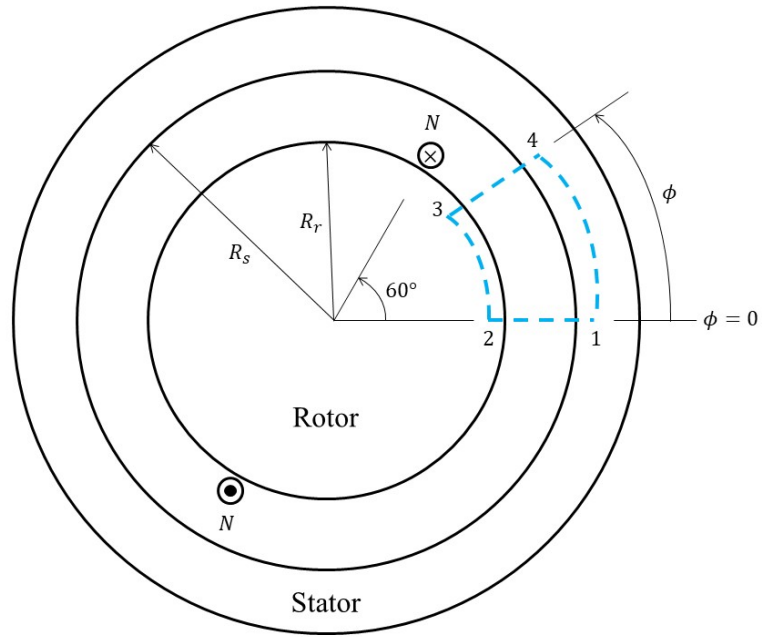
Figure 2.4: Elementary doubly cylindrical device with arbitrary placement of windings in the gap [40]

path 12341 crossing the air gap as

$$\oint_{12341} H \, dl = \int_S J \, dS, \tag{2.10}$$

where S denotes an enclosed surface by the loop path. Assuming the wires carry the same current i, the equation can then be expressed as follows:

$$\oint_{12341} H \, dl = n(\phi)i, \tag{2.11}$$

where $n(\phi)$ is the turn function. The turn function defines the number of turns of the winding within the closed loop path. For the closed loop at $\phi = 60°$, the turn function is $+N$ as the wire

31
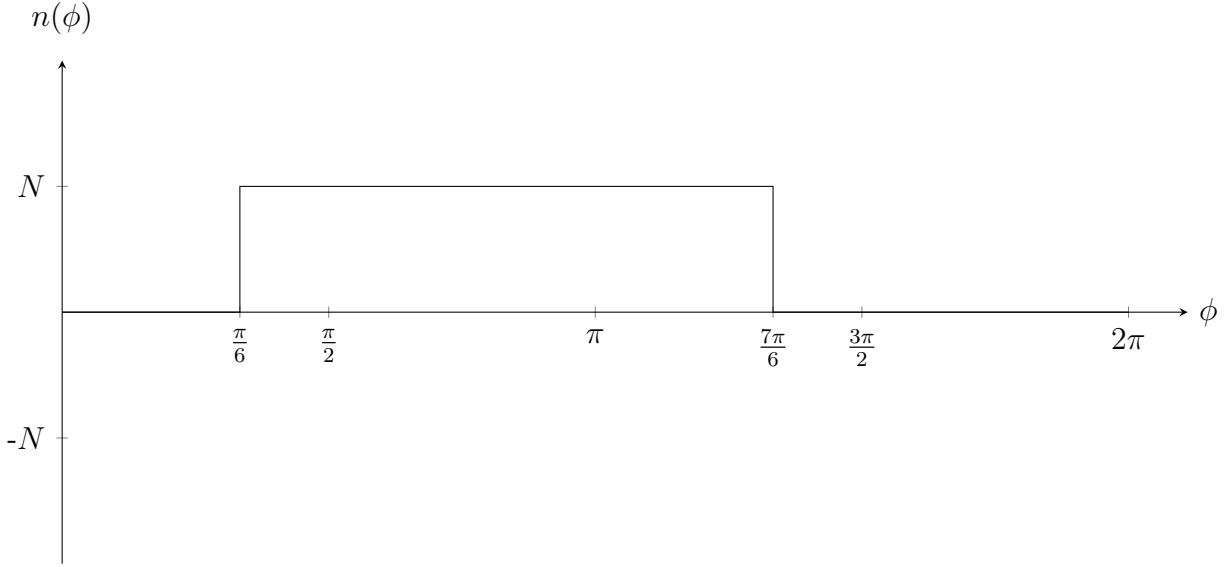
Figure 2.5: Turn function, $n(\phi)$, for arbitrary placement of windings in the gap [40]

enters into the page. Hence, the turn function for one revolution of angle ϕ can be plotted as shown in Figure 2.5.

Since the closed path can be broken into four sections, the Eq. (2.11) can be expressed as follows

$$F_{12} + F_{23} + F_{34} + F_{41} = n(\phi)i, \tag{2.12}$$

where the four terms in the left-hand side represent individual MMF drops for each section of the path. For simplification of analyses, it is assumed that the permeability of iron is very large, therefore the reluctances of the iron sections of the flux path are neglected. Hence, the Eq. (2.12) becomes

$$F_{12} + F_{34} = n(\phi)i. \tag{2.13}$$

The two MMF terms for each segment can be expressed as follows

$$F_{12} = \int_{R_s}^{R_r} H_r(r, 0)\, dr, \qquad (2.14)$$

$$F_{34} = \int_{R_r}^{R_s} H_r(r, \phi)\, dr, \qquad (2.15)$$

where R_s is the inner radius of the stator and R_r is the outer radius of the rotor. Since the air gap length is fixed at a constant value, the Eq. (2.13) can be expressed simply as

$$-H_r(R_s, 0)g + H_r(R_s, \phi)g = n(\phi)i, \qquad (2.16)$$

where g is the length of the air gap between the stator and rotor.

In order to solve the Eq. (2.16), an additional equation of magnetic flux property from Maxwell's Equations is used. According to the conservation of magnetic flux, for a specified surface S, the magnetic flux entering a surface is equal to the magnetic flux leaving the surface, which can be denoted as

$$\oint_S B\, dS = 0. \qquad (2.17)$$

Hence, by setting the rotor of the machine as an enclosed surface S, the Eq. (2.17) can be expressed as follows:

$$\mu_0 \int_0^l \int_0^{2\pi} r H_r(r, \phi)\, d\phi\, dz = 0, \qquad R_r \le r \le R_s \qquad (2.18)$$

where the z-axis represents the axial direction of the machine and l is the axial length of the rotor. It is important to note that the direction of all fluxes in the defined area is perpendicular to the surface due to the assumption of infinite permeability of irons. Moreover, the flux term is independent of the z-axis.

Hence, the Eq. (2.18) can then be written as

$$\mu_0 rl \int_0^{2\pi} H_r(r, \phi) \, d\phi = 0, \tag{2.19}$$

$$\int_0^{2\pi} H_r(r, \phi) \, d\phi = 0, \tag{2.20}$$

$$\int_0^{2\pi} F_{34}(\phi) \, d\phi = 0. \tag{2.21}$$

By integrating the Eq. (2.13) from 0 to 2π and substituting the Eq. (2.19),

$$\int_0^{2\pi} F_{12}(0) \, d\phi + \int_0^{2\pi} F_{34}(\phi) \, d\phi = \int_0^{2\pi} n(\phi) i \, d\phi = 0. \tag{2.22}$$

Therefore,

$$F_{12} = \left[\frac{1}{2\pi} \int_0^{2\pi} n(\phi) \, d\phi \right] i \, = \, < n(\phi) > i. \tag{2.23}$$

From Eqs. 2.13 and 2.23, the MMF drops at any angular position along the air gap can be written as

$$F_{34}(\phi) = (n(\phi) - < n(\phi) >)i = w(\phi)i, \tag{2.24}$$

where the term $w(\phi)$ is the winding function which is essentially the MMF per unit current.

The winding function for this example can be shown in Figure 2.6. The angle ϕ can be easily replaced by different reference points for the convenience of analyses. For example, Figure 2.7 shows the same winding function when the reference axis in Figure 2.4 is shifted by $\frac{\pi}{6}$ in the clockwise direction. The angle ϕ used in this derivation is a mechanical angle, however it is more useful to express the winding function in an electrical angle (ϕ_e) for modeling purposes which can be achieved by the following equation:

$$\phi_e = \frac{N_p}{2}\phi, \tag{2.25}$$

34

where N_p is the number of poles of the winding.

This approach to deriving the winding function can be applied to all windings located in both the stator and rotor of the machine. Using the derived winding functions and currents to excite the windings, the MMF distributions for each phase of windings in the machine at the air gap can be identified. Furthermore, for the analyses of the proposed machine topology, the MMF distributions provide information about the spatial harmonics spectrum which allows us to design the machine more effectively.
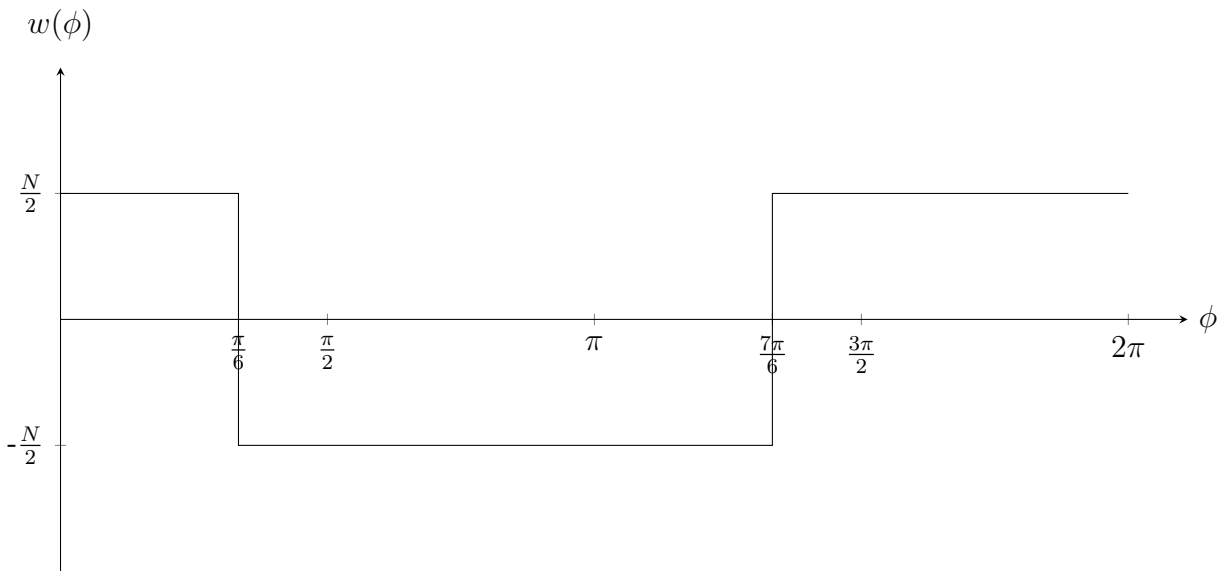
Figure 2.6: Winding function, $w(\phi)$, for arbitrary placement of windings in the gap [40]
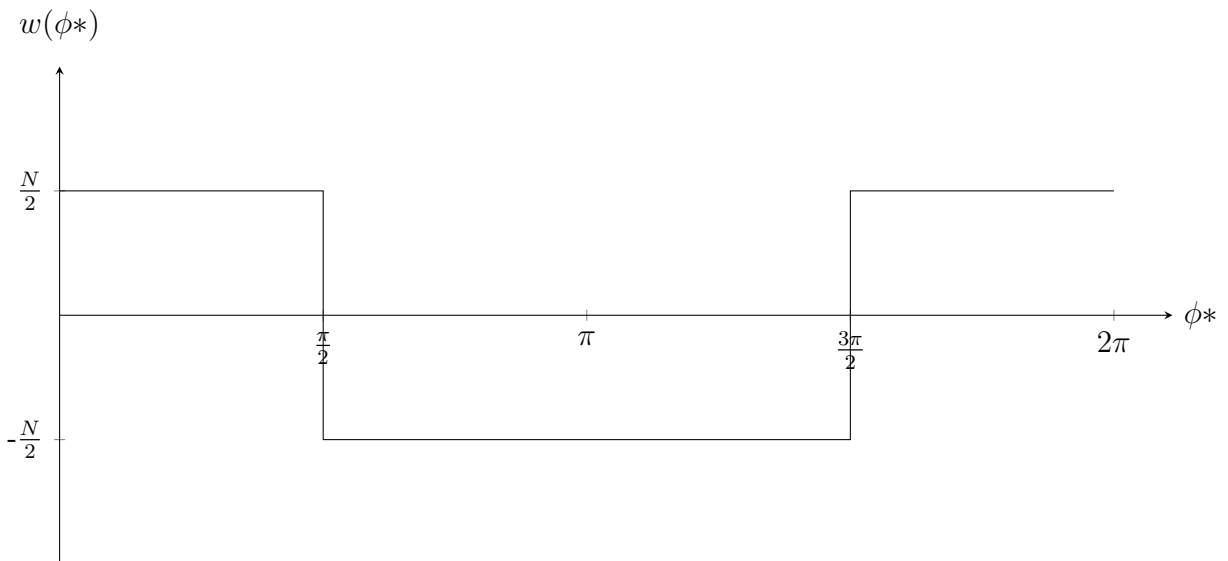
Figure 2.7: Winding function shifted by $\frac{\pi}{6}$ in a clockwise direction [40]

CHAPTER 3

Harmonic Excitation Principle

3.1 Multi-phase Stator Design and Multiple Spatial Harmonics

The number of phases in the stator winding design affects an air-gap MMF and its spatial distributions in the machine iron and the overall performance of AC machines. To achieve a good performance of AC machines, a perfect sine wave of the MMF is desired which can only be achieved if the following conditions are satisfied [41].

- The multi-phase stator winding is excited by balanced sine waveforms with appropriate angle offsets.

- The stator winding is arranged in an infinite number of slots for sinusoidal MMFs.

- The core of machines is made of ideal iron and does not become oversaturated.

Since these conditions are physically unrealistic in a real machine design, the spatial MMF distribution can never be perfectly sinusoidal, therefore the practical MMF consists of multiple rotating waveforms at different spatial harmonics.

For many AC electric machines, a three-phase winding is widely used for the stator design due to its relatively simple structure and the cancellation of balanced three-phase currents when combined [5]. The cancellation of three-phase currents also eliminates the MMF component at the third spatial harmonic. For existing AC machine topologies, the lack of the third spatial harmonic component is advantageous because these machines utilize only the MMF component at the

37

fundamental spatial harmonic to interact with the rotor magnetic field to produce electromagnetic torque.

However, the proposed machine topology needs an additional spatial harmonic component in the air-gap MMF for exciting the transformer windings and the field winding in the rotor. The three-phase design has a limitation in generating the additional spatial harmonic component that is independent of the fundamental spatial harmonic because of a lack of phase numbers.

One may argue that a MMF at the third spatial harmonic could be generated in the three-phase design by injecting a zero-sequence current [42]. However, the resulting third harmonic MMF is fixed in space, therefore it requires a "carrier" signal or high frequency to induce voltages in the transformer windings in the rotor. The injection of a high-frequency component increases the amount of voltage in the stator winding which impacts negatively the power density and torque ripple of machines.

The main advantage of having higher phases for the stator allows to generate multiple magnetic fields at two spatial harmonics that can be generated and controlled independently. This feature is important for the proposed machine topology to achieve independent excitations of two rotor windings which essentially makes this machine topology have the CPWSR capability.

Furthermore, multi-phase machines have a greater fault tolerance than the existing three-phase machines [43]. For the case of the three-phase machines, if one phase of a three-phase winding has a fault and becomes open-circuited, the machine becomes single-phase and loses its operating capability. In contrast, multi-phase machines can still operate even with a fault on one phase of the stator windings.

To generate a second independent spatial harmonic, additional temporal harmonic currents with proper phase angles need to be superimposed to the fundamental phase currents. In addition to the current injection, the stator winding arrangement using different numbers of slots and pole pitches also determines the magnitudes of all spatial harmonic contents in the resultant stator MMF. In this paper, a full-pitch distributed winding design with a single slot per pole per phase is used to achieve independent control of two main spatial harmonics for both five- and six-phase stator

38

designs. According to winding function theory [40], the winding function of one phase of the stator winding can be expressed as follows:

$$w(\phi_e) = \frac{2N_s}{\pi} \sum_{h=1,3,5,\cdots}^{\infty} (-1)^{\frac{h-1}{2}} k_h \cos\Big(h(\phi_e - \theta_{ph})\Big), \tag{3.1}$$

where N_s is the number of turns per slot in the stator, k_h are the respective winding coefficients which vary depending on the winding arrangement, θ_{ph} is the phase shift angle, and ϕ_e is the electrical angle which has a following relationship to a mechanical angle ϕ_m:

$$\phi_e = \frac{N_p}{2}\phi_m, \tag{3.2}$$

where N_p is the number of poles of the stator winding. For example, the winding coefficient for a distributed winding design can be expressed as follows:

$$k_h = \frac{1}{h} \cos\left(\frac{h(\pi - \epsilon)}{2}\right), \tag{3.3}$$

where ϵ is the pole pitch angle in radians.

In this dissertation, a full-pitch distributed winding design with a single slot per pole per phase ($\epsilon = \pi$) is used to achieve independent control of two different spatial harmonics for both five- and six-phase stator designs.

3.1.1 Multiple Spatial Harmonics for Five-phase Stator Design

A five-phase stator winding can produce a rotating MMF at the third spatial harmonic in addition to the fundamental spatial harmonic by superimposing third spatial harmonic currents (i.e., five-phase current components with a phase relationship that produce an MMF at the third spatial

harmonic) as follows:

$$i_a(t) = I_1 \cos(\omega_1 t) + I_3 \cos(\omega_3 t),$$

$$i_b(t) = I_1 \cos\left(\omega_1 t - \frac{2\pi}{5}\right) + I_3 \cos\left(\omega_3 t - 3 \cdot \frac{2\pi}{5}\right),$$

$$i_c(t) = I_1 \cos\left(\omega_1 t - \frac{4\pi}{5}\right) + I_3 \cos\left(\omega_3 t - 3 \cdot \frac{4\pi}{5}\right), \tag{3.4}$$

$$i_d(t) = I_1 \cos\left(\omega_1 t - \frac{6\pi}{5}\right) + I_3 \cos\left(\omega_3 t - 3 \cdot \frac{6\pi}{5}\right),$$

$$i_e(t) = I_1 \cos\left(\omega_1 t - \frac{8\pi}{5}\right) + I_3 \cos\left(\omega_3 t - 3 \cdot \frac{8\pi}{5}\right),$$

where I_1 is the magnitude of the fundamental spatial harmonic current, I_3 is the magnitude of the third spatial harmonic current, ω_1 is an electrical angular frequency of the fundamental spatial harmonic current ($\omega_1 = 2\pi f_1$), ω_3 is an electrical angular frequency of the third spatial harmonic current, and t is time.

Using a combination of the MMFs of all five phases derived from Eq. (3.1) and the stator currents from Eq. (3.4), the total stator MMF can be denoted as

$$F_{5ph}(\phi_e, t) = \frac{N_s}{\pi} I_1 \left[k_1 \cos(\omega_1 t - \phi_e) + k_9 \cos(\omega_1 t + 9\phi_e) + \cdots \right]$$

$$- \frac{N_s}{\pi} I_3 \left[k_3 \cos(\omega_3 t - 3\phi_e) + k_7 \cos(\omega_3 t + 7\phi_e) + \cdots \right]. \tag{3.5}$$

Inspection of Eq. (3.5) reveals that the magnitudes of the fundamental and third harmonic rotating MMFs can be independently controlled by the I_1 and I_3 spatial harmonic currents. Fig. 3.1 shows a five-phase MMF or total MMF distribution based on a full-pitch distributed winding design and its harmonic spectrum at all times with a ratio of the current magnitudes $\frac{I_1}{I_3} = \frac{1}{3}$. This five-phase stator winding therefore produces independent rotating MMFs at both the fundamental and third spatial harmonics.

In addition to the two main rotating MMFs, the stator currents produce extra MMFs at higher harmonic orders. Considering the first twenty harmonics, the fundamental stator currents produce
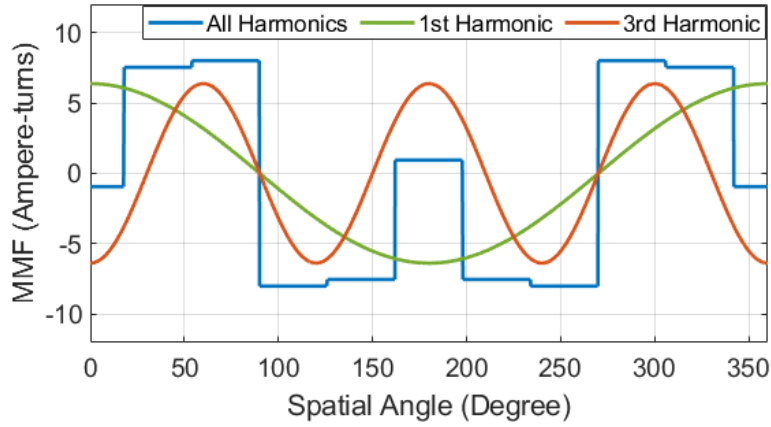
(a)
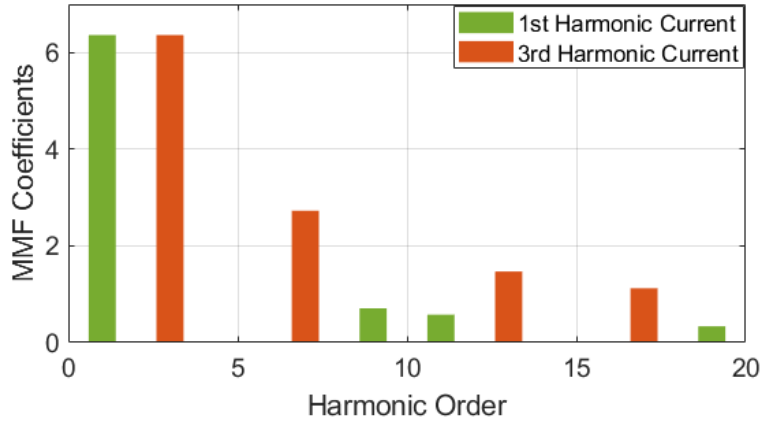
(b)

Figure 3.1: A five-phase stator MMF based on a full-pitch distributed winding design ($N_s = 4$, $I_1 = 1$ A, $I_3 = 3$ A). (a) Total MMF and two main harmonics. (b) Rotating MMF magnitudes as a function of spatial harmonic.

rotating MMFs at the 9th, 11th, and 19th spatial harmonics while the third spatial harmonic currents produce rotating MMFs at the 7th, 13th, and 17th spatial harmonics. Note that there are no common harmonics produced by both spatial harmonic currents. It is important to note that common harmonics can create undesired coupling which can result in torque ripple. However, this only occurs when there are common harmonics in both the stator and the rotor transformer MMFs and their magnitudes are significant when compared to the main spatial harmonics. Moreover, this coupling can potentially be minimized through different winding designs in both the stator and the rotor.

An example of the five-phase stator currents that are superimposed with both spatial harmonic components, and the resulting equivalent two-phase currents in the stationary reference frame are shown in Figure 3.2.
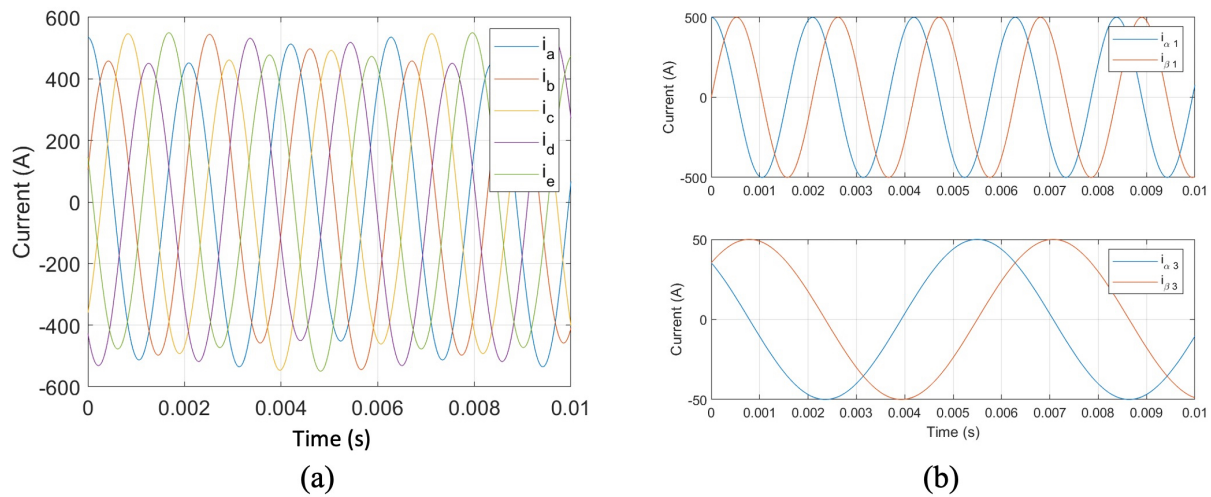
Figure 3.2: Example of five-phase stator currents in: (a) Stationary reference frame, (b) α-β frame

One advantage of this approach is that the frequency of the harmonic currents associated with the excitation of the transformer windings in the rotor can be chosen independently of the rotating frequency, which can be utilized for optimizing the performance of the proposed machine topology. For example, above the base speed operation, the frequency of these harmonic currents can be set to DC to reduce overall voltage generations in the stator of the machine while maintaining the transformer excitation due to the presence of the angular velocity of the rotor. The reduced voltage occupancy by the DC temporal harmonic currents for the transformer winding allows for increasing the torque capability of the machine.

3.1.2 Multiple Spatial Harmonics for Six-phase Stator Design

A six-phase stator winding typically consists of two three-phase windings where the first three-phase winding leads or lags the second three-phase windings by a spatial phase shift of 30° [44]. Six-phase windings can produce MMF waveforms at the fifth spatial harmonic in addition to the fundamental spatial harmonic by superimposing fifth spatial harmonic currents as follows:

$$
\begin{aligned}
i_{a1}(t) &= I_1 \cos\left(\omega_1 t\right) + I_5 \cos\left(\omega_5 t\right), \\
i_{b1}(t) &= I_1 \cos\left(\omega_1 t - \frac{2\pi}{3}\right) + I_5 \cos\left(\omega_5 t - 5 \cdot \frac{2\pi}{3}\right), \\
i_{c1}(t) &= I_1 \cos\left(\omega_1 t - \frac{4\pi}{3}\right) + I_5 \cos\left(\omega_5 t - 5 \cdot \frac{4\pi}{3}\right), \\
i_{a2}(t) &= I_1 \cos\left(\omega_1 t - \frac{\pi}{6}\right) + I_5 \cos\left(\omega_5 t - 5 \cdot \frac{\pi}{6}\right), \\
i_{b2}(t) &= I_1 \cos\left(\omega_1 t - \frac{5\pi}{6}\right) + I_5 \cos\left(\omega_5 t - 5 \cdot \frac{5\pi}{6}\right), \\
i_{c2}(t) &= I_1 \cos\left(\omega_1 t - \frac{9\pi}{6}\right) + I_5 \cos\left(\omega_5 t - 5 \cdot \frac{9\pi}{6}\right),
\end{aligned}
\tag{3.6}
$$

where I_5 is the magnitude of the fifth spatial harmonic current and ω_5 is the electrical angular frequency of the fifth spatial harmonic current.

Similarly, the total MMF of the six-phase stator can be derived using the winding functions and Eq. (3.6) as follows:

$$
\begin{aligned}
F_{6ph}(\phi_e, t) = \frac{N_s}{\pi} I_1 \left[k_1 \cos(\omega_1 t - \phi_e) - k_{11} \cos(\omega_1 t + 11\phi_e) + \cdots \right] \\
+ \frac{N_s}{\pi} I_5 \left[k_5 \cos(\omega_5 t - 5\phi_e) + k_7 \cos(\omega_5 t - 7\phi_e) + \cdots \right].
\end{aligned}
\tag{3.7}
$$

Eq. (3.7) shows the independent control capability of the fundamental and the fifth spatial harmonic rotating MMFs using the I_1 and I_5 spatial harmonic currents. Fig. 3.3 shows a six-phase rotating MMF distribution based on the full-pitch distributed winding design and its spatial harmonic spectrum. This six-phase stator can produce both the fundamental and fifth spatial harmonics in the same magnitudes with a ratio of the current magnitudes $\frac{I_1}{I_5} = \frac{1}{5}$. Similar to the five-phase stator,
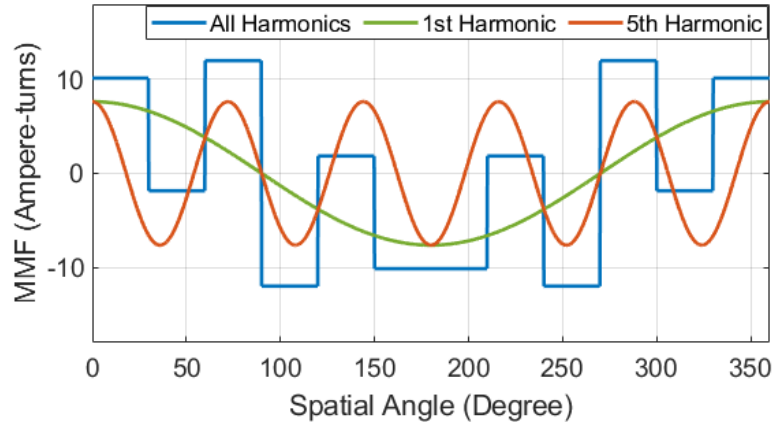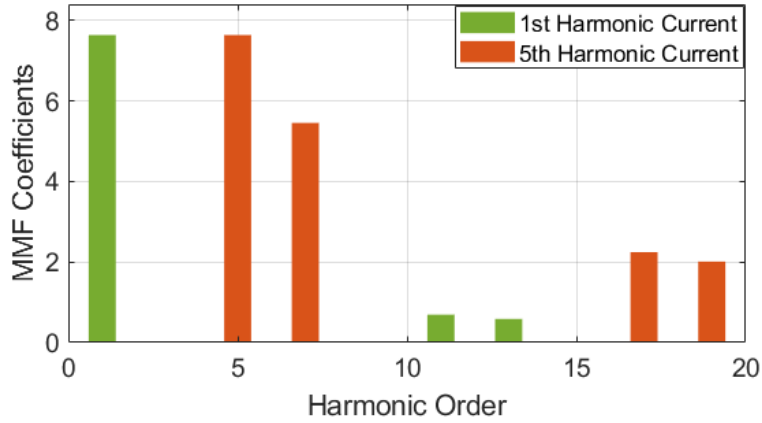
Figure 3.3: A six-phase stator MMF based on a full-pitch distributed winding design ($N_s = 4$, $I_1 = 1$ A, $I_5 = 5$ A). (a) Total MMF and two main harmonics. (b) Rotating MMF magnitudes as a function of spatial harmonic.

each harmonic current produces extra spatial harmonics at higher harmonic orders.

The capability of producing the two main spatial harmonic rotating MMFs efficiently is beneficial for the proposed brushless machine to achieve a higher power capability. Figs. 3.1 and 3.3 show that a five-phase stator with a full-pitch distributed winding design requires less current to produce the third spatial harmonic component that has the same magnitude of the fundamental spatial harmonic component than the six-phase stator. In other words, the magnitude of the third spatial harmonic in the five-phase stator is around 40% greater than the magnitude of the fifth

spatial harmonic in the six-phase for the same current magnitude. In the following sections, a field-oriented control algorithm and a design of a proposed machine topology are therefore presented based on the five-phase stator design.

3.2 Clarke and Park Transformations for Field-oriented Control

For field-oriented control of the multi-phase BSSFM topology, appropriate Clarke and Park transformations need to be used. These reference transformations are used to achieve independent spatial harmonic excitations for five- or six-phase stator. Hence, desired control algorithms can be developed for the proposed machine designs.

In this section, the FOC-based current regulator of the proposed machine is presented. The proposed stator currents consist of two pairs of direct and quadrature (d-q) currents which correspond to the two main spatial harmonic components. The electromagnetic torque of the machine can be controlled indirectly by regulating the equivalent two-phase armature currents that are in synchronism with the rotor frequency while another d-q current is responsible for exciting the transformer windings in the rotor.

To regulate the two sets of d-q currents, a feedback control technique is used as shown in Figure 3.4. When the machine operates, the stator currents are measured using a sensing device and used as the feedback inputs to the FOC-based controller. These measured currents are converted to the equivalent d-q currents using appropriate Clarke and Park transformations. The converted d-q currents are then subtracted from the reference or command currents to produce an error signal which serves as inputs to the feedback controller. The d-q voltages produced by the feedback controller are converted to the reference or command voltages for the inverter circuit using corresponding inverse Clarke and Park transformations. Hence, the resulting voltages from the controller are applied to the armature windings of the machine and produce the desired machine operations.

3.2.1 Five-phase Stator Design

The five-phase stator currents contain two main sets of harmonic components: fundamental and third spatial harmonics. The Clarke transformation, Eq. (3.9), can be used to transform the measured currents into two sets of $\alpha - \beta$ currents, each set responsible for generating different spatial
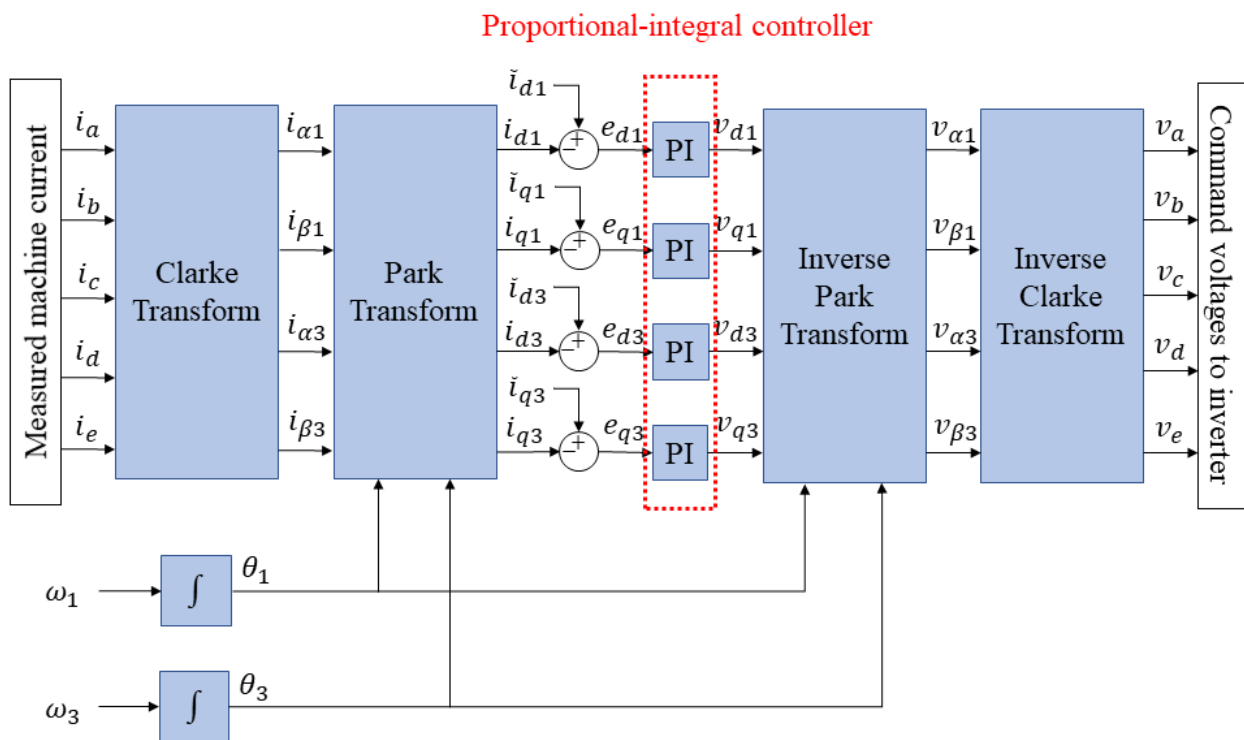
Figure 3.4: FOC-based control algorithm for 5-phase machine

harmonics, and the "zero-sequence" current corresponds to the average of the phase currents:

$$
\begin{bmatrix} i_{\alpha 1} \\ i_{\beta 1} \\ i_{\alpha 3} \\ i_{\beta 3} \\ i_0 \end{bmatrix} = \mathbf{T}_{25} \begin{bmatrix} i_a \\ i_b \\ i_c \\ i_d \\ i_e \end{bmatrix} ,
$$

(3.8)

$$
\mathbf{T}_{25} = \frac{2}{5} \begin{bmatrix} \cos(\frac{2\pi \cdot 0}{5}) & \cos(\frac{2\pi \cdot 1}{5}) & \cos(\frac{2\pi \cdot 2}{5}) & \cos(\frac{2\pi \cdot 3}{5}) & \cos(\frac{2\pi \cdot 4}{5}) \\ \sin(\frac{2\pi \cdot 0}{5}) & \sin(\frac{2\pi \cdot 1}{5}) & \sin(\frac{2\pi \cdot 2}{5}) & \sin(\frac{2\pi \cdot 3}{5}) & \sin(\frac{2\pi \cdot 4}{5}) \\ \cos(\frac{2\pi \cdot 0}{5}) & \cos(\frac{2\pi \cdot 3}{5}) & \cos(\frac{2\pi \cdot 6}{5}) & \cos(\frac{2\pi \cdot 9}{5}) & \cos(\frac{2\pi \cdot 12}{5}) \\ \sin(\frac{2\pi \cdot 0}{5}) & \sin(\frac{2\pi \cdot 3}{5}) & \sin(\frac{2\pi \cdot 6}{5}) & \sin(\frac{2\pi \cdot 9}{5}) & \sin(\frac{2\pi \cdot 12}{5}) \\ \frac{1}{2} & \frac{1}{2} & \frac{1}{2} & \frac{1}{2} & \frac{1}{2} \end{bmatrix} ,
$$

(3.9)

where the zero sequence current i_0 is constrained to be zero due to the star-connected winding configuration of the stator windings.

The two sets of $\alpha - \beta$ currents can be transformed again using the following Park transformation into two synchronous reference frames that correspond to each rotating wave as follows:

$$
\begin{bmatrix} i_{d1} \\ i_{q1} \end{bmatrix} = \begin{bmatrix} \cos(\theta_1) & \sin(\theta_1) \\ -\sin(\theta_1) & \cos(\theta_1) \end{bmatrix} \begin{bmatrix} i_{\alpha 1} \\ i_{\beta 1} \end{bmatrix} ,
$$

$$
\begin{bmatrix} i_{d3} \\ i_{q3} \end{bmatrix} = \begin{bmatrix} \cos(\theta_3) & \sin(\theta_3) \\ -\sin(\theta_3) & \cos(\theta_3) \end{bmatrix} \begin{bmatrix} i_{\alpha 3} \\ i_{\beta 3} \end{bmatrix} ,
$$

(3.10)

where

$$
\frac{d\theta_1}{dt} = \omega_1,
$$
$$
\frac{d\theta_3}{dt} = \omega_3.
$$

These transformations are then used as part of a current regulator. One way to implement the current regulation is to use proportional-integral (PI) feedback controllers. Each controller can produce d-q voltage commands which can be subsequently converted into their $\alpha - \beta$ variables using the following inverse Park transformations:

$$
\begin{bmatrix} v_{\alpha 1} \\ v_{\beta 1} \end{bmatrix} = \begin{bmatrix} \cos(\theta_1) & -\sin(\theta_1) \\ \sin(\theta_1) & \cos(\theta_1) \end{bmatrix} \begin{bmatrix} v_{d1} \\ v_{q1} \end{bmatrix},
$$

$$
\begin{bmatrix} v_{\alpha 3} \\ v_{\beta 3} \end{bmatrix} = \begin{bmatrix} \cos(\theta_3) & -\sin(\theta_3) \\ \sin(\theta_3) & \cos(\theta_3) \end{bmatrix} \begin{bmatrix} v_{d3} \\ v_{q3} \end{bmatrix}. \tag{3.11}
$$

The two sets of $\alpha - \beta$ voltages are then used to determine duty cycles which generate the corresponding five-phase voltages in an average-value sense. These five-phase voltages are given by the following inverse Clarke transform:

$$
\begin{bmatrix} v_a \\ v_b \\ v_c \\ v_d \\ v_e \end{bmatrix} = \mathbf{T}_{52} \begin{bmatrix} v_{\alpha 1} \\ v_{\beta 1} \\ v_{\alpha 3} \\ v_{\beta 3} \\ v_0 \end{bmatrix}, \tag{3.12}
$$

$$
\mathbf{T}_{52} = \begin{bmatrix} \cos(\frac{2\pi \cdot 0}{5}) & \sin(\frac{2\pi \cdot 0}{5}) & \cos(\frac{2\pi \cdot 0}{5}) & \sin(\frac{2\pi \cdot 0}{5}) & 1 \\ \cos(\frac{2\pi \cdot 1}{5}) & \sin(\frac{2\pi \cdot 1}{5}) & \cos(\frac{2\pi \cdot 3}{5}) & \sin(\frac{2\pi \cdot 3}{5}) & 1 \\ \cos(\frac{2\pi \cdot 2}{5}) & \sin(\frac{2\pi \cdot 2}{5}) & \cos(\frac{2\pi \cdot 6}{5}) & \sin(\frac{2\pi \cdot 6}{5}) & 1 \\ \cos(\frac{2\pi \cdot 3}{5}) & \sin(\frac{2\pi \cdot 3}{5}) & \cos(\frac{2\pi \cdot 9}{5}) & \sin(\frac{2\pi \cdot 9}{5}) & 1 \\ \cos(\frac{2\pi \cdot 4}{5}) & \sin(\frac{2\pi \cdot 4}{5}) & \cos(\frac{2\pi \cdot 12}{5}) & \sin(\frac{2\pi \cdot 12}{5}) & 1 \end{bmatrix},
$$

where v_0 is the zero-sequence voltage. If the five-phase winding has a common neutral connection, the zero-sequence voltage, unlike the zero-sequence current, is not constrained to be zero and is a degree of freedom to utilize for maximizing the voltages that can be applied to the machine [45].

3.2.2 Six-phase Stator Design

The six-phase stator currents contain two main sets of harmonic components: fundamental and fifth spatial harmonics. The Clarke transformation, Eq. (3.14), can be used to transform the measured currents into two sets of $\alpha - \beta$ currents, each set responsible for generating different spatial harmonics. The Clarke transformation matrix for the six-phase stator results in two zero-sequence currents where both correspond to the respective average of the two three-phase currents:

$$
\begin{bmatrix} i_{\alpha 1} \\ i_{\beta 1} \\ i_{\alpha 5} \\ i_{\beta 5} \\ i_{0+} \\ i_{0-} \end{bmatrix} = \mathbf{T}_{26} \begin{bmatrix} i_{a1} \\ i_{b1} \\ i_{c1} \\ i_{a2} \\ i_{b2} \\ i_{c2} \end{bmatrix},
\tag{3.13}
$$

$$
\mathbf{T}_{26} = \frac{1}{3} \begin{bmatrix} \cos(\frac{2\pi \cdot 0}{3}) & \cos(\frac{2\pi \cdot 1}{3}) & \cos(\frac{4\pi \cdot 1}{3}) & \cos(\frac{\pi \cdot 1}{6}) & \cos(\frac{5\pi \cdot 1}{6}) & \cos(\frac{9\pi \cdot 1}{6}) \\ \sin(\frac{2\pi \cdot 0}{3}) & \sin(\frac{2\pi \cdot 1}{3}) & \sin(\frac{4\pi \cdot 1}{3}) & \sin(\frac{\pi \cdot 1}{6}) & \sin(\frac{5\pi \cdot 1}{6}) & \sin(\frac{9\pi \cdot 1}{6}) \\ \cos(\frac{2\pi \cdot 0}{3}) & \cos(\frac{2\pi \cdot 5}{3}) & \cos(\frac{4\pi \cdot 5}{3}) & \cos(\frac{\pi \cdot 5}{6}) & \cos(\frac{5\pi \cdot 5}{6}) & \cos(\frac{9\pi \cdot 5}{6}) \\ \sin(\frac{2\pi \cdot 0}{3}) & \sin(\frac{2\pi \cdot 5}{3}) & \sin(\frac{4\pi \cdot 5}{3}) & \sin(\frac{\pi \cdot 5}{6}) & \sin(\frac{5\pi \cdot 5}{6}) & \sin(\frac{9\pi \cdot 5}{6}) \\ 1 & 1 & 1 & 0 & 0 & 0 \\ 0 & 0 & 0 & 1 & 1 & 1 \end{bmatrix},
\tag{3.14}
$$

where the two zero sequence currents i_{0+} and i_{0-} are constrained to be zero due to the wye-connected winding configuration of the both three-phase windings.

The two sets of $\alpha - \beta$ currents can be transformed again using the following Park transformation into two synchronous reference frames that correspond to each rotating wave as follows:

$$\begin{bmatrix} i_{d1} \\ i_{q1} \end{bmatrix} = \begin{bmatrix} \cos(\theta_1) & \sin(\theta_1) \\ -\sin(\theta_1) & \cos(\theta_1) \end{bmatrix} \begin{bmatrix} i_{\alpha 1} \\ i_{\beta 1} \end{bmatrix},$$

$$\begin{bmatrix} i_{d5} \\ i_{q5} \end{bmatrix} = \begin{bmatrix} \cos(\theta_5) & \sin(\theta_5) \\ -\sin(\theta_5) & \cos(\theta_5) \end{bmatrix} \begin{bmatrix} i_{\alpha 5} \\ i_{\beta 5} \end{bmatrix}, \qquad (3.15)$$

where

$$\frac{d\theta_1}{dt} = \omega_1,$$
$$\frac{d\theta_5}{dt} = \omega_5.$$

These transformations can then be used as part of a current regulator. One way to implement the current regulation is to use proportional-integral (PI) feedback controllers. Each controller can produce d-q voltage commands which can be subsequently converted into their $\alpha - \beta$ variables using the following inverse Park transformations:

$$\begin{bmatrix} v_{\alpha 1} \\ v_{\beta 1} \end{bmatrix} = \begin{bmatrix} \cos(\theta_1) & -\sin(\theta_1) \\ \sin(\theta_1) & \cos(\theta_1) \end{bmatrix} \begin{bmatrix} v_{d1} \\ v_{q1} \end{bmatrix},$$

$$\begin{bmatrix} v_{\alpha 5} \\ v_{\beta 5} \end{bmatrix} = \begin{bmatrix} \cos(\theta_5) & -\sin(\theta_5) \\ \sin(\theta_5) & \cos(\theta_5) \end{bmatrix} \begin{bmatrix} v_{d5} \\ v_{q5} \end{bmatrix}. \qquad (3.16)$$

The two sets of $\alpha - \beta$ voltages are then used to determine duty cycles which generate the corresponding six-phase voltages in an average-value sense. These six-phase voltages are given by

the following inverse Clarke transform:

$$
\begin{bmatrix} v_{a1} \\ v_{b1} \\ v_{c1} \\ v_{a2} \\ v_{b2} \\ v_{c2} \end{bmatrix} = \mathbf{T}_{62} \begin{bmatrix} v_{\alpha 1} \\ v_{\beta 1} \\ v_{\alpha 5} \\ v_{\beta 5} \\ v_{0+} \\ v_{0-} \end{bmatrix},
\tag{3.17}
$$

$$
\mathbf{T}_{62} = \begin{bmatrix}
\cos(\frac{2\pi \cdot 0}{3}) & \sin(\frac{2\pi \cdot 0}{3}) & \cos(\frac{2\pi \cdot 0}{3}) & \sin(\frac{2\pi \cdot 0}{3}) & 1 & 0 \\
\cos(\frac{2\pi \cdot 1}{3}) & \sin(\frac{2\pi \cdot 1}{3}) & \cos(\frac{2\pi \cdot 5}{3}) & \sin(\frac{2\pi \cdot 5}{3}) & 1 & 0 \\
\cos(\frac{4\pi \cdot 1}{3}) & \sin(\frac{4\pi \cdot 1}{3}) & \cos(\frac{4\pi \cdot 5}{3}) & \sin(\frac{4\pi \cdot 5}{3}) & 1 & 0 \\
\cos(\frac{\pi \cdot 1}{6}) & \sin(\frac{\pi \cdot 1}{6}) & \cos(\frac{\pi \cdot 5}{6}) & \sin(\frac{\pi \cdot 5}{6}) & 0 & 1 \\
\cos(\frac{5\pi \cdot 1}{6}) & \sin(\frac{5\pi \cdot 1}{6}) & \cos(\frac{5\pi \cdot 5}{6}) & \sin(\frac{5\pi \cdot 5}{6}) & 0 & 1 \\
\cos(\frac{9\pi \cdot 1}{6}) & \sin(\frac{9\pi \cdot 1}{6}) & \cos(\frac{9\pi \cdot 5}{6}) & \sin(\frac{9\pi \cdot 5}{6}) & 0 & 1
\end{bmatrix},
\tag{3.18}
$$

where v_{0+} and v_{0-} are the zero-sequence voltages. If the six-phase winding has common neutral connections, the zero-sequence voltages, unlike the zero-sequence currents, are not constrained to be zero and are a degree of freedom to utilize for maximizing the voltages that can be applied to the machine [45].

3.3 Brushless Machine Design Concept

This section introduces the basic concept embodiment of the proposed brushless, self-excited synchronous field-winding machine and its operating principle. Specific machine designs will be discussed in Chapter 5. The machine consists of an AC stator with more than three phases, and the rotor has both the main field winding and an additional transformer winding with a single- or multi-phase design. The transformer and the field windings on the rotor are connected through a diode rectifier with the corresponding phase numbers of the transformer winding.

The AC stator with a higher phase design can produce independent rotating, controllable magnetic fields at two or more spatial harmonics. Hence, each rotor winding couples with different spatial harmonics produced by the stator windings. For example, one of the stator MMF traveling waves that couples with the transformer winding can rotate at a different velocity than the angular velocity of the rotor. Therefore, the transformer winding "sees" an AC magnetic field which induces voltage or electromotive force (EMF). Simultaneously, another main stator MMF wave at different spatial harmonic couples with the field winding, which rotates in synchronism with the rotor. As a result, it interacts with a DC field current produced by the EMF in the transformer winding and is transferred through a diode rectifier, producing an electromagnetic torque.

A basic embodiment concept of the proposed machine topology is shown in Figure 3.5. This design is based on the five-phase stator having a two-pole design and utilizes the fundamental and third spatial harmonic components to operate the machine. Mounted on the rotor includes three-phase transformer windings with two-pole and six-pole field winding. Hence, the fundamental spatial harmonic component from the stator induces an EMF in the transformer winding, which is then rectified to supply voltage in the field winding and produce a main rotor field. By having the six-pole design of the field winding that is three times the number of poles of the stator windings, the resulting rotor field from the field winding couples with the third spatial harmonic component from the stator, which then generates an electromagnetic torque of the machine.

For control purposes, the five-phase stator currents in the stationary reference frame of this machine can be converted into two pairs of direct and quadrature (d-q) currents that are in the
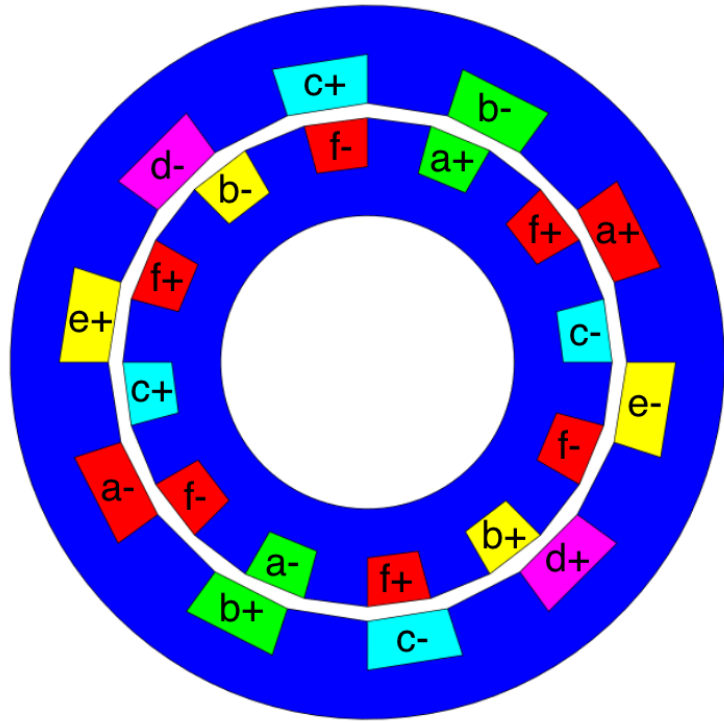
Figure 3.5: Basic embodiment concept of proposed machine topology based on the five-phase stator (rectifier not shown).

synchronous reference frame. Each pair of the d-q currents that correspond to the two temporal harmonics are responsible for producing the two main spatial harmonics. When the rotor field from the field winding is aligned with the direct axis, the quadrature component of the third temporal harmonic current is used to produce torque. The direct component of the third temporal harmonic current can be used for field-weakening above the base speed under the voltage-constrained condition. The d-q components of the fundamental temporal harmonic current are used to induce voltages in the transformer windings. The magnitude and frequency of the fundamental current can be controlled independently of the third harmonic current, hence the field current can also be controlled independently of the torque-producing stator field.

CHAPTER 4

Modeling and Simulation Tools

4.1 Significance of Lumped-parameter Model and Finite Element Analysis Model

The conventional approach to analyzing electric machines relies on knowledge of electromagnetic fields which provide the necessary information, such as magnetic flux distributions, current density, and force distributions, to model these machines. However, this method requires complicated boundary conditions for the given geometry of the machine, and many analyses are performed using finite element analysis (FEA) tools, requiring extensive digital computing horsepower and time. To expedite some of the analyses, the modeling approach using the winding function theory, introduced in the previous chapter, is used to provide a more simplified and convenient method that can capture the basic behaviors of the machines.

In this dissertation, both the lumped-parameter model and the FEA model are utilized for designing the proposed machines. The lumped-parameter model can demonstrate the basic behavior of the proposed electric machine. In the initial stage of the design process, it is important to understand how fundamental design choices, such as the number of phases in the stator winding and winding types of the stator and rotor windings, affect the fundamental behavior of an electric machine. The lumped-parameter model built using MATLAB and Simulink environments is used as a simulation tool to analyze magnetic fields and spatial harmonics in MMFs and determine design choices. Furthermore, the models are used for verifying the fundamental operating princi-

55

ples of the machines based on various design choices. This simulation tool can also be used for testing different machine parameters quickly and verifying the machine operations. The presented lumped-parameter model is limited to capturing the linear magnetic behaviors of the machines. Once the fundamental design choices are determined using the presented lumped-parameter models, the nonlinear FEA model is used for further refinements of the machine designs.

The nonlinear FEA model can provide accurate behavior of an electric machine by capturing saturation and slotting effects. Therefore, it becomes suitable for design optimizations. The FEA models are built from machine geometric parameters and material properties using ANSYS Maxwell.

Both the lumped-parameter model and the FEA model incorporate a diode rectifier model in the rotor which is unique for the proposed machine topology. For the lumped-parameter model, a system-based circuit model is used to construct a full-bridge diode rectifier that can be implemented in MATLAB and Simulink models. For the FEA models, the ANSYS Maxwell Circuit Editor is used to construct and link a full-bridge diode rectifier to the FEA models built in ANSYS Maxwell.

4.2 System Equations

4.2.1 Winding Function

The winding function approach presented in the previous chapter is used to derive winding functions of all phases of the stator and the rotor windings. The five-phase stator winding with a two-pole configuration is considered instead of a higher pole used in the final machine designs since the winding function expression in terms of an electrical angle is identical regardless of the number of poles of the machine.

4.2.1.1 Winding Function for Stator Winding

Based on the presented winding function derivation in chapter 2, the winding functions of the five-phase stator windings can be expressed in terms of an electrical angle below:

$$
\begin{aligned}
w_{sa}(\phi_e) &= \frac{2N_s}{\pi} \left[k_{s1}\cos(\phi_e) - \frac{1}{3}k_{s3}\cos(3\phi_e) + \frac{1}{5}k_{s5}\cos(5\phi_e) - \cdots \right], \\
w_{sb}(\phi_e) &= \frac{2N_s}{\pi} \left[k_{s1}\cos\left(\phi_e - \frac{2\pi}{5}\right) - \frac{1}{3}k_{s3}\cos\left(3\phi_e - \frac{6\pi}{5}\right) + \cdots \right], \\
w_{sc}(\phi_e) &= \frac{2N_s}{\pi} \left[k_{s1}\cos\left(\phi_e - \frac{4\pi}{5}\right) - \frac{1}{3}k_{s3}\cos\left(3\phi_e - \frac{12\pi}{5}\right) + \cdots \right], \\
w_{sd}(\phi_e) &= \frac{2N_s}{\pi} \left[k_{s1}\cos\left(\phi_e - \frac{6\pi}{5}\right) - \frac{1}{3}k_{s3}\cos\left(3\phi_e - \frac{18\pi}{5}\right) + \cdots \right], \\
w_{se}(\phi_e) &= \frac{2N_s}{\pi} \left[k_{s1}\cos\left(\phi_e - \frac{8\pi}{5}\right) - \frac{1}{3}k_{s3}\cos\left(3\phi_e - \frac{24\pi}{5}\right) + \cdots \right],
\end{aligned}
\tag{4.1}
$$

where $k_{s,h}$ are the winding coefficients for the stator winding. The winding functions of the five-phase stator windings based on the full-pitch distributed winding design can be found in Figure 4.1.
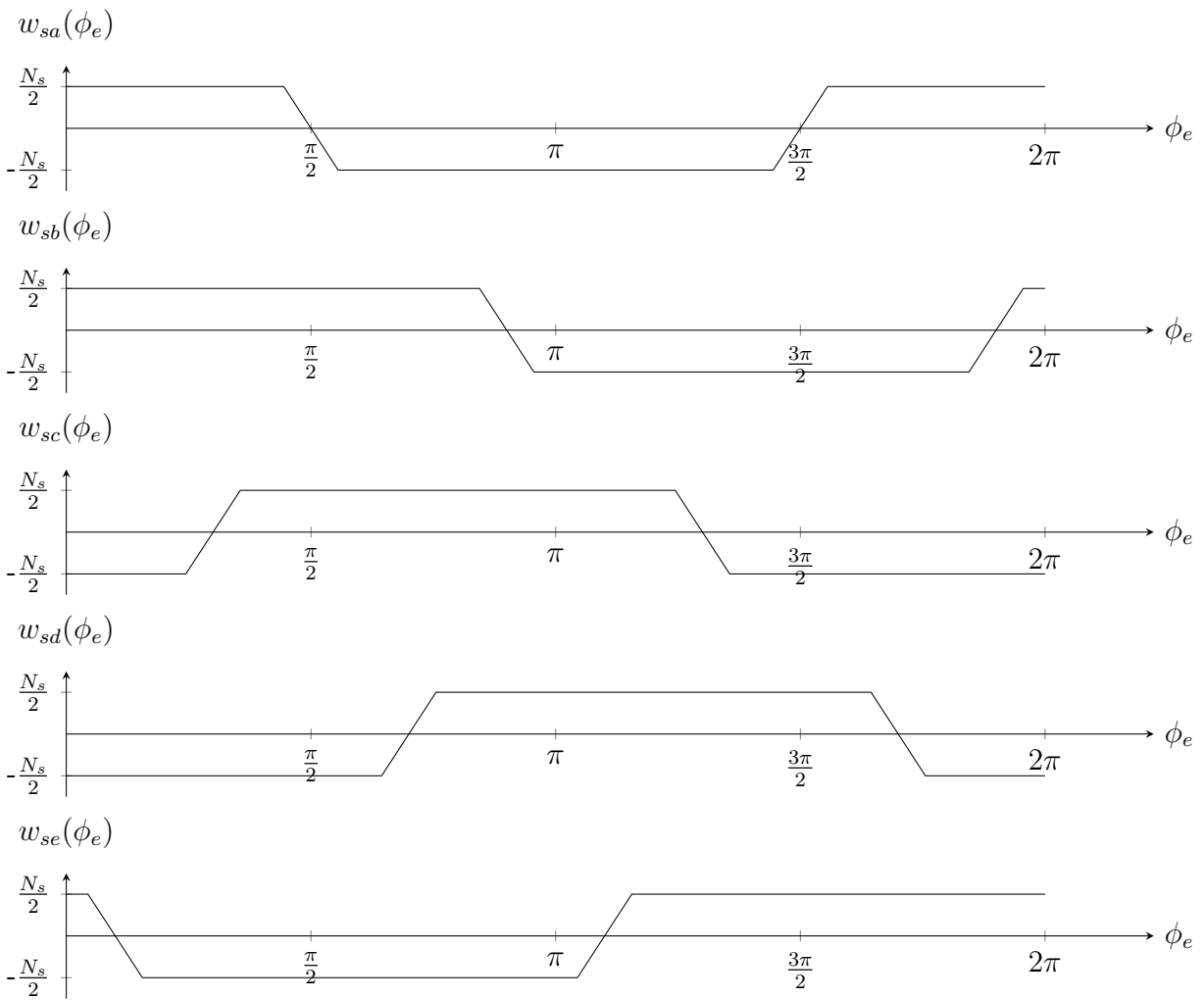
Figure 4.1: An example of winding functions of five-phase stator windings using the full-pitch distributed winding design

4.2.1.2 Winding Functions for Transformer Winding and Field Winding

Using the same method for the stator winding, the winding functions of a single- or three-phase transformer windings can be derived as

$$w_t(\phi_{re}) = \frac{2N_t}{\pi} \left[k_{t1} \cos(\phi_{re}) - \frac{1}{3} k_{t3} \cos(3\phi_{re}) + \frac{1}{5} k_{t5} \cos(5\phi_{re}) - \cdots \right], \tag{4.2}$$

or

$$
\begin{aligned}
w_{ta}(\phi_{re}) &= \frac{2N_t}{\pi} \left[k_{t1} \cos(\phi_{re}) - \frac{1}{3} k_{t3} \cos(3\phi_{re}) + \frac{1}{5} k_{t5} \cos(5\phi_{re}) - \cdots \right], \\
w_{tb}(\phi_{re}) &= \frac{2N_t}{\pi} \left[k_{t1} \cos\left(\phi_{re} - \frac{2\pi}{3}\right) - \frac{1}{3} k_{t3} \cos\left(3\phi_{re} - \frac{6\pi}{3}\right) + \cdots \right], \\
w_{tc}(\phi_{re}) &= \frac{2N_t}{\pi} \left[k_{t1} \cos\left(\phi_{re} - \frac{4\pi}{3}\right) - \frac{1}{3} k_{t3} \cos\left(3\phi_{re} - \frac{12\pi}{3}\right) + \cdots \right],
\end{aligned}
$$

$$\tag{4.3}$$

where $k_{t,h}$ are the winding coefficients for the transformer winding, and ϕ_{re} represents the electrical angle with respect to the reference rotor axis. Figure 4.2 shows an example of the winding function for one phase of the transformer winding using the concentrated winding design.

The winding function of the field winding can be expressed as

$$w_f(\phi_{re}) = \frac{2N_f}{\pi} \left[k_{f1} \cos(3\phi_{re}) - \frac{1}{3} k_{f3} \cos(9\phi_{re}) + \frac{1}{5} k_{f5} \cos(15\phi_{re}) - \cdots \right] \tag{4.4}$$

where $k_{f,h}$ are the winding coefficients for the field winding. Figure 4.3 shows an example of the winding function for the field winding using the fractional-pitch distributed winding design.
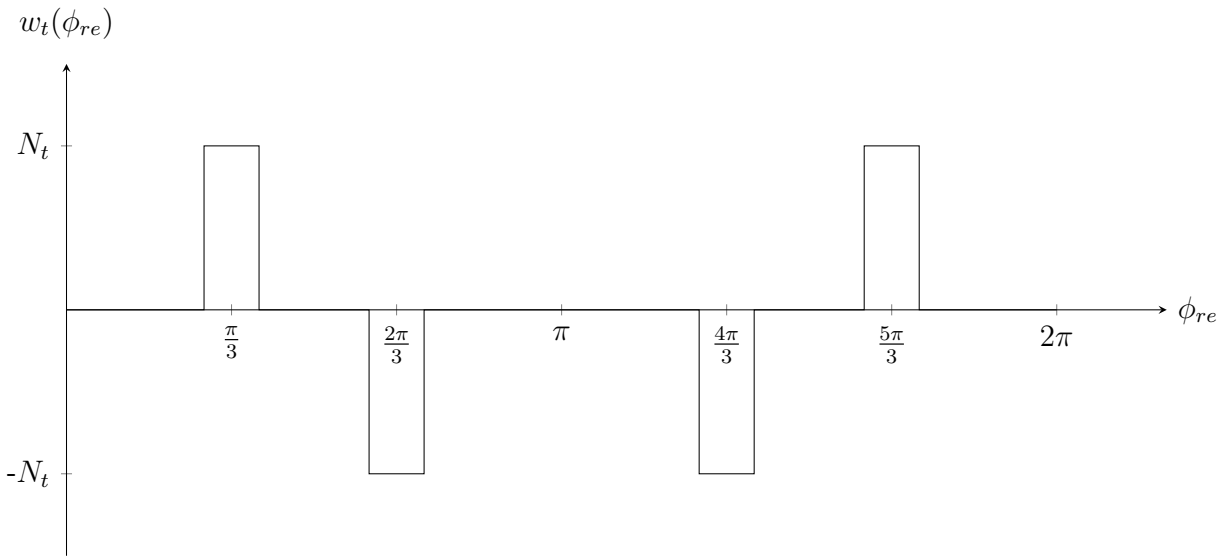
Figure 4.2: An example of a winding function of transformer winding using concentrated winding design
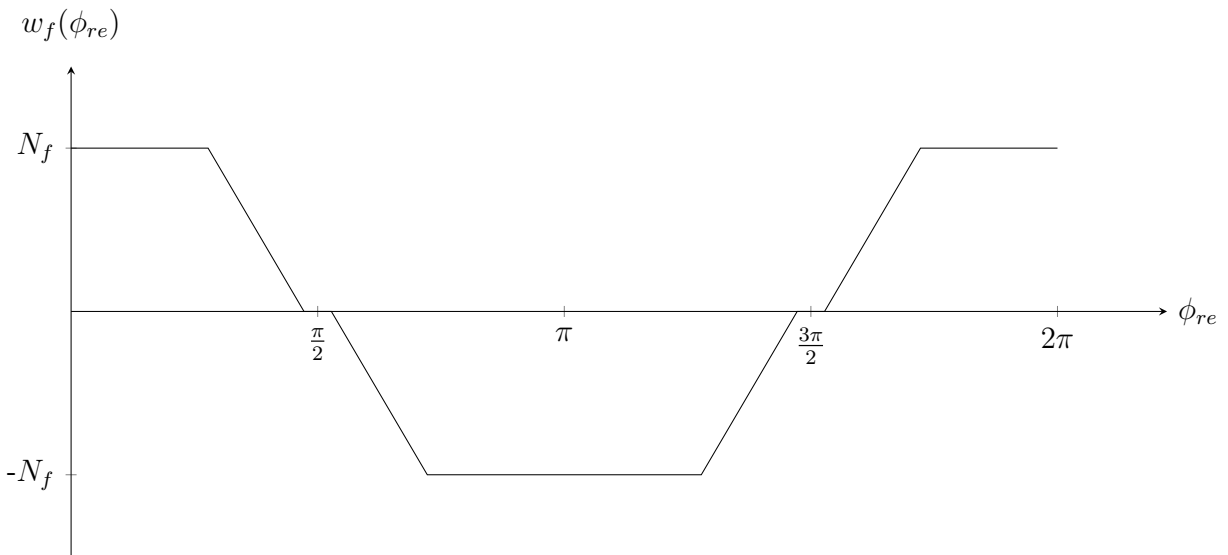
Figure 4.3: An example of a winding function of field winding using fractional-pitch distributed winding design

4.2.1.3   Relationship Between Mechanical and Electrical Angles of Stator and Rotor

A relationship between a mechanical and an electrical angle of the stator and rotor is defined with respect to two different axes and a relative rotor position. It is useful to express winding functions in the electrical angle with a consistent reference frame or axis for calculating inductances of the machines in the following sections.
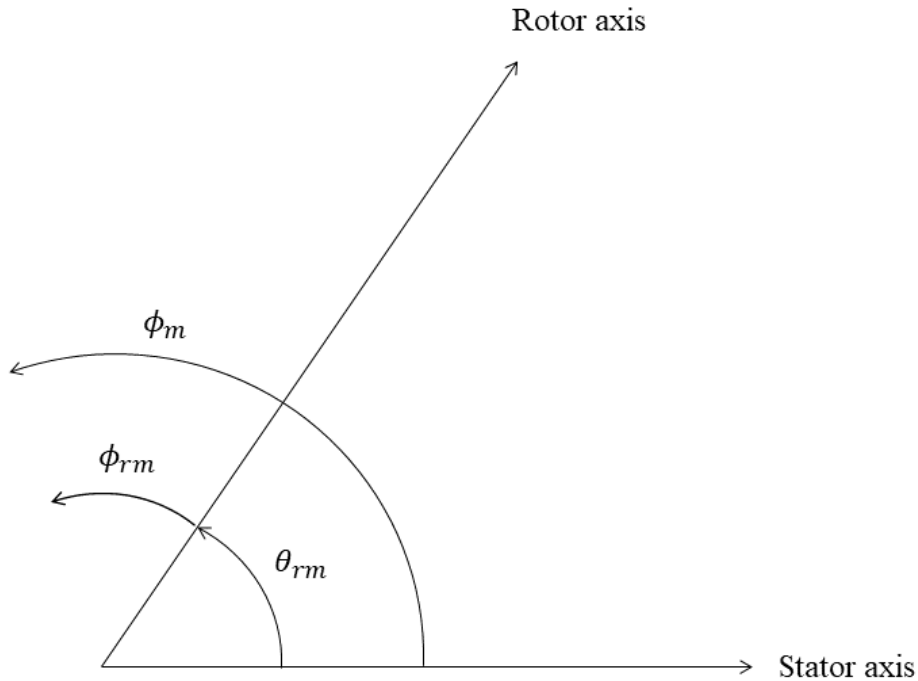
Figure 4.4: Relationship of mechanical angles with respect to the two reference axes

Figure 4.4 shows two axes, defined with respect to the stator and rotor windings, and respective mechanical angles. The stator axis is a reference point used for deriving the winding functions for the stator windings, and the rotor axis is a reference point used for the transformer and the field windings. The relationships between these mechanical angles can be derived as

$$\phi_m = \phi_{rm} + \theta_{rm}, \tag{4.5}$$

where ϕ_m is the mechanical angle based on the stator axis, ϕ_{rm} is the mechanical angle based on the rotor axis, and θ_{rm} is the relative mechanical angle of the rotor axis with respect to the stator

axis or the rotor position in the mechanical angle.

Then, the relationship between the mechanical angles and electrical angles can be defined using the number of poles of the respective windings as follows:

$$\phi_e = \frac{N_p}{2}\phi_m, \tag{4.6}$$

$$\phi_{re} = \frac{N_p}{2}\phi_{rm}, \tag{4.7}$$

$$\theta_{re} = \frac{N_p}{2}\theta_{rm}, \tag{4.8}$$

Hence, using the Equations (4.5)–(4.8), the relationship between the stator and the rotor axes in the electrical angle can be derived as

$$\phi_{re} = \phi_e - \theta_{re}. \tag{4.9}$$

4.2.2 Inductance

The inductance of the machine provides a key metric for modeling the machine operations. The inductances of all windings in the stator and rotor of the machine generate the flux-linkage and current relationships which relate the energy conversions between the magnetic power and the electrical power.

In this section, self- and mutual inductances of the stator, transformer, and field windings are derived using the winding functions which account for the spatial harmonics of each winding. Moreover, it is assumed that the air-gap length is uniformly constant, referred to as a smooth-air-gap model. Also, the permeability of the stator and rotor irons is assumed to be significantly larger than the permeability of the air-gap.

4.2.2.1 Self-Inductance of Stator, Transformer, and Field Windings

Self-inductance of the stator, transformer, and field windings are derived. In general, the self-inductance consists of a leakage inductance and an air-gap inductance as follows:

$$L_{self} = L_{leak} + L_{gap}. \tag{4.10}$$

The air-gap inductance is a main component of the self-inductance, and the leakage inductance due to the magnetic core slots is dealt with in the following section.

According to the winding function theory, the air-gap inductance of a winding can be derived using the following expression:

$$L_{gap} = \mu_0 r l \int_0^{2\pi} \frac{(w(\phi_e))^2}{g} d\phi_e, \tag{4.11}$$

where μ_0 is the permeability of the air-gap, r is the average air-gap radius, l is the axial length of the core, g is the effective air-gap length, and $w(\phi_e)$ is the winding function.

A useful trigonometric identity for the derivations of the air-gap inductance is the product identity which is

$$\cos(\alpha)\cos(\beta) = \frac{\cos(\alpha + \beta) + \cos(\alpha - \beta)}{2}. \tag{4.12}$$

Another property that simplifies the derivation process is shown as follows:

$$\int_0^{2\pi} \cos(m\phi)\cos(n\phi)d\phi = 0, \quad \text{if} \quad m \neq n \tag{4.13}$$

which states that the property that all product terms containing non-similar frequencies become zero.

The gap inductance of one phase of the stator winding can be calculated using the winding

function of that phase shown as

$$L_{sa,gap} = \mu_0 rl \int_0^{2\pi} \frac{(w_{sa}(\phi_e))^2}{g} d\phi_e \tag{4.14}$$

$$= \frac{\mu_0 rl}{g} \int_0^{2\pi} \left(\frac{2N_s}{\pi} \left(k_{s1} \cos(\phi_e) - \frac{1}{3} k_{s3} \cos(3\phi_e) + \cdots \right) \right)^2 d\phi_e \tag{4.15}$$

$$= \frac{4\mu_0 rl N_s^2}{g\pi} \left(k_{s1}^2 + \left(\frac{1}{3} \right)^2 k_{s3}^2 + \cdots \right). \tag{4.16}$$

Inspection of the air-gap inductance of one phase of the stator winding shows that the air-gap inductances for the remaining phases of the stator windings result in the same expression. Hence,

$$L_{s,self} = L_{s,leak} + \frac{4\mu_0 rl N_s^2}{g\pi} \left(k_{s1}^2 + \left(\frac{1}{3} \right)^2 k_{s3}^2 + \cdots \right). \tag{4.17}$$

The air-gap inductances of the transformer winding and the field winding can be derived using the same procedure leading to

$$L_{t,self} = L_{t,leak} + \frac{4\mu_0 rl N_t^2}{g\pi} \left(k_{t1}^2 + \left(\frac{1}{3} \right)^2 k_{t3}^2 + \cdots \right), \tag{4.18}$$

$$L_{f,self} = L_{f,leak} + \frac{4\mu_0 rl N_f^2}{g\pi} \left(k_{f1}^2 + \left(\frac{1}{3} \right)^2 k_{f3}^2 + \cdots \right). \tag{4.19}$$

4.2.2.2 Mutual Inductance between Stator Windings

The mutual inductance between different phases of windings can be derived similarly using the multiplication of two respective winding functions as follows:

$$M_{12} = \mu_0 rl \int_0^{2\pi} \frac{w_1(\phi) w_2(\phi)}{g} d\phi. \tag{4.20}$$

Hence, the mutual inductance between the phase-a and b of the stator winding can be calculated

as follows:

$$M_{sab} = \mu_0 rl \int_0^{2\pi} \frac{w_{sa}(\phi_e)w_{sb}(\phi_e)}{g} d\phi_e \tag{4.21}$$

$$= \frac{\mu_0 rl}{g} \int_0^{2\pi} \left(\left(\frac{2N_s}{\pi}\right)^2 (k_{s1}\cos(\phi_e) - \cdots) \left(k_{s1}\cos\left(\phi_e - \frac{2\pi}{5}\right) - \cdots \right) \right) d\phi_e \tag{4.22}$$

$$= \frac{4\mu_0 rl N_s^2}{g\pi} \left(k_{s1}^2 \cos\left(\frac{2\pi}{5}\right) + \left(\frac{1}{3}\right)^2 k_{s3}^2 \cos\left(3 \cdot \frac{2\pi}{5}\right) + \cdots \right). \tag{4.23}$$

Similarly, the remaining mutual inductances between other phases of the stator winding can be expressed as

$$M_{sac} = \frac{4\mu_0 rl N_s^2}{g\pi} \left(k_{s1}^2 \cos\left(\frac{4\pi}{5}\right) + \left(\frac{1}{3}\right)^2 k_{s3}^2 \cos\left(3 \cdot \frac{4\pi}{5}\right) + \cdots \right), \tag{4.24}$$

$$M_{sad} = \frac{4\mu_0 rl N_s^2}{g\pi} \left(k_{s1}^2 \cos\left(\frac{6\pi}{5}\right) + \left(\frac{1}{3}\right)^2 k_{s3}^2 \cos\left(3 \cdot \frac{6\pi}{5}\right) + \cdots \right), \tag{4.25}$$

$$M_{sae} = \frac{4\mu_0 rl N_s^2}{g\pi} \left(k_{s1}^2 \cos\left(\frac{8\pi}{5}\right) + \left(\frac{1}{3}\right)^2 k_{s3}^2 \cos\left(3 \cdot \frac{8\pi}{5}\right) + \cdots \right). \tag{4.26}$$

The difference in the mutual inductances between two phases is caused by the difference in the phase angle of the two phases. Hence, the following relationship can be deduced as

$$M_{sab} = M_{sbc} = M_{scd} = M_{sde}, \tag{4.27}$$

$$M_{sac} = M_{sbd} = M_{sce}, \tag{4.28}$$

$$M_{sad} = M_{sbe}. \tag{4.29}$$

4.2.2.3 Mutual Inductance between Stator Winding and Transformer Winding

The mutual inductance between one phase of the stator winding and the transformer winding can be calculated using Equation (4.9) as follows:

$$M_{sat} = \mu_0 rl \int_0^{2\pi} \frac{w_{sa}(\phi_e) w_t(\phi_{re})}{g} d\phi_e \tag{4.30}$$

$$= \mu_0 rl \int_0^{2\pi} \frac{w_{sa}(\phi_e) w_t(\phi_e - \theta_{re})}{g} d\phi_e \tag{4.31}$$

$$= \frac{\mu_0 rl}{g} \int_0^{2\pi} \left[\left(\frac{4 N_s N_t}{\pi^2} \right) (k_{s1} \cos(\phi_e) - \cdots)(k_{t1} \cos(\phi_e - \theta_{re}) - \cdots) \right] d\phi_e \tag{4.32}$$

$$= \frac{4 \mu_0 rl N_s N_t}{g\pi} \left(k_{s1} k_{t1} \cos(\theta_{re}) + \left(\frac{1}{3} \right)^2 k_{s3} k_{t3} \cos(3\theta_{re}) + \cdots \right). \tag{4.33}$$

Similarly, the remaining mutual inductances between different phases of the stator windings and the transformer winding can be expressed as

$$M_{sbt} = \frac{4 \mu_0 rl N_s N_t}{g\pi} \left(k_{s1} k_{t1} \cos \left(\theta_{re} - \frac{2\pi}{5} \right) + \left(\frac{1}{3} \right)^2 k_{s3} k_{t3} \cos \left(3 \left(\theta_{re} - \frac{2\pi}{5} \right) \right) + \cdots \right),$$
$$\tag{4.34}$$

$$M_{sct} = \frac{4 \mu_0 rl N_s N_t}{g\pi} \left(k_{s1} k_{t1} \cos \left(\theta_{re} - \frac{4\pi}{5} \right) + \left(\frac{1}{3} \right)^2 k_{s3} k_{t3} \cos \left(3 \left(\theta_{re} - \frac{4\pi}{5} \right) \right) + \cdots \right),$$
$$\tag{4.35}$$

$$M_{sdt} = \frac{4 \mu_0 rl N_s N_t}{g\pi} \left(k_{s1} k_{t1} \cos \left(\theta_{re} - \frac{6\pi}{5} \right) + \left(\frac{1}{3} \right)^2 k_{s3} k_{t3} \cos \left(3 \left(\theta_{re} - \frac{6\pi}{5} \right) \right) + \cdots \right),$$
$$\tag{4.36}$$

$$M_{set} = \frac{4 \mu_0 rl N_s N_t}{g\pi} \left(k_{s1} k_{t1} \cos \left(\theta_{re} - \frac{8\pi}{5} \right) + \left(\frac{1}{3} \right)^2 k_{s3} k_{t3} \cos \left(3 \left(\theta_{re} - \frac{8\pi}{5} \right) \right) + \cdots \right).$$
$$\tag{4.37}$$

4.2.2.4 Mutual Inductance between Stator Winding and Field Winding

The mutual inductance between one phase of the stator winding and the field winding can be calculated as follows:

$$M_{saf} = \mu_0 r l \int_0^{2\pi} \frac{w_{sa}(\phi_e) w_f(\phi_{re})}{g} d\phi_e \tag{4.38}$$

$$= \mu_0 r l \int_0^{2\pi} \frac{w_{sa}(\phi_e) w_f(\phi_e - \theta_{re})}{g} d\phi_e \tag{4.39}$$

$$= \frac{4\mu_0 r l N_s N_f}{g\pi^2} \int_0^{2\pi} \left(k_{s1} \cos(\phi_e) - \frac{1}{3} k_{s3} \cos(3\phi_e) \cdots \right) \left(k_{f1} \cos(3(\phi_e - \theta_{re})) - \cdots \right) d\phi_e \tag{4.40}$$

$$= -\frac{4\mu_0 r l N_s N_f}{g\pi} \left(\frac{1}{3} k_{s3} k_{f1} \cos(3\theta_{re}) + \frac{1}{27} k_{s9} k_{f3} \cos(9\theta_{re}) + \cdots \right) \tag{4.41}$$

Note that the field winding, in this case, is assumed to have three times more poles than the stator winding so that the field on the rotor produced by the field winding can couple with the stator field at the third spatial harmonic.

Similarly, the remaining mutual inductances between different phases of the stator windings and the field winding can be expressed as

$$M_{sbf} = -\frac{4\mu_0 r l N_s N_f}{g\pi} \left(\frac{1}{3} k_{s3} k_{f1} \cos \left(3 \left(\theta_{re} - \frac{2\pi}{5} \right) \right) + \frac{1}{27} k_{s9} k_{f3} \cos \left(9 \left(\theta_{re} - \frac{2\pi}{5} \right) \right) + \cdots \right), \tag{4.42}$$

$$M_{scf} = -\frac{4\mu_0 r l N_s N_f}{g\pi} \left(\frac{1}{3} k_{s3} k_{f1} \cos \left(3 \left(\theta_{re} - \frac{4\pi}{5} \right) \right) + \frac{1}{27} k_{s9} k_{f3} \cos \left(9 \left(\theta_{re} - \frac{4\pi}{5} \right) \right) + \cdots \right), \tag{4.43}$$

$$M_{sdf} = -\frac{4\mu_0 r l N_s N_f}{g\pi} \left(\frac{1}{3} k_{s3} k_{f1} \cos \left(3 \left(\theta_{re} - \frac{6\pi}{5} \right) \right) + \frac{1}{27} k_{s9} k_{f3} \cos \left(9 \left(\theta_{re} - \frac{6\pi}{5} \right) \right) + \cdots \right), \tag{4.44}$$

$$M_{sef} = -\frac{4\mu_0 r l N_s N_f}{g\pi} \left(\frac{1}{3} k_{s3} k_{f1} \cos \left(3 \left(\theta_{re} - \frac{8\pi}{5} \right) \right) + \frac{1}{27} k_{s9} k_{f3} \cos \left(9 \left(\theta_{re} - \frac{8\pi}{5} \right) \right) + \cdots \right). \tag{4.45}$$

4.2.2.5 Leakage Inductance

The leakage inductance is an inductive component that results from imperfect magnetic couplings within a single-phase winding. In this section, the leakage inductance due to a magnetic slot, known as the slot leakage inductance, is modeled for both the stator and rotor windings based on the method in [46]. The slot leakage inductance corresponds to fluxes that cross a conductor circumferentially from one tooth to another, closing its path around the back-iron beneath the slot that does not cross the air gap. Figure 4.5 shows a typical slot and tooth structure that applies to both the stator and rotor with a winding located inside each slot.
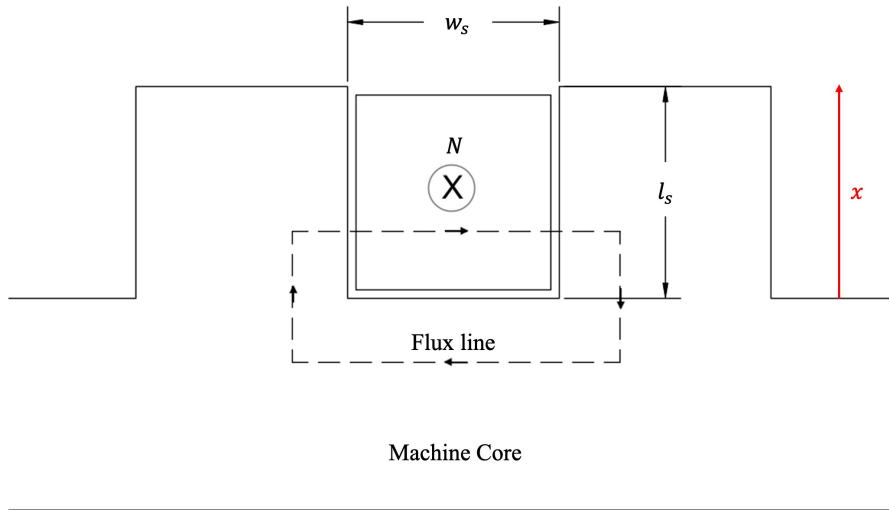

Figure 4.5: Leakage flux path for one core slot

By Ampere's Law, the ampere-turns enclosed by the specific flux path shown in 4.5 can be defined as

$$\oint \vec{H}_{slot} d\vec{l} = i_{slot}, \tag{4.46}$$

where H_{slot} is the magnetic intensity of the slot, and i_{slot} is the current flowing in the winding inside the slot.

It is assumed that the permeability of the iron is significantly large, and the magnetic intensity in a slot H_{slot} increases linearly as the distance from the back-iron x increases. Then, the magnetic intensity of the slot can be expressed as a function of the distance x along the tooth as

$$H_{slot} = \frac{Ni}{w_s l_s} x, \quad 0 \leq x \leq l_s \tag{4.47}$$

where N is the number of turns in the slot, w_s is the width of the slot, and l_s is the length of the slot.

In general, the magnetic energy density in a slot can be defined as

$$w = \frac{1}{2}\vec{B}\vec{H} = \frac{1}{2}\mu_0|\vec{H}|^2 = \frac{1}{2}\mu_0 H_{slot}^2. \tag{4.48}$$

Hence, the magnetic energy stored in a slot as a function of the currents becomes

$$W_{slot} = \iiint_V w \, dV \tag{4.49}$$

$$= 2w_s l_c \int_0^{l_s} \frac{1}{2}\mu_0 H_{slot}^2 \, dx \tag{4.50}$$

$$= \frac{\mu_0 N^2 l_s l_c}{3w_s} i^2, \tag{4.51}$$

where l_c is the length of the iron.

Therefore, the leakage inductance for a single slot can be derived by relating Equation (4.51) and a general magnetic energy of the slot leakage inductance as follows:

$$W_{slot} = \frac{\mu_0 N^2 l_s l_c}{3w_s} i^2 = \frac{1}{2} L_{leak} i^2, \tag{4.52}$$

$$L_{leak} = \frac{2\mu_0 N^2 l_s l_c}{3w_s}. \tag{4.53}$$

The expression can be used to calculate the total slot leakage inductances based upon the number of slots and the number of poles for a given machine design.

4.2.3 Flux-linkage and Current Relationship

Under the assumption of a linear magnetic relationship, the flux-linkage and current relationship can be derived using the inductances derived from the previous sections in a vector-matrix form. For example, the flux-linkage and current relationship for the machine design consisting of a five-phase stator winding, a single-phase transformer winding, and a single-phase field winding can be expressed as follows:

$$
\begin{bmatrix} \vec{\lambda}_s \\ \lambda_t^r \\ \lambda_f^r \end{bmatrix} = \begin{bmatrix} \mathbf{L}_s & \vec{M}_{st} & \vec{M}_{sf} \\ \vec{M}_{st}^T & L_t & M_{tf} \\ \vec{M}_{sf}^T & M_{tf} & L_f \end{bmatrix} \begin{bmatrix} \vec{i}_s \\ i_t^r \\ i_f^r \end{bmatrix},
\tag{4.54}
$$

where

$$
\mathbf{L}_s = \begin{bmatrix} L_{sa} & M_{sab} & M_{sac} & M_{sad} & M_{sae} \\ M_{sab} & L_{sb} & M_{sbc} & M_{sbd} & M_{sbe} \\ M_{sac} & M_{sbc} & L_{sc} & M_{scd} & M_{sce} \\ M_{sad} & M_{sbd} & M_{scd} & L_{sd} & M_{sde} \\ M_{sae} & M_{sbe} & M_{sce} & M_{sde} & L_{se} \end{bmatrix},
\tag{4.55}
$$

$$
\vec{M}_{st} = \begin{bmatrix} M_{sat} \\ M_{sbt} \\ M_{sct} \\ M_{sdt} \\ M_{set} \end{bmatrix},
\tag{4.56}
$$

$$
\vec{M}_{sf} = \begin{bmatrix} M_{saf} \\ M_{sbf} \\ M_{scf} \\ M_{sdf} \\ M_{sef} \end{bmatrix}.
\tag{4.57}
$$

The combined inductance matrix reveals that the diagonal elements of the matrix represent the self-inductance of each phase. The off-diagonal elements of the matrix represent the mutual inductances between the corresponding two phases of different windings. In the case of the machine design that uses three-phase transformer winding instead of the single-phase winding, the inductance matrix can be adjusted by replacing the self-inductance component for the transformer winding and the mutual inductance components between the transformer winding and the stator or the field windings with corresponding new inductance components in appropriately sized matrices or vectors.

The flux-linkage and current relationship provides core operating behaviors of the proposed machine design as it relates to the energy conversions between the magnetic energy and the electrical energy.

4.2.4 Phase Resistance of Winding

4.2.4.1 Distributed Winding Type

Modeling of a phase resistance using a full-pitch distributed winding type is presented. Figure 4.6 shows the winding layout of one phase of the distributed winding.
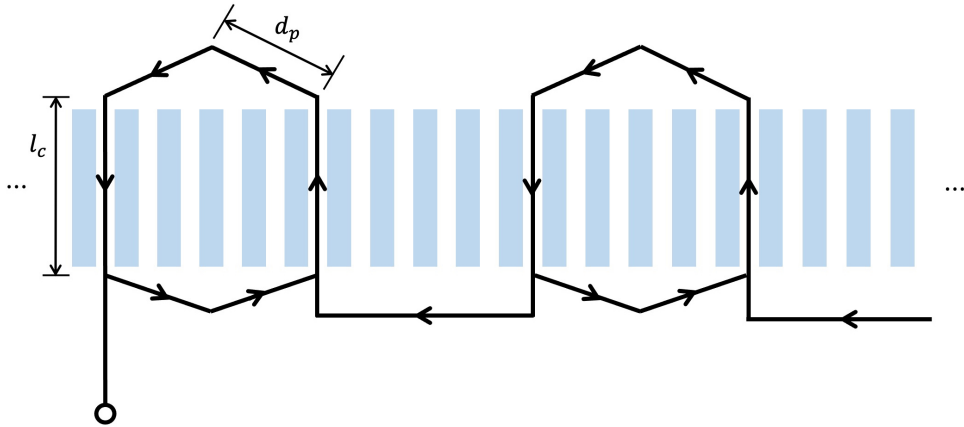

Figure 4.6: Winding layout of the distributed winding design for one phase winding

Assuming the slot size is known and fixed, the cross-sectional area of a single conductor or a

71

wire per slot can be calculated as follows:

$$A_c = k_{pf} \frac{A_s}{N_w}, \tag{4.58}$$

where k_{pf} is the packing factor, A_s is the cross-sectional area of the slot, and N_w is the number of turns per slot.

Then, the total volume of the distributed winding in all slots and the end-turn portions can be calculated as

$$V_{slot,dw} = \frac{N_p}{2} N_w A_c (2l_c), \tag{4.59}$$

$$V_{end,dw} = \frac{N_p}{2} N_w A_c (4d_p), \tag{4.60}$$

$$V_{total,dw} = V_{slot,dw} + V_{end,dw} = N_p N_w A_c (l_c + 2d_p), \tag{4.61}$$

where N_p is the number of poles of the winding, l_c is the length of the iron, and d_p is the half-length of the one-side of the end-turn.

Finally, the phase resistance of the distributed winding can be calculated as

$$R_{ph,dw} = \rho \frac{V_{total,dw}}{A_c^2}, \tag{4.62}$$

where ρ is the resistivity of a conductor.

4.2.4.2 Concentrated Winding Type

Modeling of a phase resistance using a concentrated winding type is presented. Figure 4.7 shows the winding layout of one phase of the concentrated winding.

Using Equation (4.58), the total volume of the concentrated winding in all slots and the end-
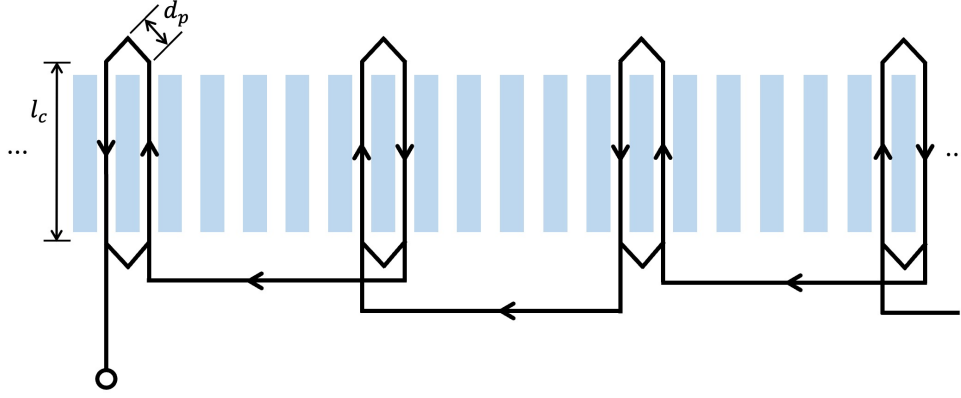
Figure 4.7: Winding layout of the concentrated winding design for one phase winding

turn portions can be calculated as

$$V_{slot,cw} = N_p N_w A_c (2l_c), \tag{4.63}$$

$$V_{end,cw} = N_p N_w A_c (4d_p) \tag{4.64}$$

$$V_{total,cw} = V_{slot,cw} + V_{end,cw} = 2N_p N_w A_c (l_c + 2d_p). \tag{4.65}$$

Hence, the phase resistance of the concentrated winding can be expressed as

$$R_{ph,cw} = \rho \frac{V_{total,cw}}{A_c^2}. \tag{4.66}$$

4.2.5 Voltage Equation

Using the flux-linkage and current relationship derived in the previous section, the dynamic voltage equation of the proposed machine can be expressed using the vector circuit model of the

73

two-phase AC stator in Figure 4.8.

Figure 4.8: Vector circuit model of two-phase AC stator including winding resistance

The dynamic voltage equation for all windings results in a vector-matrix form as follows:

$$
\begin{bmatrix} \vec{v}_s \\ v_t^r \\ v_f^r \end{bmatrix} = \begin{bmatrix} \mathbf{R}_s & 0 & 0 \\ 0 & R_t & 0 \\ 0 & 0 & R_f \end{bmatrix} 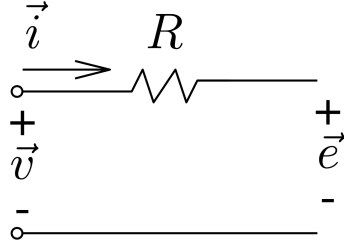\begin{bmatrix} \vec{i}_s \\ i_t^r \\ i_f^r \end{bmatrix} + \begin{bmatrix} \vec{e}_s \\ e_t^r \\ e_f^r \end{bmatrix} = \begin{bmatrix} \mathbf{R}_s & 0 & 0 \\ 0 & R_t & 0 \\ 0 & 0 & R_f \end{bmatrix} \begin{bmatrix} \vec{i}_s \\ i_t^r \\ i_f^r \end{bmatrix} + \frac{d}{dt} \begin{bmatrix} \vec{\lambda}_s \\ \lambda_t^r \\ \lambda_f^r \end{bmatrix}, \tag{4.67}
$$

where $\mathbf{R}_s$ the diagonal matrix with the phase resistance of the stator winding, R_t the phase resistance of the transformer winding, and R_f the phase resistance of the field winding.

4.2.6 Electromagnetic Torque

The electromagnetic torque can be derived using the co-energy approach which uses an expression of the field energy as a function of current and the electrical angle of the rotor. The co-energy expression for the proposed machine can be expressed as follows:

$$
W'_{co}(\vec{i}_{stf}, \theta_{re}) = \frac{1}{2} \vec{i}_{stf}^T \boldsymbol{L}_{stf}(\theta_{re}) \vec{i}_{stf}, \tag{4.68}
$$

where $\boldsymbol{L}_{stf}$ is the inductance matrix of all machine windings.

Using the co-energy expression, the electromagnetic torque can be derived by differentiating

the co-energy over the electrical angle of the rotor as follows:

$$\tau_{em} = \frac{dW'_{co}(\vec{i}_{stf}, \theta_{re})}{d\theta_{re}} \tag{4.69}$$

$$= \frac{1}{2}\vec{i}_{stf}^T \frac{d\boldsymbol{L}_{stf}(\theta_{re})}{d\theta_{re}}\vec{i}_{stf}, \tag{4.70}$$

where

$$\vec{i}_{stf} = \begin{bmatrix} \vec{i}_s \\ i_t^r \\ i_f^r \end{bmatrix}, \tag{4.71}$$

$$\frac{d\boldsymbol{L}_{stf}(\theta_{re})}{d\theta_{re}} = \begin{bmatrix} 0_{5x5} & \frac{d\vec{M}_{st}}{d\theta_{re}} & \frac{\vec{M}_{sf}}{d\theta_{re}} \\ \frac{d\vec{M}^T_{st}}{d\theta_{re}} & 0_{3x3} & \frac{\vec{M}_{tf}}{d\theta_{re}} \\ \frac{\vec{M}^T_{sf}}{d\theta_{re}} & \frac{\vec{M}^T_{tf}}{d\theta_{re}} & 0 \end{bmatrix}. \tag{4.72}$$

Furthermore, the torque expression can be simplified in terms of the d-q synchronous reference frame. For example, the torque for a five-phase machine design that uses the fundamental spatial harmonic component as a main torque-producing field and the third spatial harmonic component for generating the field current can be expressed as follows:

$$\tau_{em} = \frac{5N_p}{4}M_{sf}i_f i_{q1}, \tag{4.73}$$

where N_p is the number of poles, M_{sf} is the mutual inductance between the stator windings and the field winding, i_f is the field current, and i_{q1} is the quadrature-axis fundamental stator current. As the field current i_f is basically controlled by the third spatial harmonic current i_3, the torque of the machine is regulated by i_{q1} and i_3.

4.2.7 Magnetic Flux Density in Machine Irons

The magnetic flux density in the machine irons, such as teeth and back-iron portions, is an important factor to check whether the machine operates under the saturation level or not. In this

section, the magnetic flux densities in the stator teeth and back-iron portions are derived based on the flux-linkages of each phase windings derived from the flux-linkage and current relationship.

Figure 4.9 shows a five-phase stator winding with a full-pitch distributed winding type. A two-pole design is used to simplify the derivation process. It is assumed that the net magnetic flux out of any closed surface is zero. Using the symmetric property of the machine, the magnetic flux within the stator teeth can be defined as Φ_i $(i = 1, \cdots, 5)$. This approach can be easily applied for higher pole designs as well as the rotor iron.
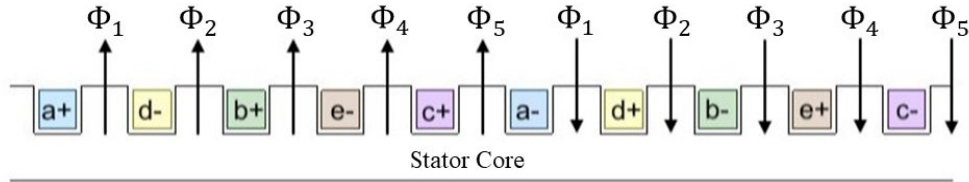

Figure 4.9: Five-phase, two-pole stator winding and magnetic fluxes in the stator teeth

By using the convention of a sign of each phase windings in the slots and fluxes in each tooth, the flux-linkage and magnetic flux relationship can be established as follows:

$$\lambda_a = N_s(\Phi_1 + \Phi_2 + \Phi_3 + \Phi_4 + \Phi_5), \tag{4.74}$$

$$\lambda_b = N_s(\Phi_3 + \Phi_4 + \Phi_5 - \Phi_1 - \Phi_2), \tag{4.75}$$

$$\lambda_c = N_s(\Phi_5 - \Phi_1 - \Phi_2 - \Phi_3 - \Phi_4), \tag{4.76}$$

$$\lambda_d = -N_s(\Phi_2 + \Phi_3 + \Phi_4 + \Phi_5 - \Phi_1), \tag{4.77}$$

$$\lambda_e = -N_s(\Phi_4 + \Phi_5 - \Phi_1 - \Phi_2 - \Phi_3). \tag{4.78}$$

The relationship can be expressed in a vector-matrix form as

$$
\begin{bmatrix} \lambda_a \\ \lambda_b \\ \lambda_c \\ \lambda_d \\ \lambda_e \end{bmatrix} = \boldsymbol{Q} \begin{bmatrix} \Phi_1 \\ \Phi_2 \\ \Phi_3 \\ \Phi_4 \\ \Phi_5 \end{bmatrix}, \tag{4.79}
$$

where

$$
\boldsymbol{Q} = N_s \begin{bmatrix} 1 & 1 & 1 & 1 & 1 \\ -1 & -1 & 1 & 1 & 1 \\ -1 & -1 & -1 & -1 & 1 \\ 1 & -1 & -1 & -1 & -1 \\ 1 & 1 & 1 & -1 & -1 \end{bmatrix}. \tag{4.80}
$$

Hence, the magnetic fluxes within the corresponding stator teeth can be calculated with known flux-linkages of the stator winding as follows:

$$
\begin{bmatrix} \Phi_1 \\ \Phi_2 \\ \Phi_3 \\ \Phi_4 \\ \Phi_5 \end{bmatrix} = \boldsymbol{Q}^{-1} \begin{bmatrix} \lambda_a \\ \lambda_b \\ \lambda_c \\ \lambda_d \\ \lambda_e \end{bmatrix}. \tag{4.81}
$$

As a result, the magnetic flux density corresponding to each stator tooth locations can be cal-

culated as follows:

$$\begin{bmatrix} B_1 \\ B_2 \\ B_3 \\ B_4 \\ B_5 \end{bmatrix} = \frac{1}{w_t l} \begin{bmatrix} \Phi_1 \\ \Phi_2 \\ \Phi_3 \\ \Phi_4 \\ \Phi_5 \end{bmatrix} = \frac{1}{w_t l} \cdot \boldsymbol{Q^{-1}} \begin{bmatrix} \lambda_a \\ \lambda_b \\ \lambda_c \\ \lambda_d \\ \lambda_e \end{bmatrix}, \tag{4.82}$$

where w_t is the width of the stator tooth and l is the length of the stator iron.

Moreover, the magnetic flux density distribution in the stator back-iron can be derived using the conservation of flux equation, which is denoted as

$$\sum_{n=1}^{N} \Phi_n = 0. \quad n = 1, \cdots, N \tag{4.83}$$

Using Figure 4.10, the relationship between the magnetic fluxes in the stator back-iron and the fluxes in the teeth can be expressed as follows:

$$\Phi_{b1} = \frac{1}{2}(\Phi_1 + \Phi_2 + \Phi_3 + \Phi_4 + \Phi_5), \tag{4.84}$$

$$\Phi_{b2} = \Phi_{b1} - \Phi_1 = \frac{1}{2}(-\Phi_1 + \Phi_2 + \Phi_3 + \Phi_4 + \Phi_5), \tag{4.85}$$

$$\Phi_{b3} = \Phi_{b2} - \Phi_2 = \frac{1}{2}(-\Phi_1 - \Phi_2 + \Phi_3 + \Phi_4 + \Phi_5), \tag{4.86}$$

$$\Phi_{b4} = -\Phi_{b3} + \Phi_3 = \frac{1}{2}(\Phi_1 + \Phi_2 + \Phi_3 - \Phi_4 - \Phi_5), \tag{4.87}$$

$$\Phi_{b5} = \Phi_{b4} + \Phi_4 = \frac{1}{2}(\Phi_1 + \Phi_2 + \Phi_3 + \Phi_4 - \Phi_5). \tag{4.88}$$
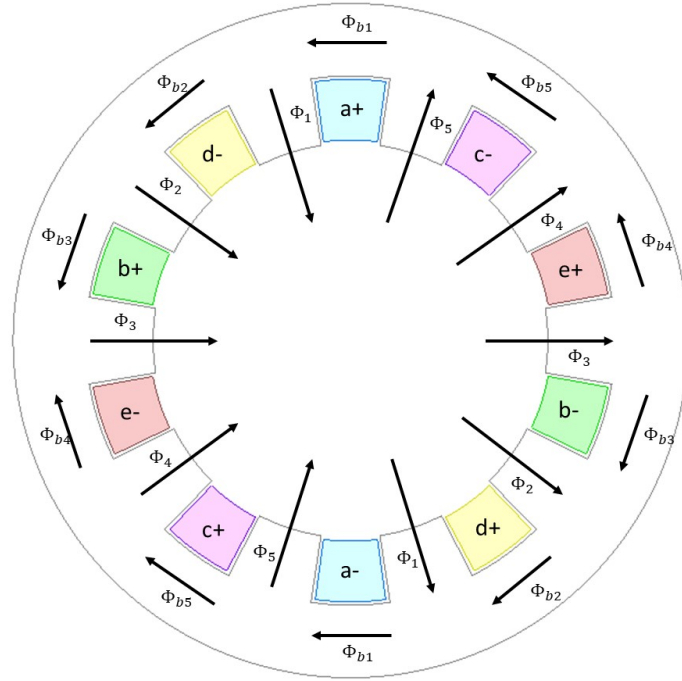
Figure 4.10: Cross-sectional view of the five-phase, two-pole stator with magnetic flux distributions

The relationship can be expressed in a vector-matrix form as

$$
\begin{bmatrix} \Phi_{b1} \\ \Phi_{b2} \\ \Phi_{b3} \\ \Phi_{b4} \\ \Phi_{b5} \end{bmatrix} = \boldsymbol{K} \begin{bmatrix} \Phi_1 \\ \Phi_2 \\ \Phi_3 \\ \Phi_4 \\ \Phi_5 \end{bmatrix},
\tag{4.89}
$$

where

$$
\boldsymbol{K} = \frac{1}{2} \begin{bmatrix} 1 & 1 & 1 & 1 & 1 \\ -1 & 1 & 1 & 1 & 1 \\ -1 & -1 & 1 & 1 & 1 \\ 1 & 1 & 1 & -1 & -1 \\ 1 & 1 & 1 & 1 & -1 \end{bmatrix}.
\tag{4.90}
$$

79

As a result, the magnetic flux density in the stator back-iron can be calculated as follows:

$$
\begin{bmatrix} B_{b1} \\ B_{b2} \\ B_{b3} \\ B_{b4} \\ B_{b5} \end{bmatrix} = \frac{1}{w_{bi}l} \begin{bmatrix} \phi_{b1} \\ \phi_{b2} \\ \phi_{b3} \\ \phi_{b4} \\ \phi_{b5} \end{bmatrix} = \frac{1}{w_{bi}l} \cdot \boldsymbol{K} \begin{bmatrix} \Phi_1 \\ \Phi_2 \\ \Phi_3 \\ \Phi_4 \\ \Phi_5 \end{bmatrix} ,
\tag{4.91}
$$

where w_{bi} is the thickness of the stator back-iron.

4.3 Rotor Rectifier Model

The proposed electric machine has a diode rectifier circuit in the rotor that connects between the transformer winding and the field winding to convert an AC current produced in the transformer winding into a DC current in the field winding. A full-bridge single-phase rectifier diagram for a single-phase transformer winding is shown in Figure 4.11. The v_t represents an AC voltage or EMF induced in the transformer winding and v_f represents a voltage in the field winding.
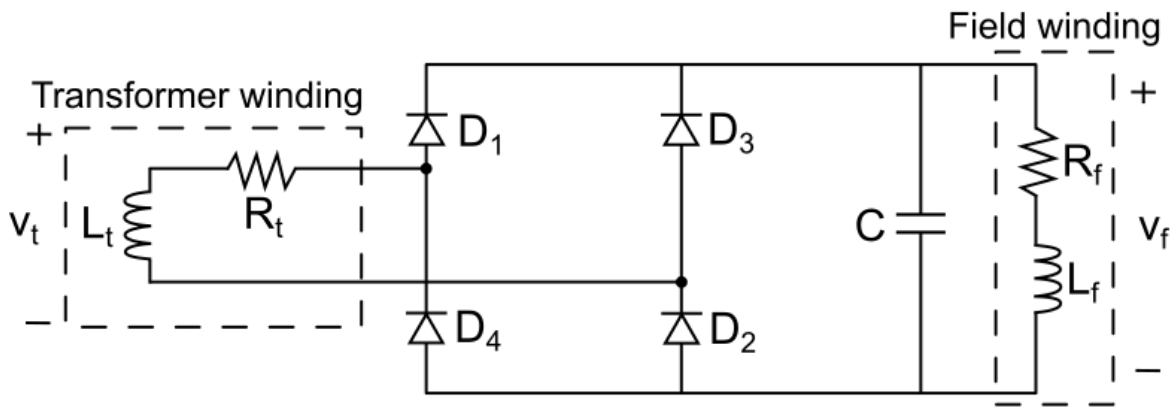

Figure 4.11: A full-bridge single-phase rectifier for a single-phase transformer winding

In proper operation, the diodes $D1, D2, D3,$ and $D4$ in Figure 4.11 are in one of two states as follows:

- State 1: $D1$ and $D2$ on, $D3$ and $D4$ off, or

- State 2: $D1$ and $D2$ off, $D3$ and $D4$ on.

It is assumed that the induced AC voltage of the transformer winding is a pure sinusoidal waveform as shown in Figure 4.12a. When the transformer voltage is a positive cycle $\left(0 \leq t < \frac{T_t}{2}\right)$, the diodes are in State 1, and the output voltage results in $v_f = v_t$. When the transformer voltage is a negative cycle $\left(\frac{T_t}{2} \leq t < T_t\right)$, the diodes are in State 2, and the output voltage becomes $v_f = -v_t$.

Hence, the resulting voltage in the field winding becomes always positive. Since a capacitor is connected in parallel with the field winding inductance and resistance, the output voltage in the field winding results in a relatively constant voltage, as shown in Figure 4.12b.
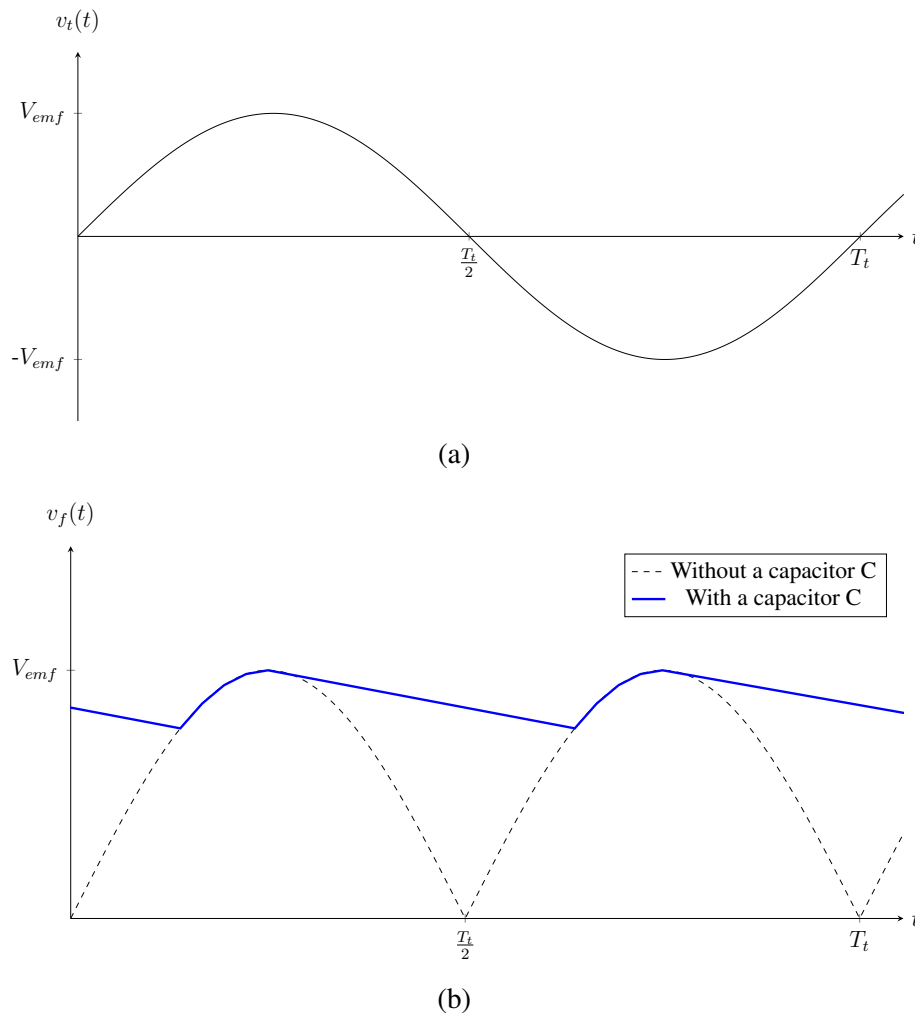

(a)

(b)

Figure 4.12: A full-bridge single-phase rectifier: (a) an induced voltage in transformer winding (b) an output voltage in field winding.

A full-bridge three-phase rectifier diagram for a three-phase transformer winding is shown in Figure 4.13. The v_{ta}, v_{tb}, and v_{tc} represent AC voltages or EMFs of each phase of the transformer windings, and the circuit consists of six diodes for each phases.

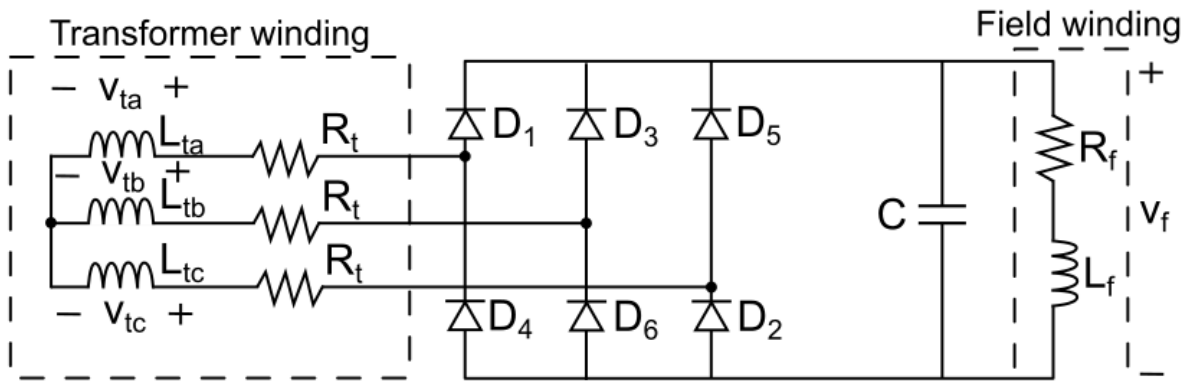In proper operation, the diodes $D1, D2, D3, D4, D5$ and $D6$ in Figure 4.13 are in one of six states as follows:

Figure 4.13: A full-bridge three-phase rectifier for a three-phase transformer winding

- State 1: $D1$ and $D2$ on, $D3, D4, D5$ and $D6$ off, or

- State 2: $D2$ and $D3$ on, $D1, D4, D5$ and $D6$ off, or

- State 3: $D3$ and $D4$ on, $D1, D2, D5$ and $D6$ off, or

- State 4: $D4$ and $D5$ on, $D1, D2, D3$ and $D6$ off, or

- State 5: $D5$ and $D6$ on, $D1, D2, D3$ and $D4$ off, or

- State 6: $D1$ and $D6$ on, $D2, D3, D4$ and $D5$ off.

The induced three-phase AC voltages in the transformer windings are shown in Figure 4.14a. When the phase-a voltage of the transformer is the highest, and the phase-c voltage is the lowest, the diodes are in State 1, therefore the output voltage results in $v_f = v_{ta} - v_{tc}$. Likewise, when the phase-c voltage of the transformer is the highest, and the phase-a voltage is the lowest, the diodes are in State 4, hence the output voltage becomes $v_f = v_{tc} - v_{ta}$. Moreover, a parallel-connected capacitor at the output makes the output voltage in the field winding relatively constant, as shown in Figure 4.14b.
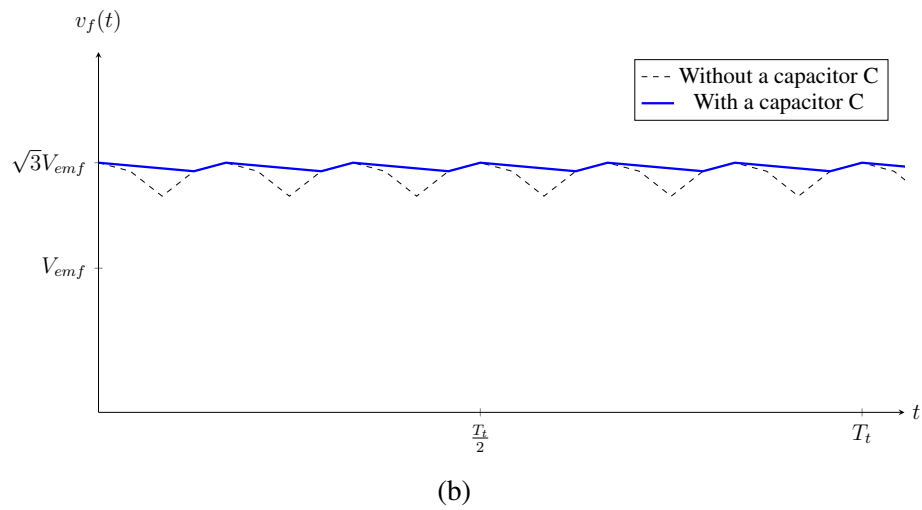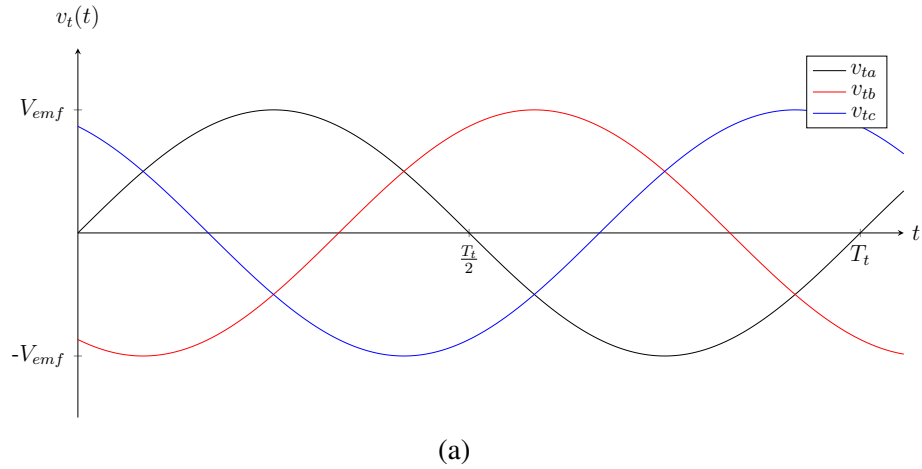
(a)

(b)

Figure 4.14: A full-bridge three-phase rectifier: (a) induced three-phase voltages in transformer winding (b) an output voltage in field winding.

For the proposed machine, a silicon carbide diode in [47] is used for the diode model thanks to its high breakdown voltage advantageous for the operating specifications of the proposed machine.

4.4 Lumped-parameter Model using MATLAB and Simulink

The lumped-parameter model of the proposed machine is constructed for simulations using MATLAB and Simulink. Figure 4.15 shows a Simulink overview containing a five-phase machine model and a current regulator based on the FOC technique. The five-phase inverter model is not presented in this Simulink model for simplification.
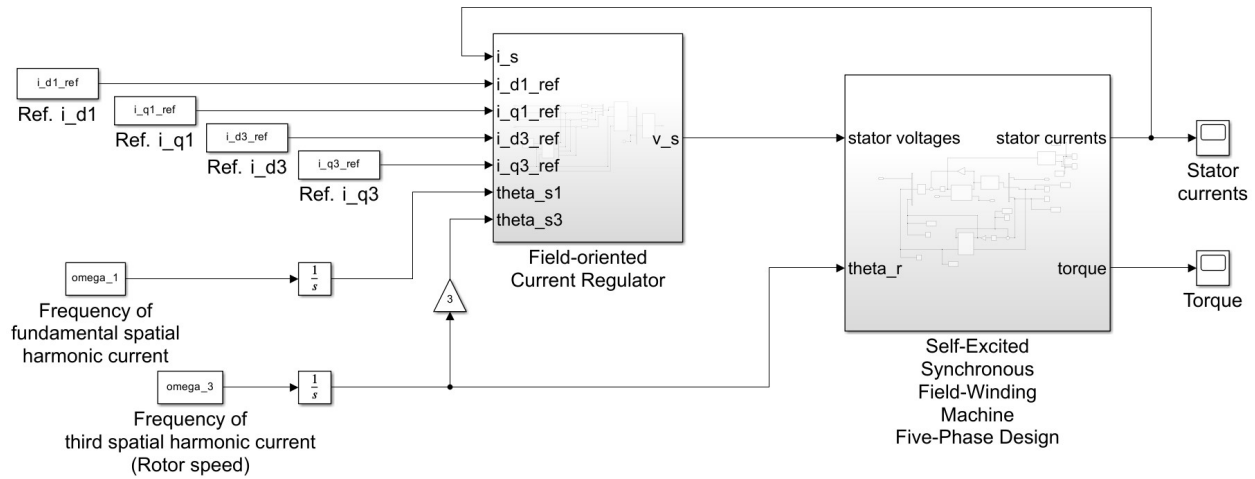

Figure 4.15: Simulink model of a five-phase machine design using the third spatial harmonic as a main rotating frequency

The inputs of the field-oriented current regulator subsystem are the two pairs of reference stator currents, measured output stator currents from the machine subsystem, and two angular positions of the reference stator currents. Each pair of the reference direct and quadrature (d-q) stator currents produces the corresponding fundamental and third spatial harmonics independently. One of the angular positions corresponds to a frequency of the third spatial harmonic currents and is synchronized to the rotor position while the second angular position corresponds to a frequency of the fundamental spatial harmonic currents that are independently controlled. The role of the two spatial harmonic components can be switched based upon the winding designs of machines.

The subsystem of the FOC-based current regulator is shown in Figure 4.16. It contains two pairs of proportional-integral (PI) controllers for individual reference currents. The Clarke and

Park transformations for the five-phase stator winding convert the measured five-phase stator currents into the equivalent d-q currents and are used to generate four error signals. The two angular positions are used for the Park transformation. The outputs of the PI controllers are reference voltages in the d-q frame which are then converted again to the five-phase voltages as inputs to the machine subsystem.
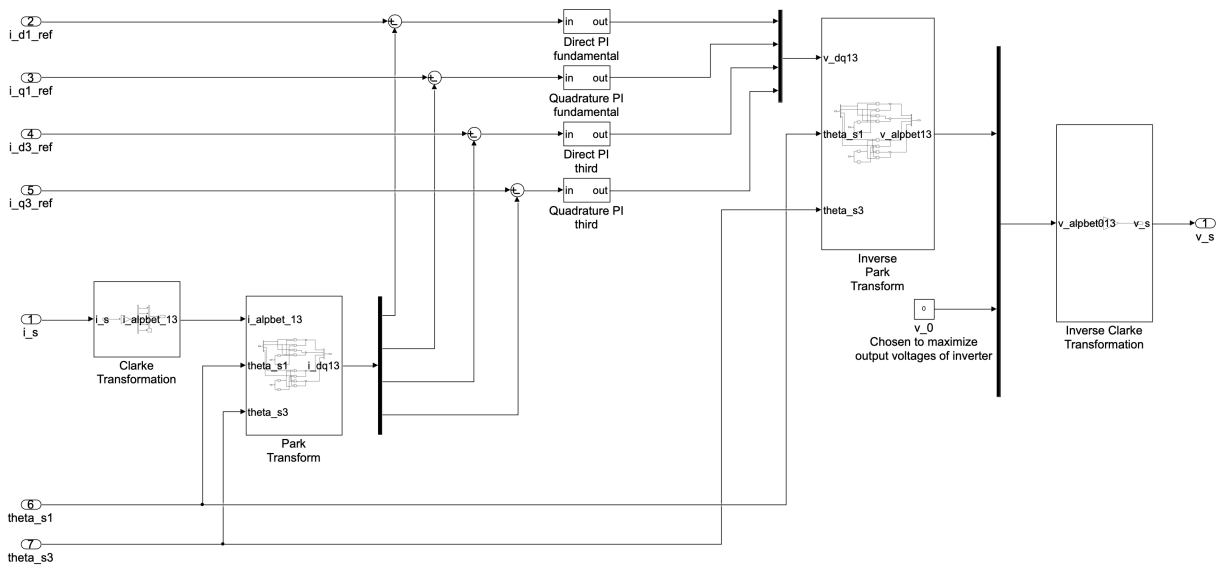

Figure 4.16: Simulink subsystem of FOC-based current regulator

The subsystem of the proposed machine is shown in Figure 4.17. In this subsystem, the reference five-phase voltages from the controller and the voltages in the transformer winding and the field winding are first converted into the two-phase values using the Clarke transformation. The voltages in the transformer and field windings are calculated from the corresponding output currents and a diode rectifier through a feedback loop. In the Clarke transformations of all windings, the zero-sequence voltage components of the stator winding or the transformer winding are constrained to be zero, therefore removed by the star-connected or wye-connected configurations.
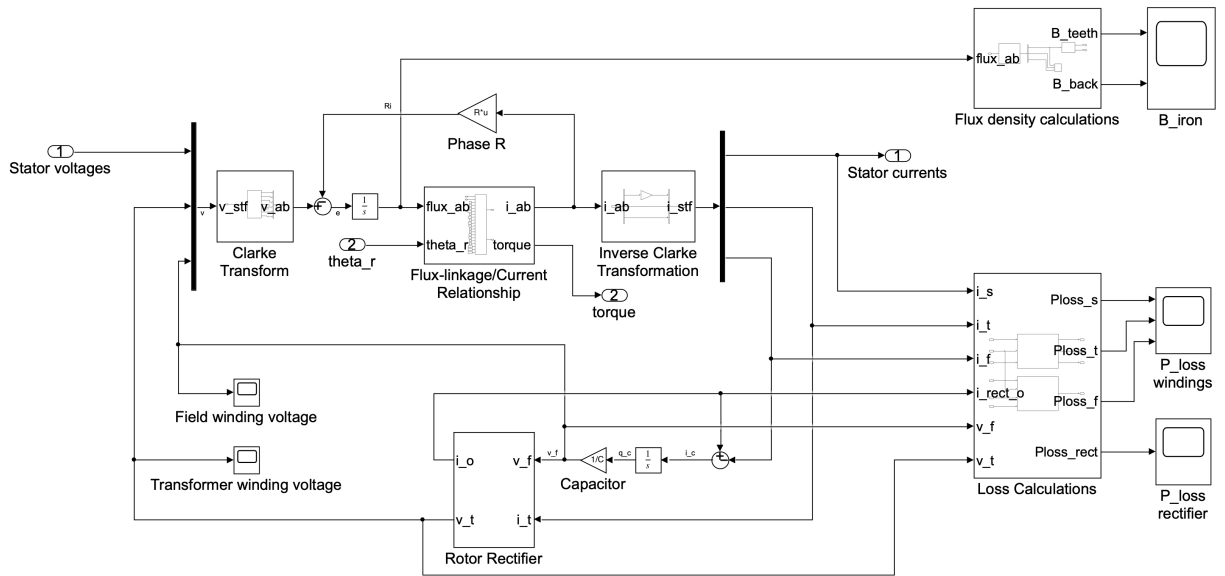
86

Figure 4.17: Simulink subsystem of proposed electric machine

The core of the machine subsystem is a MATLAB function block which contains calculations based upon the flux-linkage and current relationship and torque derived in previous Chapters. Figure 4.18 shows the details of the MATLAB function block including inputs of the flux-linkages of all windings calculated from the voltage equation, the rotor position, and all parameters relevant to the machine geometry (e.g., air-gap length and radius, stack length, the number of turns and pole pitch for all windings, and leakage inductances).

The currents of the transformer and field windings are used as inputs for the diode rectifier model which is shown in Figure 4.19. For the implementation of the single- or three-phase diode rectifier in MATLAB and Simulink simulation tool, a modified systems-based power electronic circuit model based on the work presented in [47] is used to capture robust and accurate simulation results. The nonlinear $i-v$ characteristics for the diodes result in more accurate conduction losses, therefore it can capture breakdown phenomena more accurately than using the generic piecewise
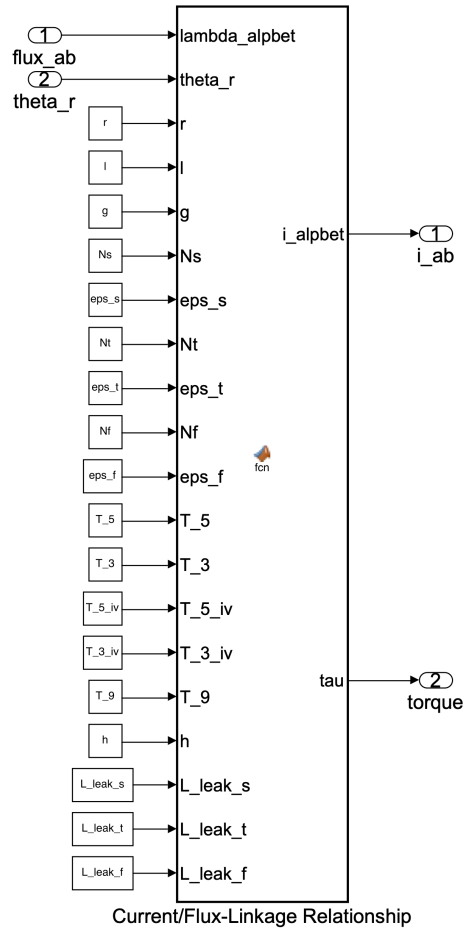
Figure 4.18: Simulink subsystem of current and torque calculations

linear models. Using the rectifier model, the voltages of the transformer and field windings are calculated and complete the feedback loop inside the machine subsystem.

The resulting currents of all windings in the equivalent two-phase values are converted back to the respective stationary reference frames using the inverse Clarke transformation. The five-phase stator currents become outputs of the machine model which is also used for the current regulator. Moreover, two post-processing blocks calculate flux densities in the stator teeth and back-iron regions and power losses, including conduction losses of all windings and diode losses in the rectifier.
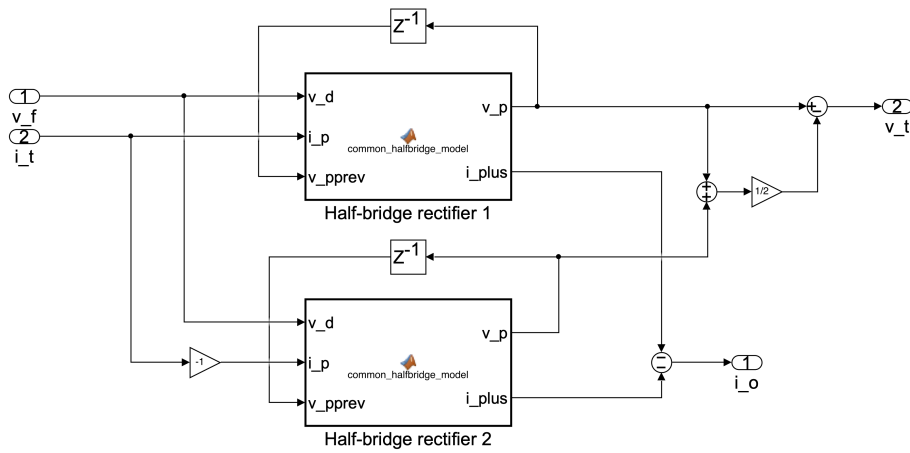
(a)
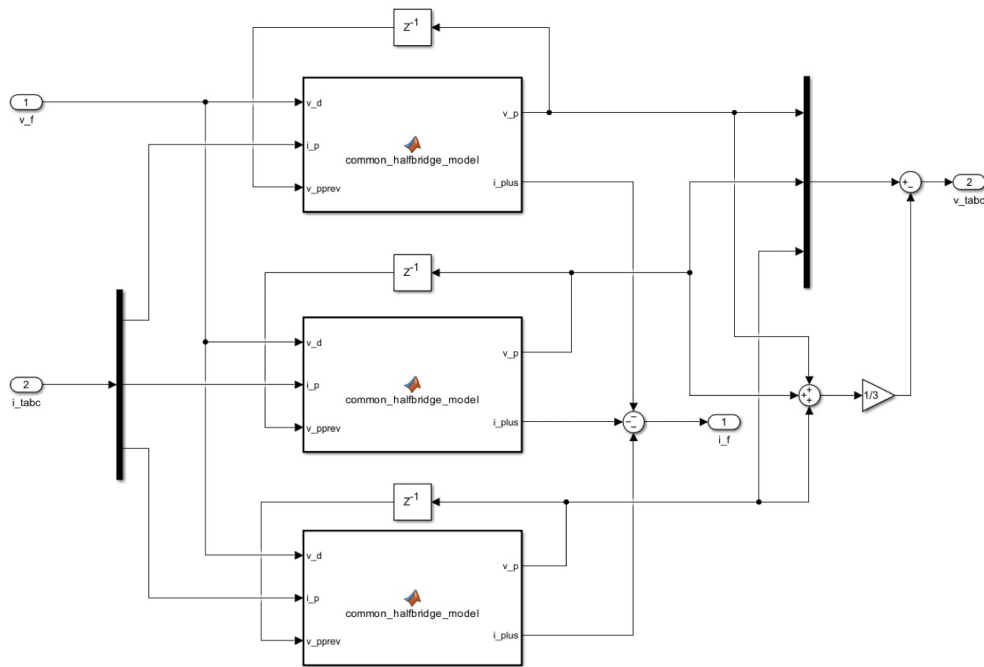
(b)

Figure 4.19: Simulink subsystem of the rotor diode rectifier (a) single-phase diode rectifier (b) three-phase diode rectifier

4.4.1 Proposed Harmonic Excitation Tests via MATLAB and Simulink Simulations

The developed MATLAB and Simulink simulation tools allow us to verify the proposed harmonic excitation scheme and investigate machine parameters relatively quickly. In this section, a machine design with a five-phase stator winding, a three-phase transformer winding, and a field winding is used. The fundamental spatial harmonic couples with the transformer windings, and the third spatial harmonic couples with the field winding. The following three simulation results verify the operating principle of the brushless machine topology.
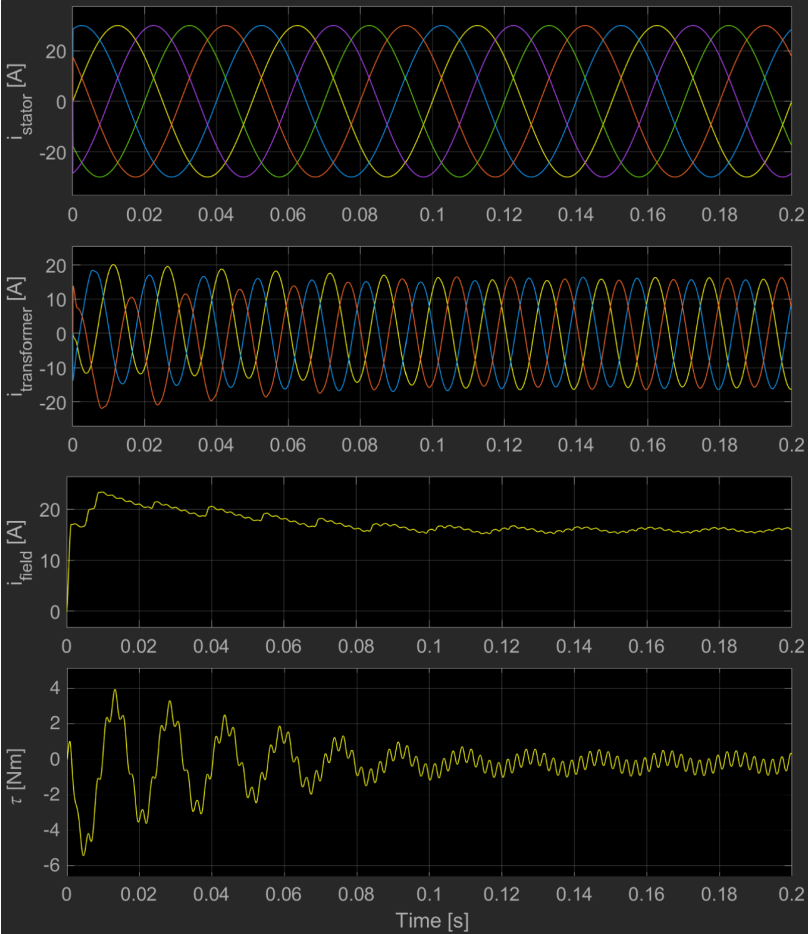

Figure 4.20: Simulink simulation of fundamental spatial harmonic current excitation

In Figure 4.20, the fundamental spatial harmonic currents are injected into the stator windings to excite the three-phase transformer windings. The induced voltages in the three-phase trans-

former windings generate a DC current in the field winding through a diode rectifier. This excitation does not produce the desired torque, as the third spatial harmonic currents are not injected in the stator winding, but is meant to demonstrate that the field current can be independently produced by the fundamental spatial harmonic component.
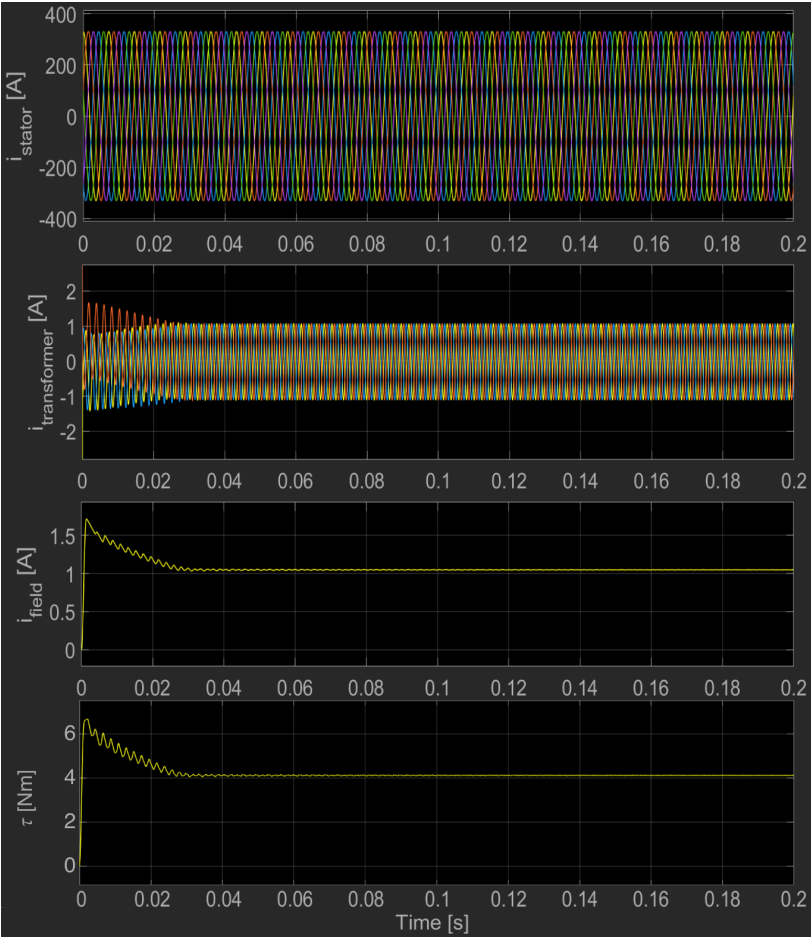

Figure 4.21: Simulink simulation of third spatial harmonic current excitation

In Figure 4.21, the third spatial harmonic currents are injected into the stator windings to demonstrate the degree of independency of excitation in the transformer windings. The third spatial harmonic currents, which are synchronized with the rotating frequency, are mainly used to interact with the rotor magnetic field to produce torque. Since the transformer windings are excited with the fundamental spatial harmonic component by design, the induced transformer voltages using the third spatial harmonic currents are small when compared to those generated by the fundamental

currents. These induced voltages are generated due to the slot harmonics of the stator and harmonic coupling between some sub-harmonic components between the stator and transformer MMFs.
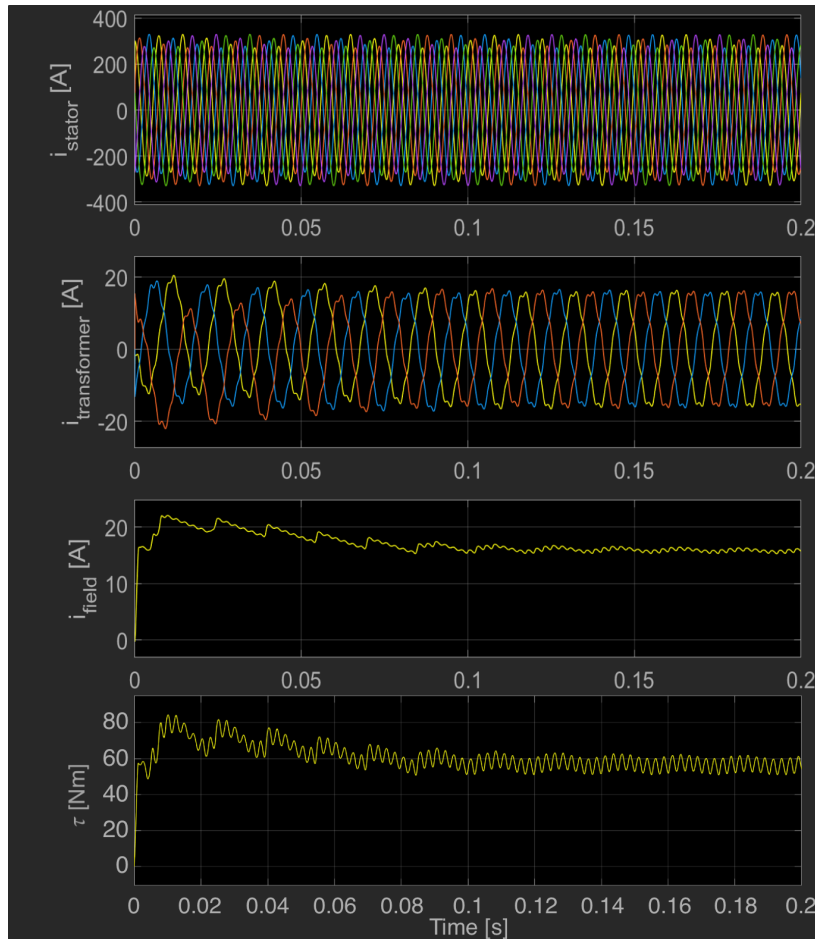

Figure 4.22: Simulink simulation of both fundamental and third spatial harmonic current excitation

In Figure 4.22, both fundamental and third spatial harmonic currents are injected simultaneously into the stator windings to demonstrate the torque production capability of the proposed design approach. The three-phase transformer windings are excited through the fundamental spatial harmonic component and produce the DC current and rotor field while the third spatial harmonic component interacts with the rotor field to produce the desired torque.

4.5   Finite Element Analysis (FEA) Model using ANSYS Maxwell

The finite element analysis model of the proposed machine is created using ANSYS Electromagnetics Suite for accurate simulations of the machine behavior, such as nonlinear magnetic behaviors, magnetic saturations, and core losses of the machine. For a faster simulation process and using its symmetrical property of the designs, a single-pole or single-pole-pair section of the full machine model is implemented in the ANSYS Maxwell as shown in Figure 4.23. Both machine designs have a five-phase stator design that is arranged using a full-pitch distributed winding type with a single-pole per slot per phase configuration. The stator windings are designed in a way that the magnetic fields produced by each phase have a phase shift of 72° each other.
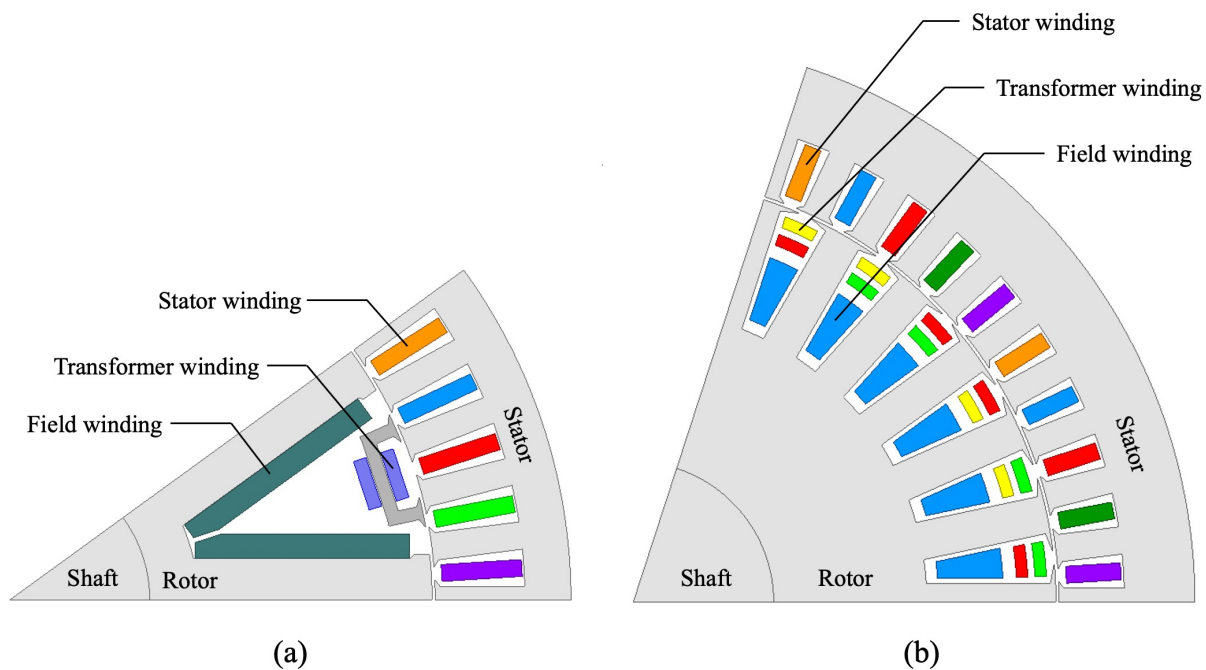

Figure 4.23: ANSYS Maxwell 2D Models: (a) Single-pole machine model based on single-phase transformer, (b) Single-pole-pair machine model based on three-phase transformer

The first machine design, as shown in Figure 4.23a, has a single-phase transformer winding design and a field winding on the rotor. Both the transformer and field windings are wound using a concentrated winding type. The transformer windings are wound around the back-iron portion

93

of the transformer core instead of its tooth region in order to maximize the space utilization of the rotor slot area. Hence, each transformer winding is oriented horizontally along with the back-iron of the transformer core whereas the field winding is in a vertical position.

The magnetic cores for the transformer windings are created separately and are placed between each field-pole rotor tooth. The width of the transformer cores is designed so that the stator MMF at the third spatial harmonic can enter from one side of the transformer core and exit to another side creating harmonic couplings between the stator and transformer windings.

The second machine design, as shown in Figure 4.23b, has a non-salient pole rotor design with a multi-layer winding structure for both the transformer and field windings. The transformer windings have a three-phase design wound using a distributed winding layout, and the field winding is wound using a concentrated winding layout.

The rotor of both machine designs contains a single- or three-phase diode rectifier model built using ANSYS Maxwell Circuit Design package, as shown in Figures 4.24 and 4.25. The phase inductance and resistance of the transformer windings including the end-turn portion are located at the input terminals (left side) of the rectifier, and the field winding components are connected at the output terminals (right side).

The completed rectifier models are imported into the machine models in ANSYS Maxwell 2D using the external circuit excitation settings for the transformer and field windings.
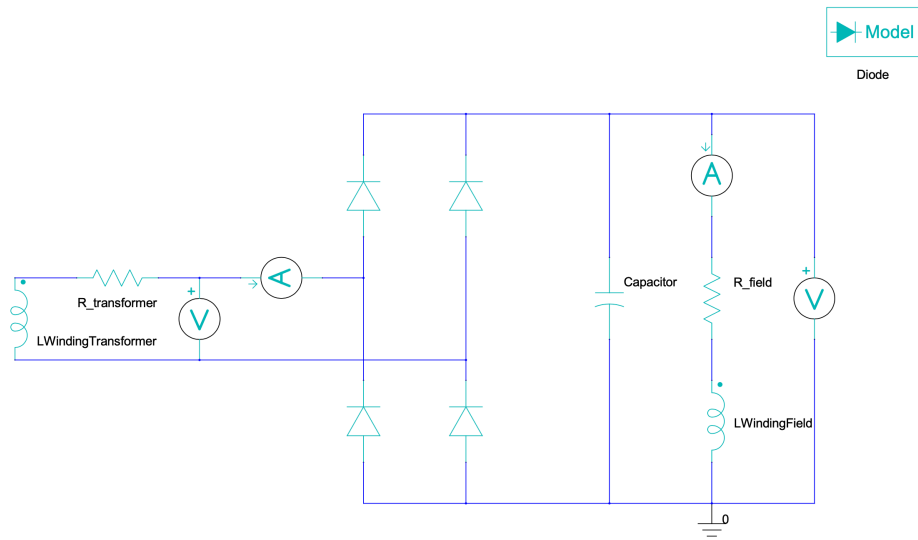
Figure 4.24: Rotor rectifier implementation in ANSYS Maxwell Circuit Design for single-phase transformer design
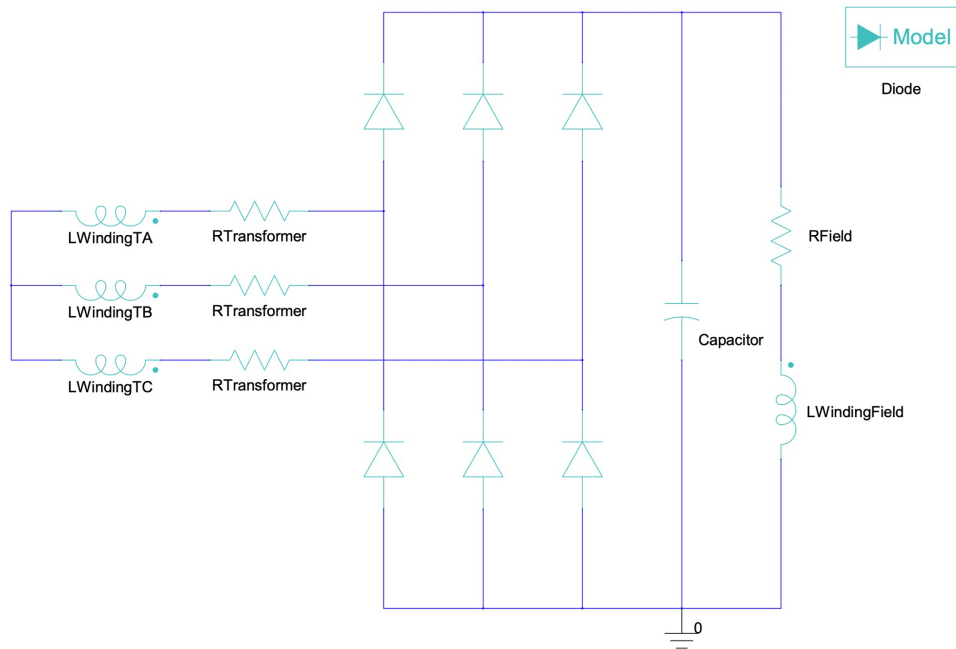

Figure 4.25: Rotor rectifier implementation in ANSYS Maxwell Circuit Design for three-phase transformer design
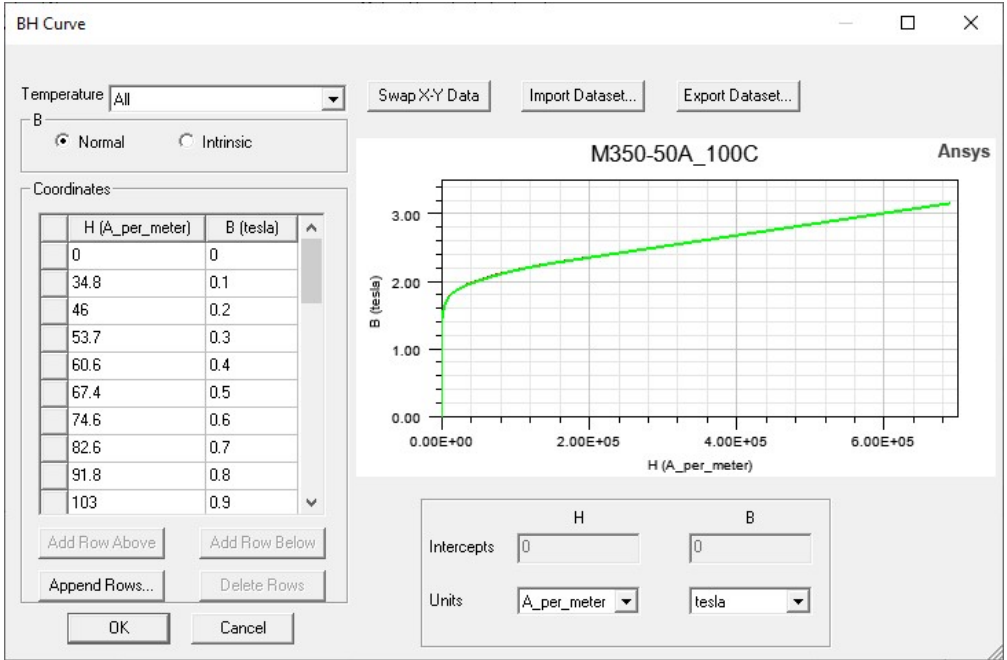
Figure 4.26: B-H Characteristic of M350-50A Steel in ANSYS Maxwell Model

4.5.1 Validation Test of FEA Model with MATLAB and Simulink Model

The FEA model built using ANSYS Maxwell and Circuit Design needs to be validated since the presence of a diode rectifier on the rotor is a unique design for the proposed machine topology. The FEA model is excited with both the fundamental and third spatial harmonic currents to produce torque. The simulation results of the FEA model are compared with the MATLAB and Simulink simulations. For a fair comparison, the properties of the materials in the FEA model are temporarily switched to a linear model since the MATLAB and Simulink model is a linear magnetics model, where a relationship between the magnetic flux density (B) and the magnetic field strength (H) is linear. This test is meant to validate the functions of the diode rectifier and communications between the machine model in ANSYS Maxwell and the circuit model in ANSYS Circuit Design.

Simulation results of the MATLAB and Simulink model are shown in Figure 4.27 and 4.28, and the FEA simulation results are shown in Figure 4.29 and 4.30. The simulation results of the FEA model are closely matched with the simulations from the MATLAB and Simulink model and the FEA model. Note that some deviations in the simulation results occur because the MATLAB and Simulink model does not account for the shape of the stator and rotor cores, such as the slotting effect.
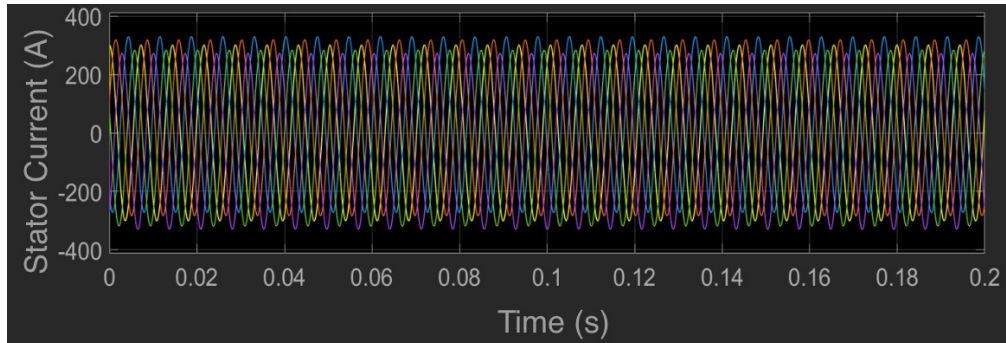
(a)
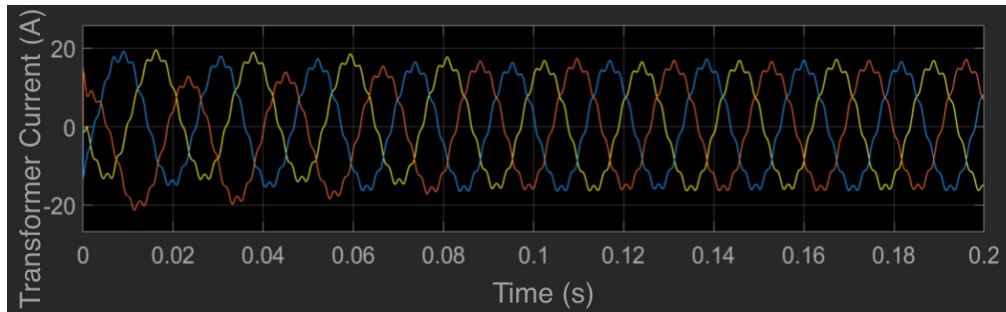
(b)
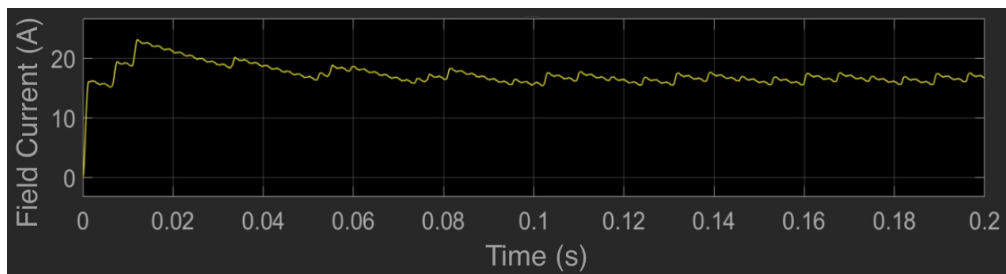
(c)

Figure 4.27: Simulation of MATLAB and Simulink model for Validation test. (a) Stator currents with both fundamental and third spatial harmonics. (b) Three-phase transformer currents. (c) Rotor field current.

(a)

(b)

Figure 4.28: Simulation of MATLAB and Simulink model for Validation test. (a) Three-phase transformer voltages. (b) Torque.

(a)
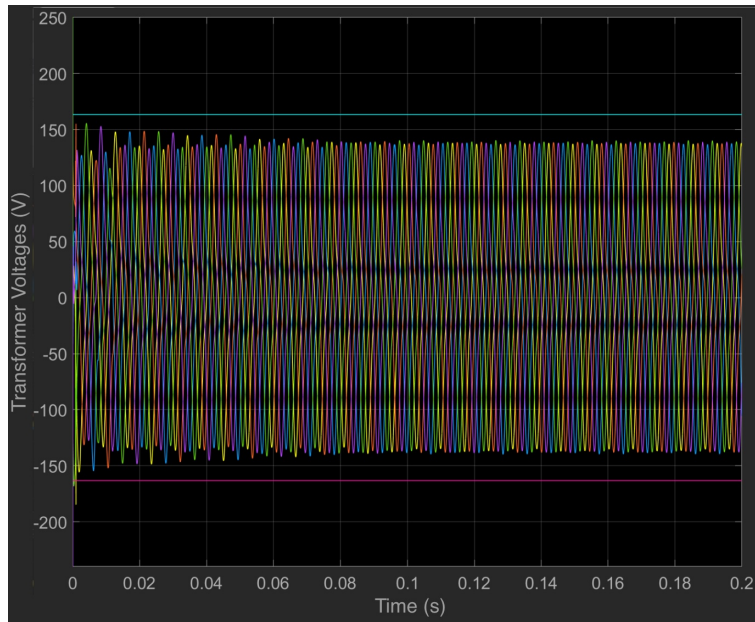

(b)
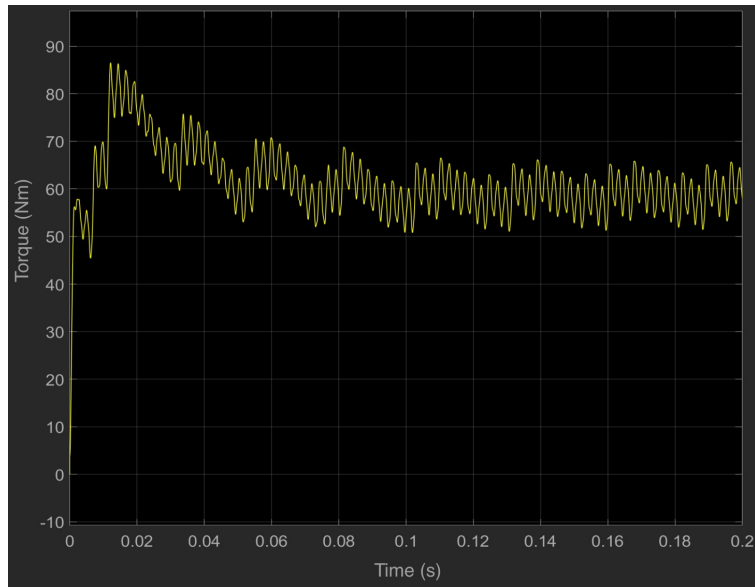

(c)

Figure 4.29: Simulation of ANSYS Maxwell model for Validation test. (a) Stator currents with both fundamental and third spatial harmonics. (b) Three-phase transformer currents. (c) Rotor field current.
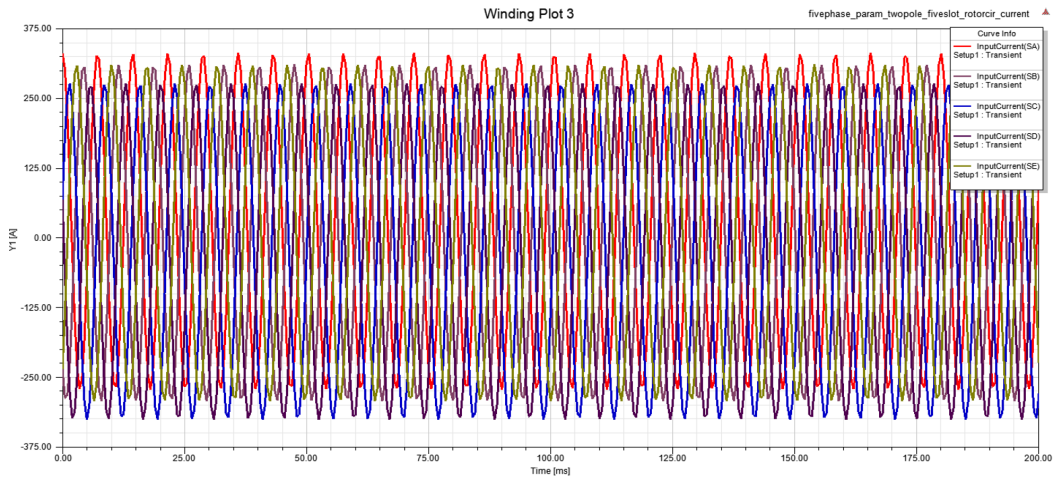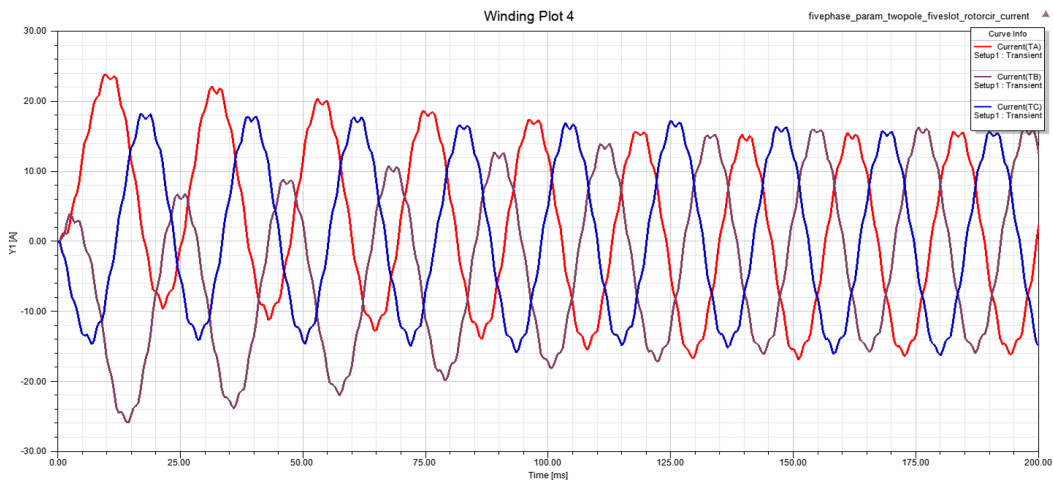
100

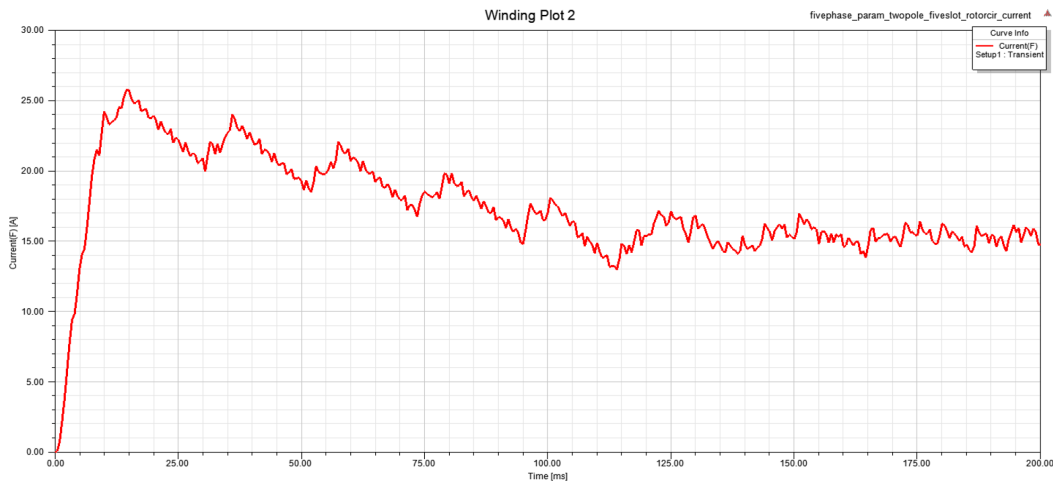Winding Plot 8

(a)

Torque Plot 1
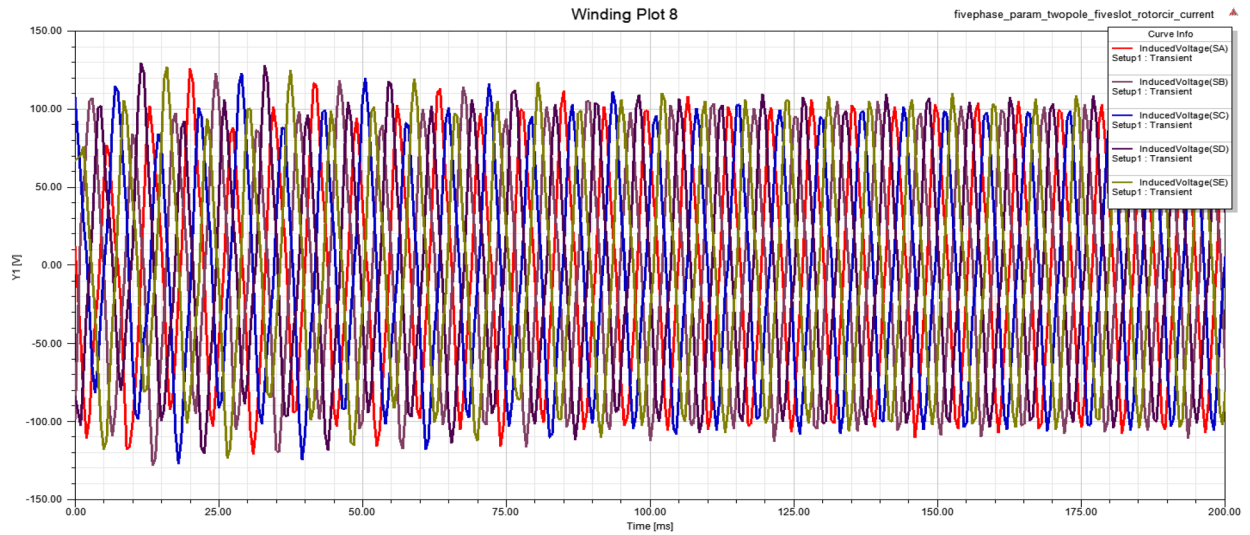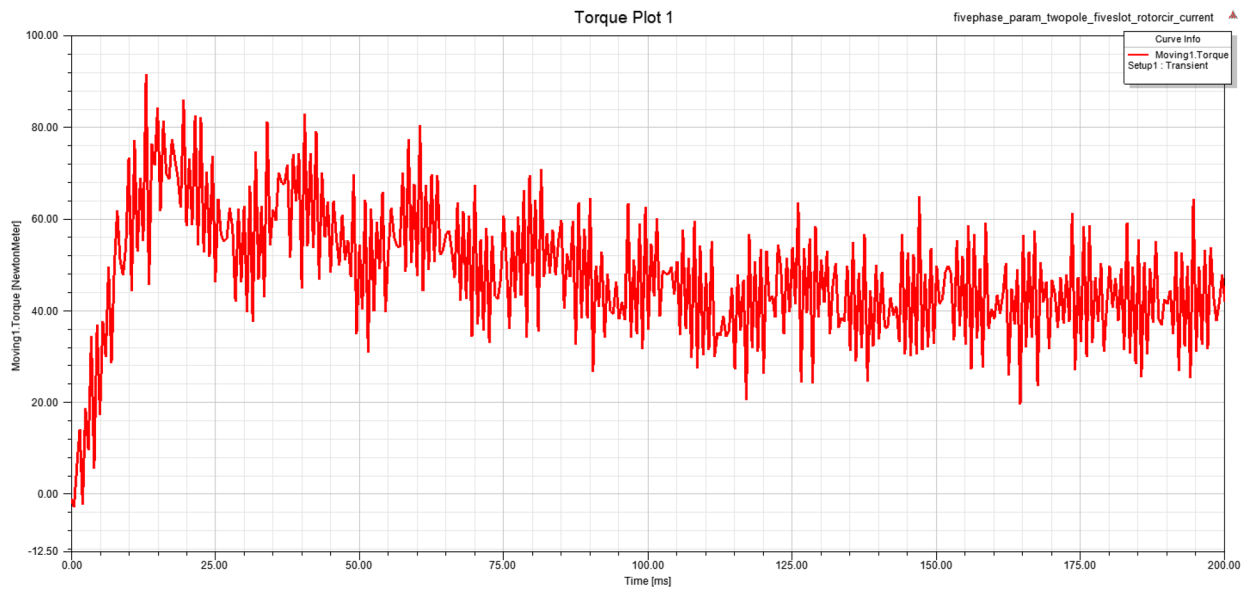
(b)

Figure 4.30: Simulation of ANSYS Maxwell model for Validation test. (a) Three-phase transformer voltages. (b) Torque.

4.6   Distributed and Concentrated Winding Designs

The stator windings can be arranged in various ways which change the overall spatial harmonic contents in the total stator MMF waveform and magnetic flux distributions in the machine cores. Different winding designs also affect the number of slots and layers required for the machine cores.
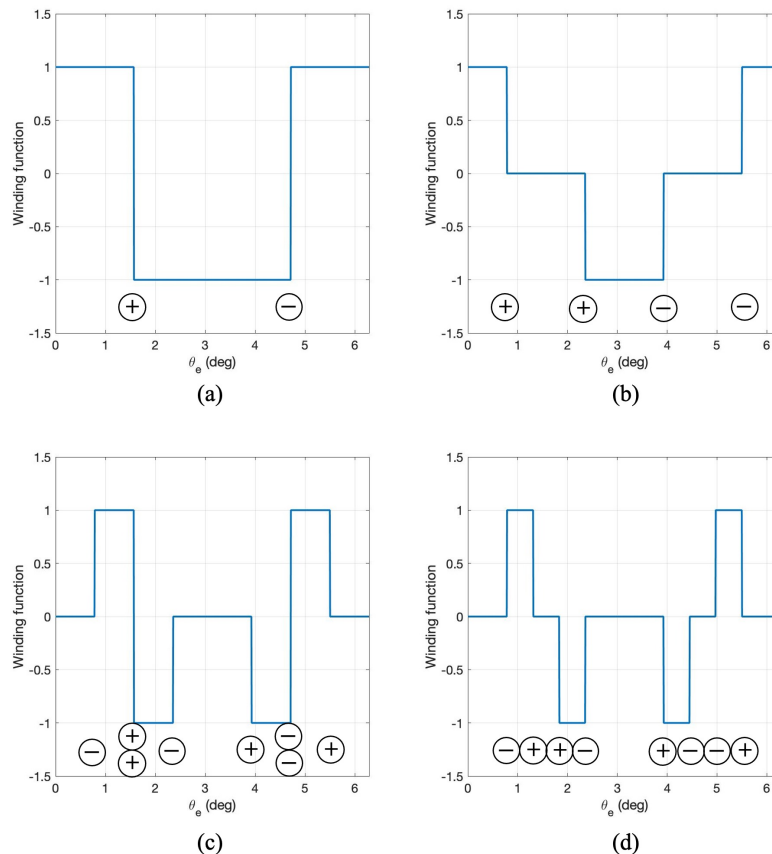
Figure 4.31: Different stator winding arrangements: (a) 1 SPP, (b) 2 SPP, (c) 3 SPP, and (d) 4 SPP

Figure 4.31 shows four winding designs for one phase with different numbers of slots per pole per phase (SPP). Each figure represents an MMF waveform per unit current over one period in an electrical angle. For example, the MMF of 1 SPP in Figure 4.31a corresponds to a full-pitch distributed winding configuration. The MMF of 2 SPP in Figure 4.31b represents either a concentrated winding or a fractional-pitch distributed winding configuration. Lastly, the MMFs of 3 and 4 SPP in Figures 4.31c and 4.31d are other possible winding arrangements that require

102

higher numbers of slots or layers per pole in the stator.

For applications requiring high power capability and high torque performance, it is desired that electric machine designs possess a large number of poles. However, increasing the number of poles in the machine design proportionally increases the total number of slots in the stator core. Using the five-phase stator winding design can increase the number of slots in the stator by roughly 67% compared to the three-phase stator design. A simulation test shows that the 3 and 4 SPP winding designs result in higher magnetic flux densities in the stator core than the 1 and 2 SPP designs due to the requirement of three to four times more numbers of slots in the stator core. Moreover, the large numbers of slots in the stator are undesired because of the manufacturing difficulty. For these reasons, the winding designs of the 1 and 2 SPPs (or distributed and concentrated winding designs) are considered for the proposed machine design.

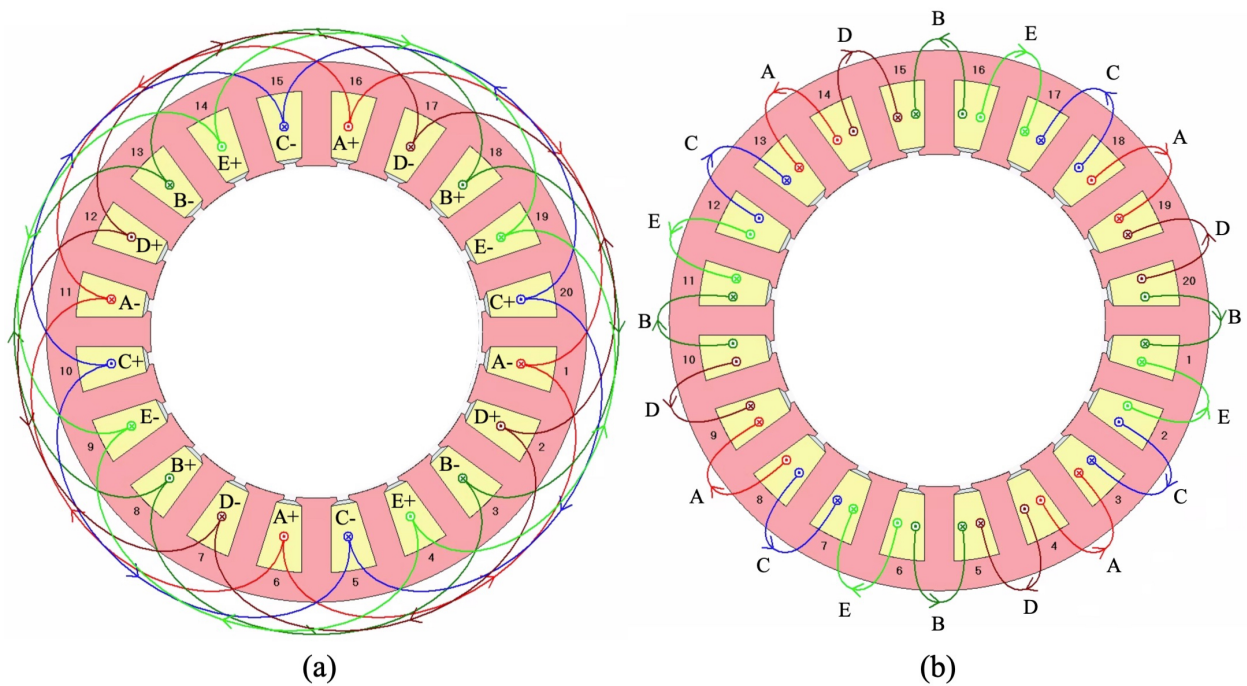Figure 4.32: Five-phase, four-pole stator winding layout using (a) Full-pitch distributed winding design (b) Concentrated winding design

The distributed winding design is a winding type that has a coil arrangement as shown in Figure 4.32a. Coils of each phase are positioned across multiple number slots along the air-gap periphery

creating wide magnetic poles. This winding design can be arranged in either a full-pitch or a fractional-pitch manner, and the number of slots spanning one pole can be varied. The concentrated winding design has a coil arrangement as shown in Figure 4.32b. Each coil of this winding design is wound around each tooth creating magnetic poles. Both winding designs have their own merits and demerits. This section focuses on the MMF waveform and its winding coefficients for the corresponding spatial harmonic components that are produced by the two winding designs.

(a) (b) (c)

Figure 4.33: MMFs and spatial harmonic spectrum using full-pitch distributed winding type for five-phase stator design (a) an MMF per unit current of the fundamental spatial harmonic (b) an MMF per unit current of the third spatial harmonic (c) spatial harmonic spectrum

Figures 4.33 and 4.34 show the total MMF waveforms per unit current for the five-phase stator design and their spatial harmonic spectrum based upon both winding designs. The distributed winding design produces a more sinusoidal MMF waveform than the concentrated winding design, therefore this winding type results in a larger first winding coefficient and a smaller third winding coefficient than the concentrated winding design. By contrast, the magnitude of an MMF produced by the concentrated winding design results in a different harmonic spectrum when compared to the distributed winding due to a short winding pitch. While the first winding coefficient of the concentrated winding design is reduced, the third winding coefficient becomes higher than the distributed winding design.

Using the Fourier series expansion technique, the winding coefficients of the MMF waveforms based on the distributed and concentrated winding designs can be found in Table 4.1. The winding coefficients are directly correlated to the magnitudes of the spatial harmonic component in the

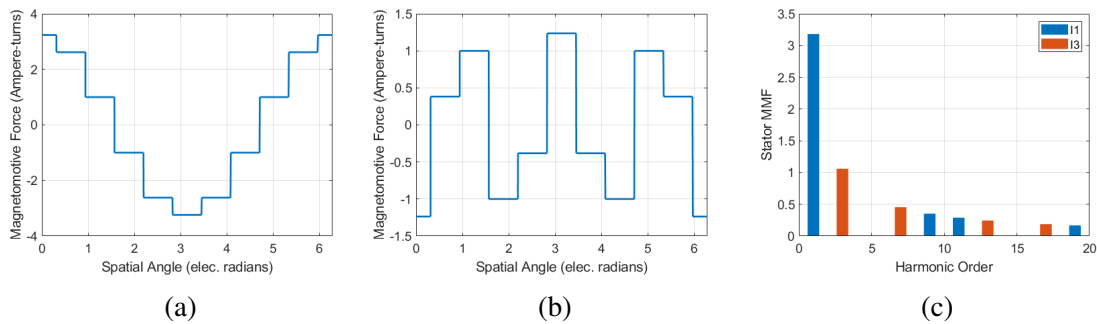(a)   (b)   (c)
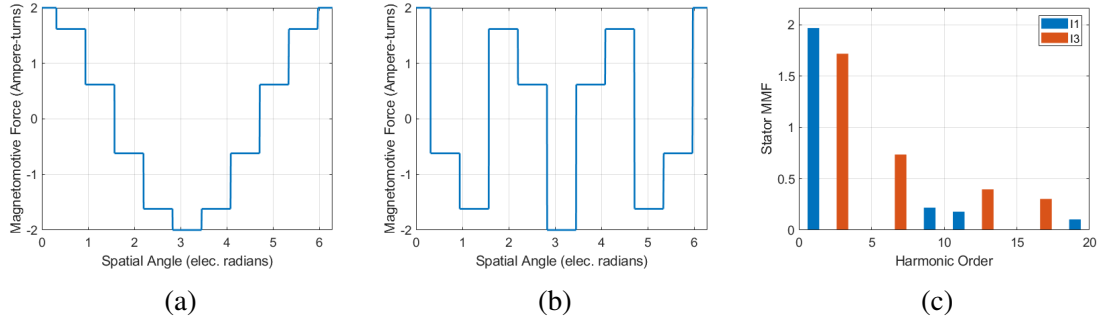
Figure 4.34: MMFs and spatial harmonic spectrum using concentrated winding type for five-phase stator design (a) an MMF per unit current of the fundamental spatial harmonic (b) an MMF per unit current of the third spatial harmonic (c) spatial harmonic spectrum

resulting MMF. Note that the fifth order winding coefficient k_5 is neglected as this term is canceled when the five-phase windings are in star-connected configuration.

Winding Design	k_1	k_3	k_7	k_9	k_{11}	k_{13}	$\sum k_{1,3}$	$\sum k_{7-13}$
Distributed winding	0.637	0.212	0.091	0.071	0.058	0.049	0.849	0.269
Concentrated winding	0.394	0.343	0.147	0.044	0.036	0.079	0.737	0.306

Table 4.1: Winding coefficients of full-pitch distributed winding and concentrated winding for a five-phase stator design

For the proposed harmonic excitation scheme, it is desired that the winding coefficients for the main spatial harmonic components are large and the winding coefficients for the others are small. Inspection of Table 4.1 reveals that the full-pitch distributed winding designs have higher first and third winding coefficients combined than the concentrated winding design, which is beneficial for the proposed excitation scheme. Moreover, the sum of the high-order winding coefficients for the distributed winding design is slightly smaller than that for the concentrated winding design, therefore the effects of the undesired harmonic couplings with the distributed winding design are smaller.

Despite the advantage of the distributed winding design in the winding coefficients, the concentrated winding design can be a useful choice when smaller winding resistance and simpler manufacturability are important design factors. The concentrated winding type generally has a

higher slot filling factor and a shorter length of end-turns of winding which decreases its winding resistance and conduction loss when compared to the distributed winding type. Since the concentrated winding design has a short pole pitch requiring less space for the machine, this winding design has more flexibility in the rotor design where both the transformer and field windings need to be placed. The concentrated winding type also has simpler manufacturability due to the short end-turns. Conversely, the manufacturing cost for the distributed winding type is generally higher than the concentrated winding design.

4.7 Design Procedure for Maximum Torque Capability

The design procedure of the proposed machine design is presented in Figure 4.35 which focuses on the key machine parameters, such as the number of turns for all windings, the ratio of stator currents, and thickness and size of the stator and rotor cores. The objective for this design procedure is to maximize the induced voltage in the transformer winding and DC current in the field winding, therefore reaching the highest peak torque capability of the proposed machine.

There are three major steps in this design procedure. The stator core is first designed based upon the numbers of phases and poles of the stator windings. Then, the number of turns of the stator winding is determined based upon the predetermined voltage constraint from a target specification. The stator winding is excited using the maximum current density (J_{max}). If magnetic saturation is observed in the FEA simulation, the design of the stator core is adjusted such as the width of stator tooth and the thickness of stator back-iron.

Once the design of the stator core is set, the rotor core is next designed based upon the numbers of phases and poles of the transformer and field windings. In order to maximize the induced voltage in the transformer winding, the turns ratio between the transformer windings and the field windings is investigated using a parametric sweep in FEA simulation. Similarly, the design of the rotor core is adjusted if saturation is observed. With proper rotor turns ratio, both the induced transformer voltage and DC field current are maximized.

In the last step, the stator current ratio between the fundamental spatial harmonic current and the third or other additional spatial harmonic current is determined to maximize electromagnetic torque of the proposed machine design under J_{max}.
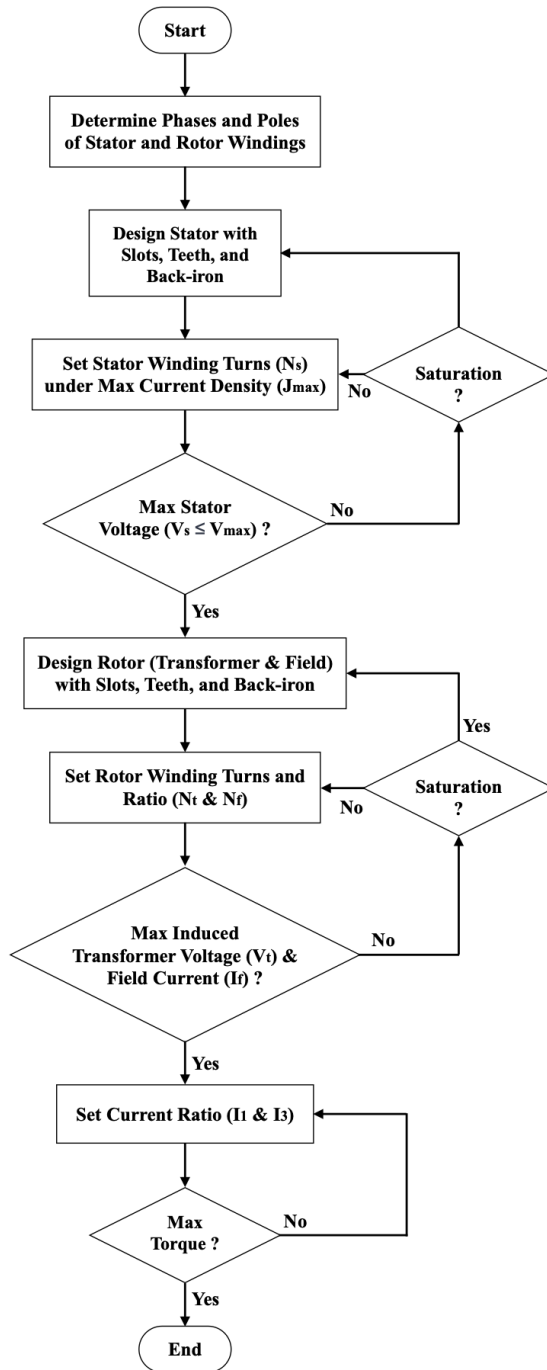
Figure 4.35: Design procedure of stator, transformer, and field windings and machine cores

CHAPTER 5

Proposed Machine Designs and Operating Principle

This chapter presents two design approaches and implementations of the brushless, self-excited synchronous field-winding machine that uses the multiple spatial harmonic excitation scheme. Both machine designs are created based upon a five-phase AC stator design using a full-pitch distributed winding layout since this particular five-phase design is beneficial in producing a larger second spatial harmonic or third spatial harmonic under certain current density constraints than the six-phase design with the fifth spatial harmonic.

5.1 Machine Design 1: Five-phase Machine with Single-phase Transformer Winding

The machine design 1 shown in Fig. 5.1 has a five-phase AC stator with a ten-pole design, a single-phase transformer winding with a thirty-pole design, and field windings with a ten-pole design.

The stator has fifty slots for the five-phase winding and is wound using a full-pitch distributed winding design. The rotor has a salient pole design, and both the single-phase transformer winding and the field winding are wound in a concentrated winding arrangement on the rotor. The rotor consists of separate magnetic cores for the transformer winding and a main core for the field winding. The cores for the transformer winding are located between the main core teeth. Each transformer winding is wound around the back-iron portion of the transformer core instead of its
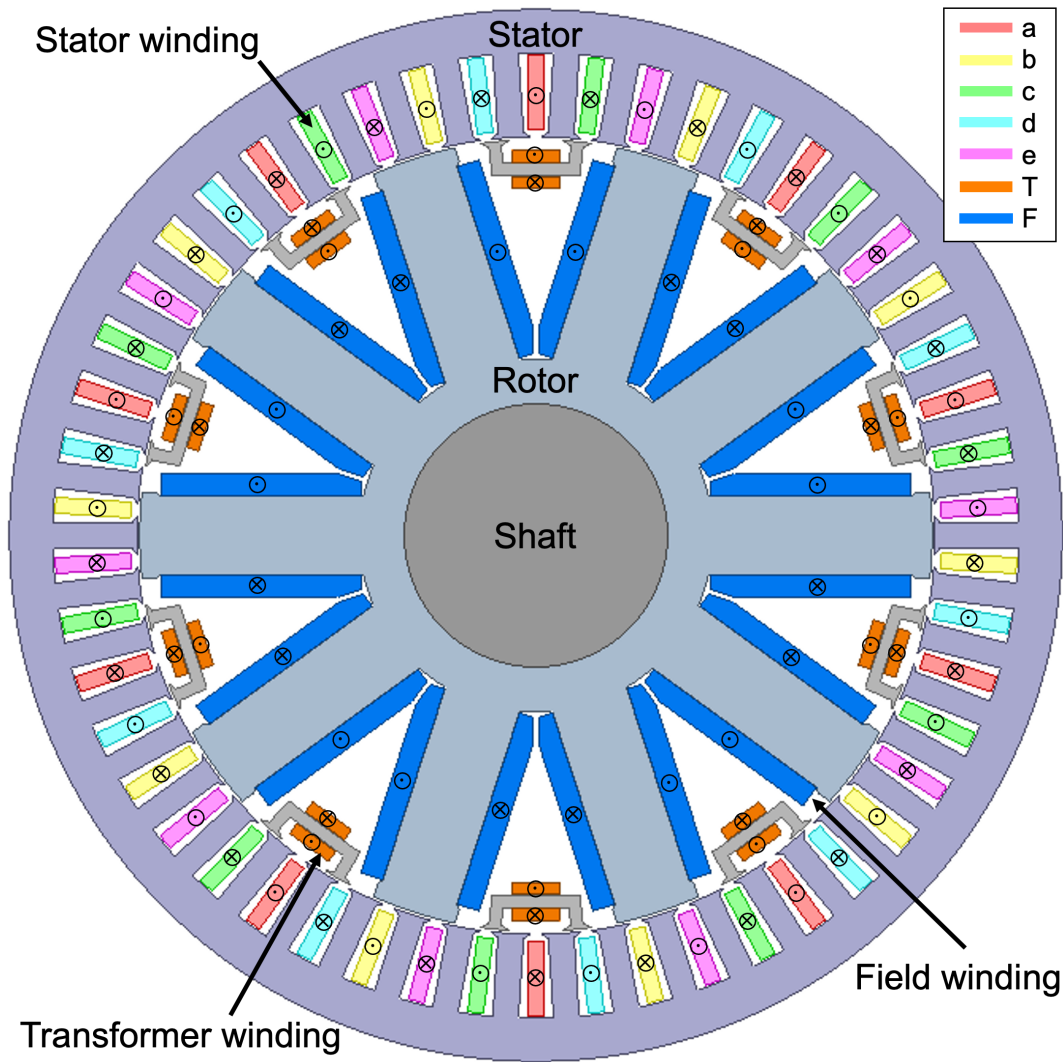
Figure 5.1: Five-phase design of the proposed machine topology (rectifier not shown). a, b, c, d, e—Stator windings, T—Rotor transformer windings, F—Rotor field windings

teeth region in order to maximize the space utilization of the rotor slot area. Hence, each transformer winding is oriented horizontally along with the back-iron of the transformer core whereas the field winding is in a vertical position.

Figure 5.2 shows a schematic diagram of the proposed machine design 1. The machine is designed so that the stator MMF wave at the third spatial harmonic couples with the transformer winding and the stator MMF wave at the fundamental spatial harmonic couples with the field winding and rotates in synchronism with the rotor. The width of the transformer cores is designed so that the stator MMF at the third spatial harmonic can enter from one side of the transformer core
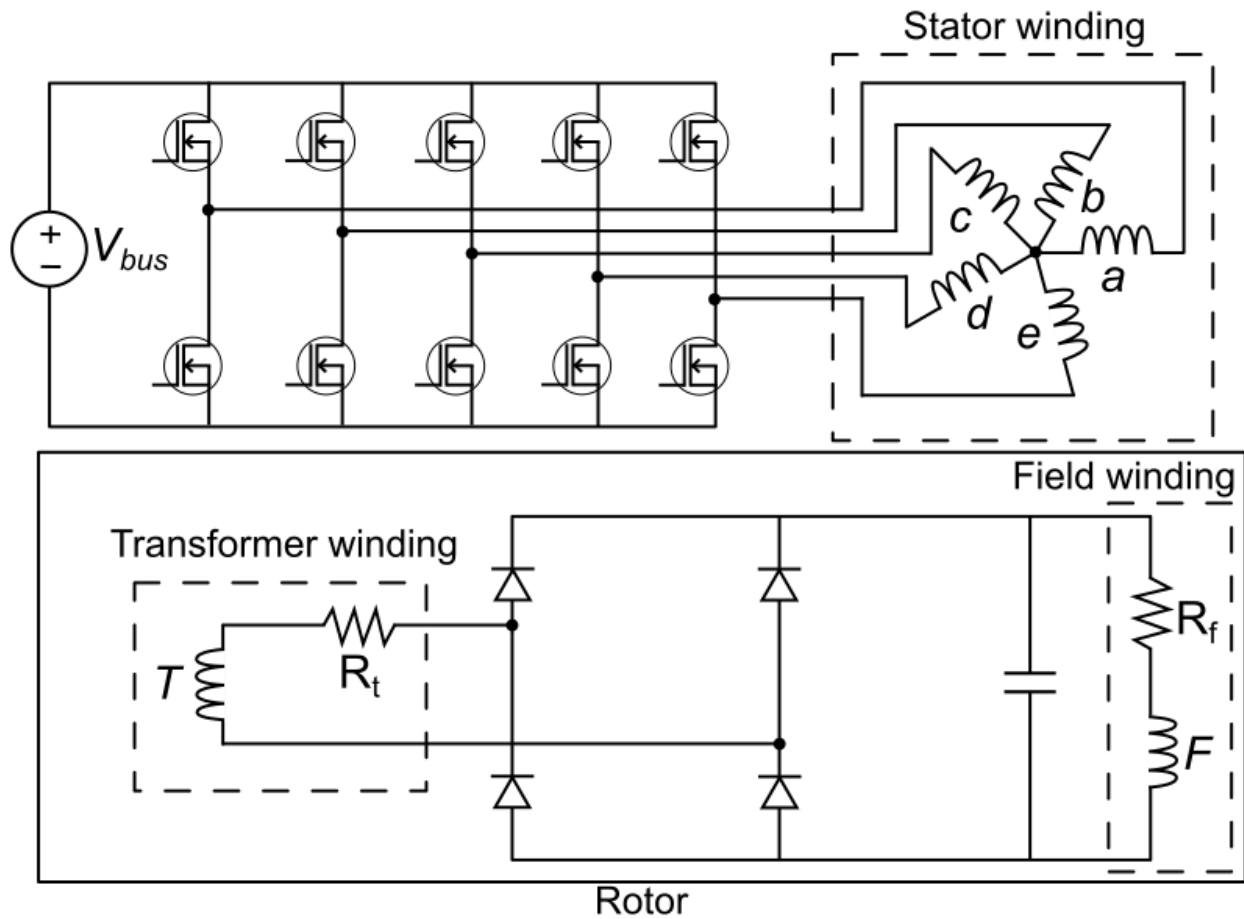
Figure 5.2: Schematic diagram of the machine design with single-phase transformer winding.

and exit to another side creating harmonic couplings between the stator and transformer windings. The third spatial harmonic MMF rotates at a different velocity than the transformer winding, so the transformer winding "sees" an AC magnetic field, which induces an EMF in the winding. This induced EMF becomes a power source to produce a DC current in the field winding through the use of a diode rectifier. This DC current generates a DC rotor field, which interacts with the fundamental spatial harmonic stator magnetic field and produces torque.

The concentrated winding design used for the transformer and field winding results in relatively small winding resistances due to a shorter end-turn length compared to the distributed winding design. This results in low conduction losses and low temperatures in the rotor during motor operations which are beneficial to the cooling aspect of the rotor cores, which is a typical issue when compared to the cooling of the stator core.

Moreover, the transformer cores are physically separated from the field-pole rotor to maximize the decoupling of the two magnetic fluxes between the transformer cores and the field-pole rotor cores.

5.1.1   Spatial Harmonic Spectrum for Machine Design 1

The spatial harmonic spectrum of all windings for machine design 1 is presented in Figure 5.3, which is generated using the MATLAB and Simulink simulation tools neglecting the slotting effects. Two excitation modes for the stator windings produce two different sets of the spatial harmonic spectrum. The first set of the spatial harmonic in the stator MMFs contains the fundamental or 1st spatial harmonic as the main harmonic component produced by the fundamental spatial harmonic currents. The second spatial harmonic set in the stator MMFs contains a third spatial harmonic as the main harmonic component produced by the third spatial harmonic currents.

The spatial harmonic spectrums of the rotor MMFs from the transformer winding and the field winding are generated based on their resulting currents. The set of spatial harmonics in the MMF of the field winding is produced by a DC field current, as a result of the diode rectifier, and couples with the stator MMF at the fundamental spatial harmonic. On the other hand, the set of

spatial harmonics in the MMF of the transformer winding is produced by an induced AC sinusoidal voltage and current and couples with the stator MMF at the third spatial harmonic.
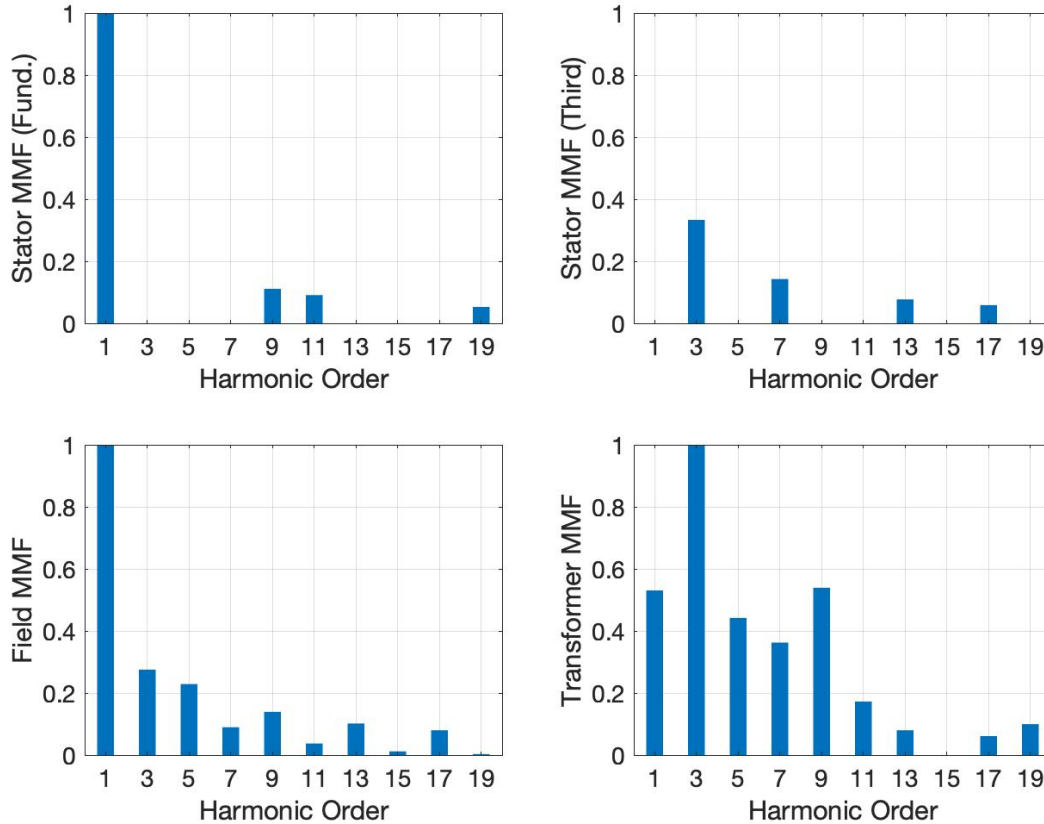

Figure 5.3: Harmonic spectrum of all windings for a five-phase machine with a single-phase transformer winding

In addition to the interactions between the main spatial harmonic components, there are additional harmonic couplings at high harmonic orders or sub-harmonic components. For example, the stator MMF produced by the third spatial harmonic currents also produces 7th, 13th, and 17th spatial harmonics which also induce voltages in the transformer winding and generate the DC field current. Inspection of the harmonic spectrum of all windings reveals that there is a relatively large harmonic coupling at these high harmonic orders between the stator MMF produced by the fundamental spatial harmonic currents and transformer MMF, which is undesirable in terms of a decoupling between the excitation of the two rotor windings. These undesired harmonic couplings

affect certain amounts of a DC field current even with the fundamental spatial harmonic currents, therefore reducing the independency of the rotor field controls. In particular, this brings a potential issue during operations at high speeds where the rotor field needs to be reduced in order to maintain a constant power while operating under the voltage constraint.

5.1.2   Separation of Magnetic Fluxes in Rotor for Machine Design 1

The rotor design of machine design 1 achieves a high degree of separation of the magnetic fluxes for the transformer winding and the field winding. When the machine is excited with the third spatial harmonic currents to couple with the transformer winding, the stator flux due to the third spatial harmonic creates a flux path in each transformer core with minimal impacts in the main rotor core for the field winding as shown in Figure 5.4. On the other hand, when the machine is excited with the fundamental spatial harmonic currents to couple with the field winding, the stator flux due to the fundamental spatial harmonic creates a flux path in the main field-pole rotor core as shown in Figure 5.5.

Furthermore, the separate rotor core design allows the optimization of each core design independently which simplifies the optimization process. When high saturation of the flux density in the transformer cores causes an issue for inducing voltages in the transformer winding, the size of the transformer cores can be increased without changing the geometric dimensions of the field-pole rotor.

Using this design approach, this machine design can achieve relatively high core utilization and have a high peak torque capability when the stator flux due to the fundamental spatial harmonic quadrature currents combines with the stator flux due to the third spatial harmonic currents and the field winding flux to produce torque. Subsequently, the high core utilization results in reduced high saturation in local regions, such as the stator and rotor teeth, which is beneficial to the excitation of the transformer winding using the third spatial harmonic component. Moreover, as the core losses are proportional to the rotating frequency of the machine, using the fundamental spatial harmonic currents for synchronizing with the rotating frequency results in significantly lower core losses at
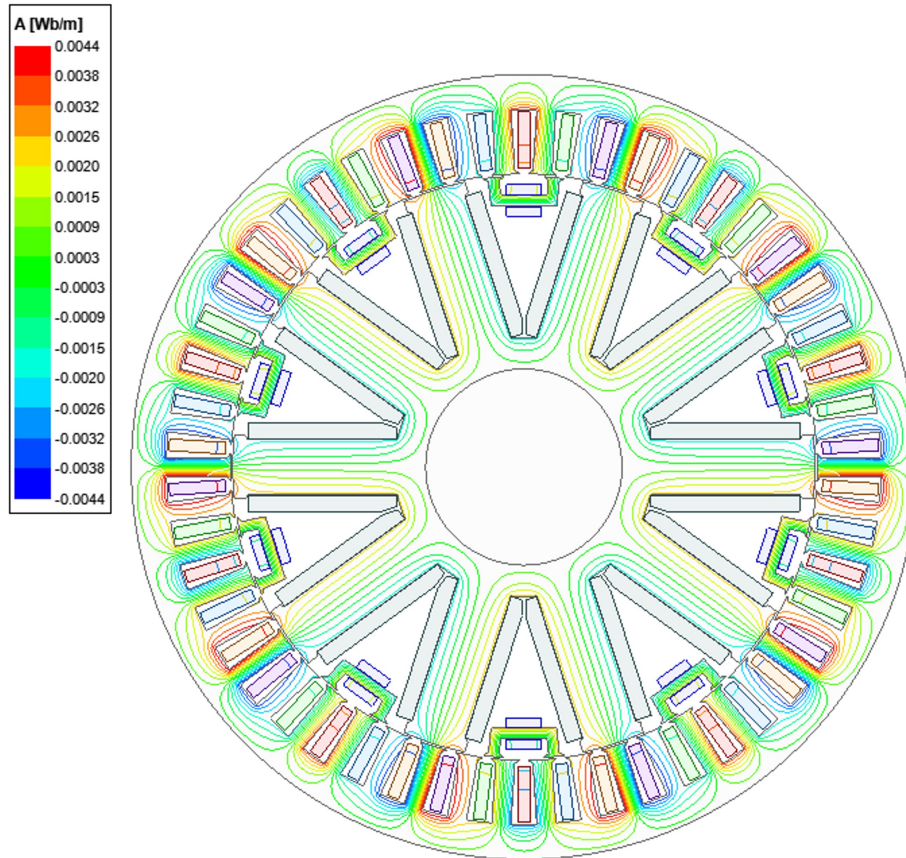
114

Figure 5.4: Flux lines generated by third harmonic currents

high speeds compared to the machine design using the third spatial harmonic component coupling with the field winding.

However, limitations of such rotor design are the difficulty of fixing the separate transformer cores to the rotor structure, not having a multi-phase transformer winding design, and significant amounts of extra spatial harmonic contents generated by the concentrated winding design. Because the limited spaces are available for the transformer cores, the multi-phase transformer winding design is physically infeasible while not interfered with by the other fluxes. Several attempts were made to achieve the multi-phase transformer design by shifting some of the transformer cores, but the resulting transformer EMFs were significantly interfered with and became unbalanced. The issue with the single-phase transformer design is the fact that the power transfer from the induced
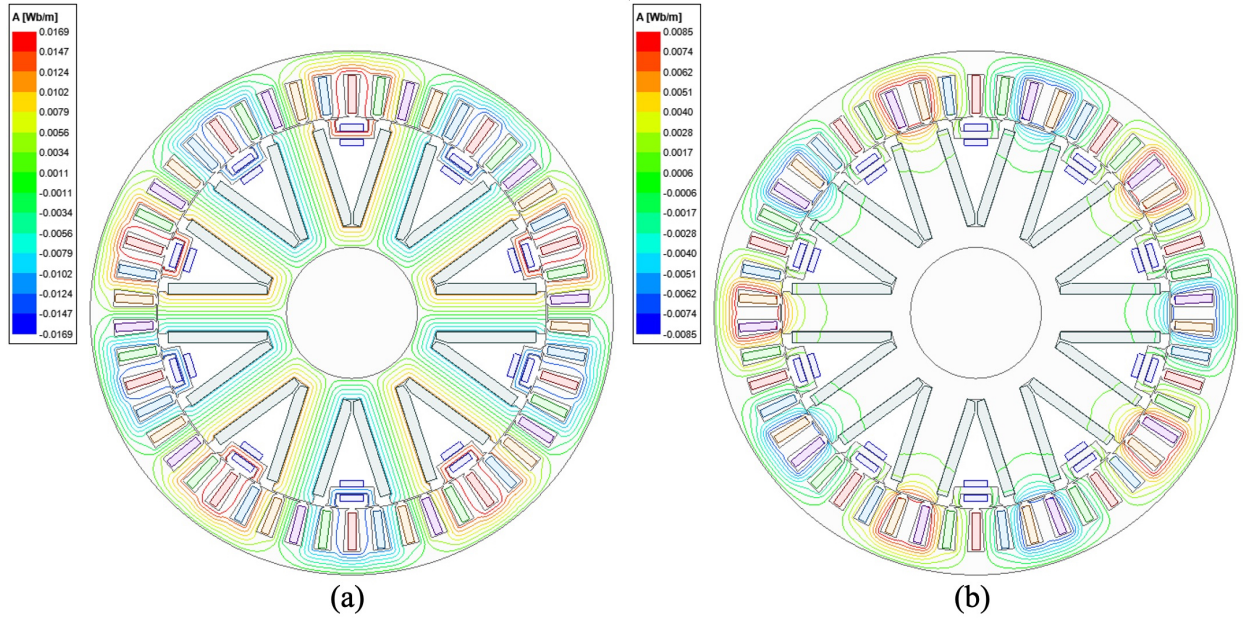
Figure 5.5: Flux lines generated by: (a) Direct-axis fundamental current, (b) Quadrature-axis fundamental current

voltage and current in the transformer winding results in a sinusoidal waveform and large torque ripple. Moreover, the additional spatial harmonic contents generated by the concentrated winding design increase the torque ripple.

5.1.3 Target Specification for Machine Design 1

The first machine design is tested for liquid cooling applications and built using the machine specification based upon a commercially available EM-80 motor from Magna, as shown in Table 5.1.

Table 5.1: Machine design 1 specification for liquid cooling applications

Parameters	Value
Stator outer diameter (mm)	220
Rotor outer diameter (mm)	165.6
Shaft outer diameter (mm)	55
Core length (mm)	100
Air-gap length (mm)	0.6
Turns per phase - Stator winding	7
Turns per phase - Rotor transformer winding	21
Turns per phase - Rotor field winding	250
Number of poles - Stator winding	10
Number of poles - Rotor transformer winding	30
Number of poles - Rotor field winding	10
Phase numbers - Stator winding	5
Phase numbers - Transformer winding	1
Slot numbers - Stator	50
Slot numbers - Rotor	10
Slot packing factor	0.5
Rated (base) speed (RPM)	2779
Maximum speed (RPM)	9094
DC bus voltage (VDC)	325
Maximum line-to-line voltage (V_{rms})	200
Maximum phase current (A_{rms})	390
Maximum current density per slot (A_{rms}/mm^2)	30
Winding temperature (°C)	120
Type of Iron	M350-50A
Type of Cooling	Liquid-cooled

5.2 Machine Design 2: Five-phase Machine with Three-phase Transformer Winding

The machine design 2 shown in Figure 5.6 has a five-phase AC stator with a ten-pole design, three-phase transformer windings with a ten-pole design, and field windings with a thirty-pole design. The three-phase transformer design allows the power transferred to the transformer winding to be roughly constant in steady-state, and hence reduce power oscillations and torque ripple in the machine, as opposed to a single-phase transformer design. The pole numbers of each rotor winding are selected to achieve the desired harmonic coupling with the rotating MMFs and a feasible rotor design.

The stator of the machine design has fifty slots for the five-phase winding and is wound using a full-pitch distributed winding design. The rotor has a non-salient pole design, and the three-phase transformer windings are wound in a distributed winding arrangement while the field windings adopt a concentrated winding arrangement in thirty slots on the rotor. The resulting rotor windings have a multi-layer winding arrangement where the field windings are placed in the inner layer of the slot and the transformer windings are placed in the outer layers of the slot in order to minimize leakage inductance in the transformer windings.

Figure 5.7 shows a schematic diagram of the proposed machine topology. The machine is designed so that the stator MMF wave at the fundamental spatial harmonic couples with the transformer windings and the stator MMF wave at the third spatial harmonic couples with the field winding and rotates in synchronism with the rotor. The fundamental harmonic MMF rotates at a different velocity than the transformer winding, so the transformer winding "sees" an AC magnetic field, which induces an EMF in the winding. This induced EMF becomes a power source to produce a DC current in the field winding through the use of a diode rectifier. This DC current generates a DC rotor field, which interacts with the third harmonic stator magnetic field and produces torque.

One advantage of the proposed design is that the five-phase stator can produce field current at
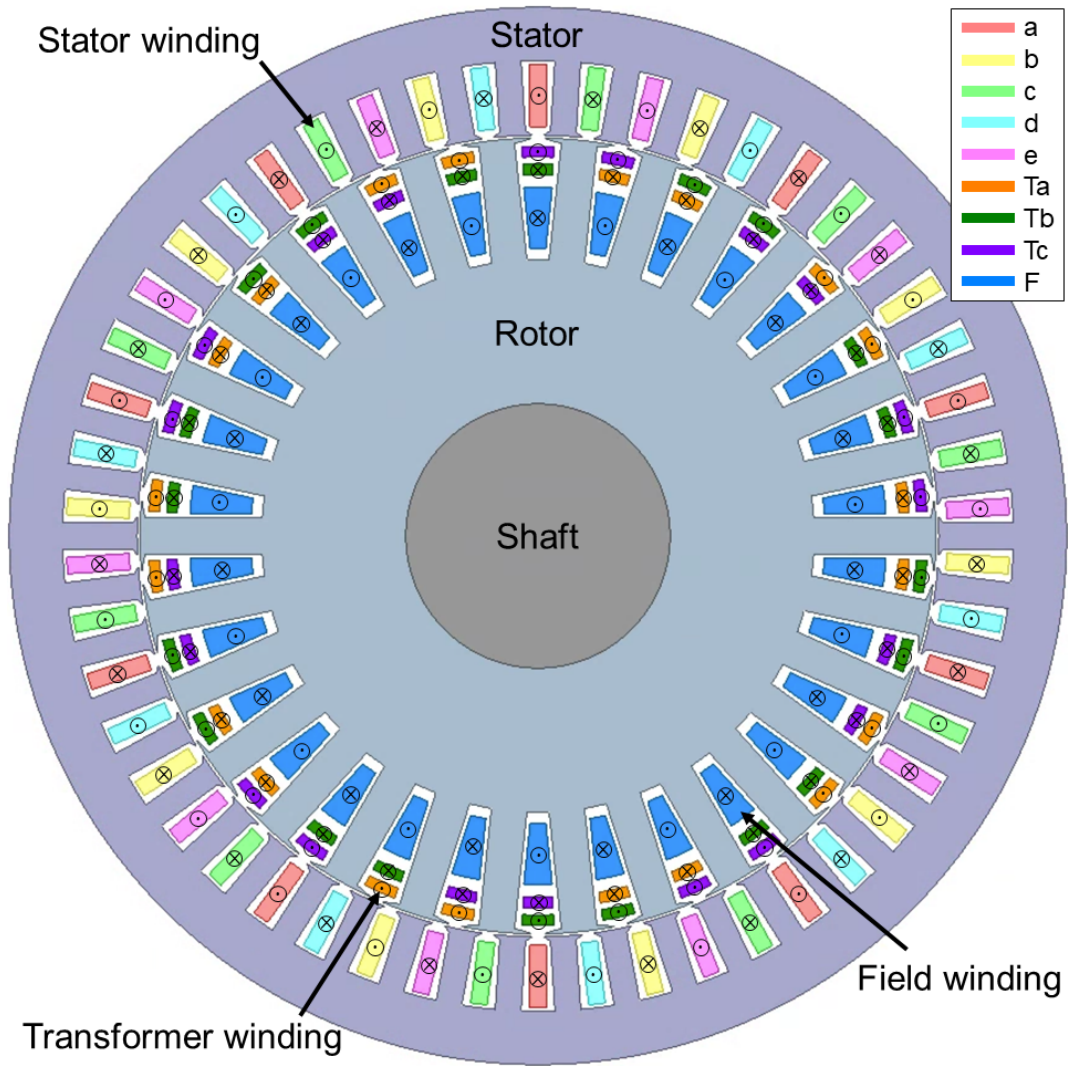
Figure 5.6: Five-phase design of the proposed machine topology (rectifier not shown). a, b, c, d, e—Stator windings, Ta, Tb, Tc—Rotor transformer windings, F—Rotor field windings
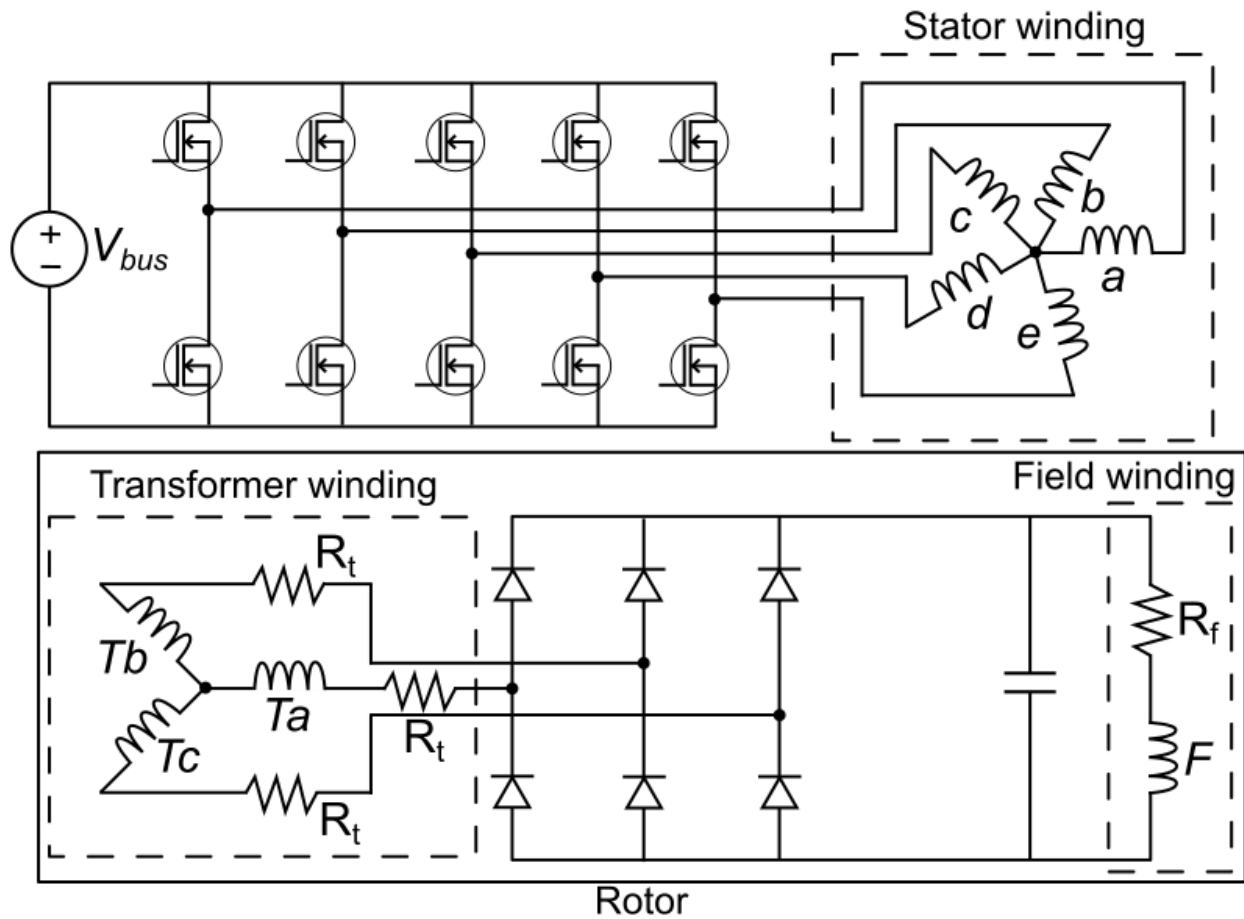
Figure 5.7: Schematic diagram of the machine design with three-phase transformer winding.

any speed by adjusting the rotating frequency of the fundamental spatial harmonic. The ability to adjust the frequency of the transformer winding excitation creates a degree of freedom that can be exploited to maximize power or efficiency while staying within the voltage and current constraints imposed by the inverter. At low-speed regions, the frequency of the fundamental harmonic can be increased to induce the required transformer EMF. Since the back-EMF produced by the field winding is small at low speeds, it is possible to increase the frequency of the fundamental stator field and stay within the voltage constraints of the inverter. For high-speed operation, the frequency of the fundamental spatial harmonic currents can be set to DC and still generate the field current due to the angular velocity of the rotor. The use of the DC currents causes the stator voltage component due to the fundamental spatial harmonic to consist of only a resistive drop, which minimizes its impact on the voltage.

5.2.1   Spatial Harmonic Spectrum for Machine Design 2

The spatial harmonic spectrum of all windings for machine design 2 is presented in Figure 5.8, which is generated using the MATLAB and Simulink simulation tools neglecting the slotting effects. Two excitation modes for the stator windings produce two different sets of the spatial harmonic spectrum. The first set of the spatial harmonic in the stator MMFs contains the fundamental or 1st spatial harmonic as the main harmonic component produced by the fundamental spatial harmonic currents. The second spatial harmonic set in the stator MMFs contains a third spatial harmonic as the main harmonic component produced by the third spatial harmonic currents.

The spatial harmonic spectrums of the rotor MMFs from the transformer winding and the field winding are generated based on their resulting currents. The set of spatial harmonics in the MMF of the field winding is produced by a DC field current, as a result of the diode rectifier, and couples with the stator MMF at the third spatial harmonic. On the other hand, the set of spatial harmonics in the MMF of the transformer winding is produced by induced three-phase AC sinusoidal voltages and currents and couples with the stator MMF at the fundamental spatial harmonic.

In addition to the interactions between the main spatial harmonic components, there are ad-
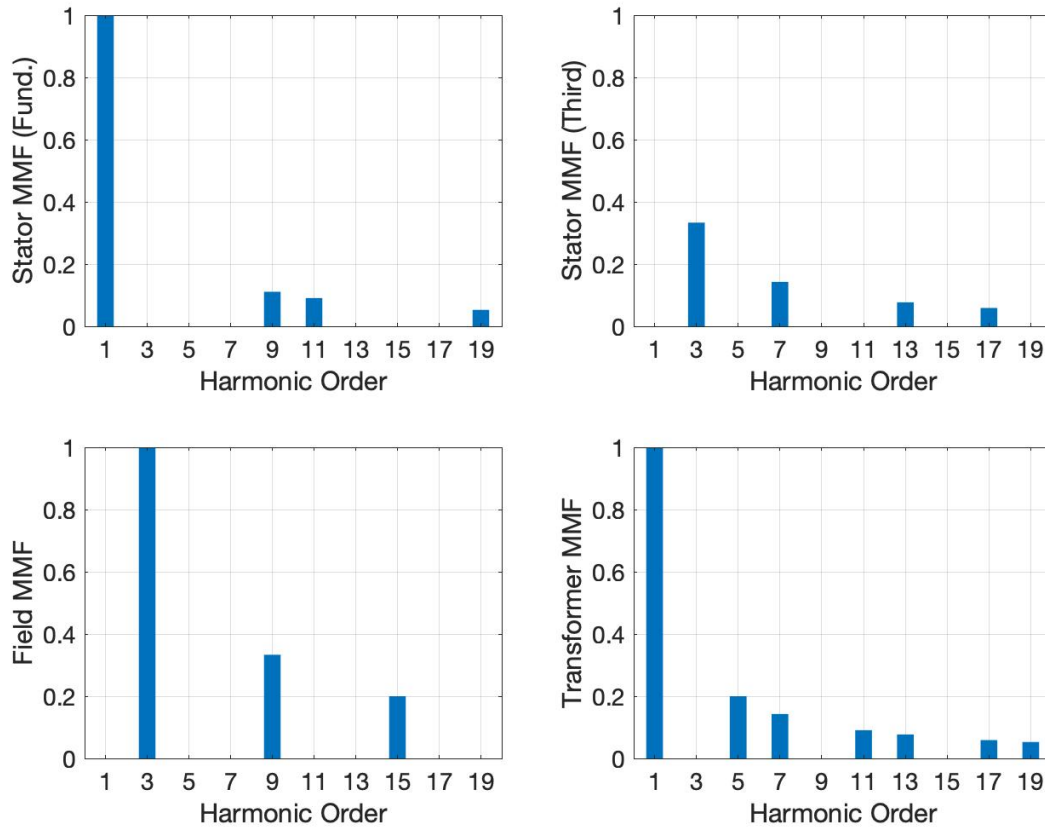
Figure 5.8: Harmonic spectrum of all windings for a five-phase machine with three-phase transformer windings

ditional harmonic couplings at high harmonic orders or sub-harmonic components. For example, the stator MMF produced by the fundamental spatial harmonic currents also produces 11th and 19th spatial harmonics which also induce voltages in the transformer winding and generate the DC field current. Note that the 9th spatial harmonic is not common harmonic between the fundamental stator MMF and the transformer MMF, therefore not contributing to the transformer voltages. Inspection of the harmonic spectrum of all windings reveals that the influence of the couplings between these extra harmonics is significantly smaller than in the case of the first machine design, therefore increasing the independency of the rotor field controls. Moreover, the cancellations of the third harmonic sequence (i.e., 3rd, 9th, 15th, $\cdots$) in the wye-connected three-phase transformer windings further eliminate harmonic interferences among the stator, transformer, and field MMFs.

5.2.2 Initial Approach with Single-layer Rotor Winding Structure for Machine Design 2

The proposed machine topology requires a rotor structure that includes both transformer windings and field winding. In particular, the transformer windings must have a phase angle shift of 120° between each phase to have a three-phase structure and the same number of poles as the stator winding in order to create a desired harmonic coupling at the fundamental spatial harmonic produced by the stator winding. On the other hand, the rotor field winding must have the number of poles that are three times that of the stator winding in order to couple at the third spatial harmonic and synchronize with the rotating speed.

Early rotor, shown in Figure 5.9, is achieved using the distributed winding design for both rotor windings with a single-layer structure making a total of sixty slots for the ten-pole machine. The transformer windings are made in a three-phase winding configuration and coupled at the fundamental spatial harmonic with the stator windings. The field winding is structured in a thirty-pole configuration to couple at the third spatial harmonic with the stator windings.

A key benefit of the three-phase transformer winding structure is that the net power transfer by the induced transformer voltage and current becomes constant which results in low torque ripple. The balanced three-phase transformer winding structure also removes all third spatial harmonic sequences (i.e., 3rd, 9th, 15th, 21st, $\cdots$) in the transformer MMF via wye connection, therefore eliminating undesired harmonic couplings with the third spatial harmonic by the stator MMFs and the field winding MMFs. Moreover, this improves the decoupling of the field current produced by the fundamental and third spatial harmonic currents, hence the field current produced by the third spatial harmonic currents is significantly reduced.

However, the rotor using the single-layer winding structure shows a limitation when generating the field current and torque due to the magnetic saturation of the machine cores. Figure 5.10 shows that the magnetic flux distributions produced by both fundamental and third harmonic currents are highly concentrated at both the stator and rotor teeth region as well as the back-iron region of the stator core. Moreover, corresponding flux paths share a majority of those teeth and back-
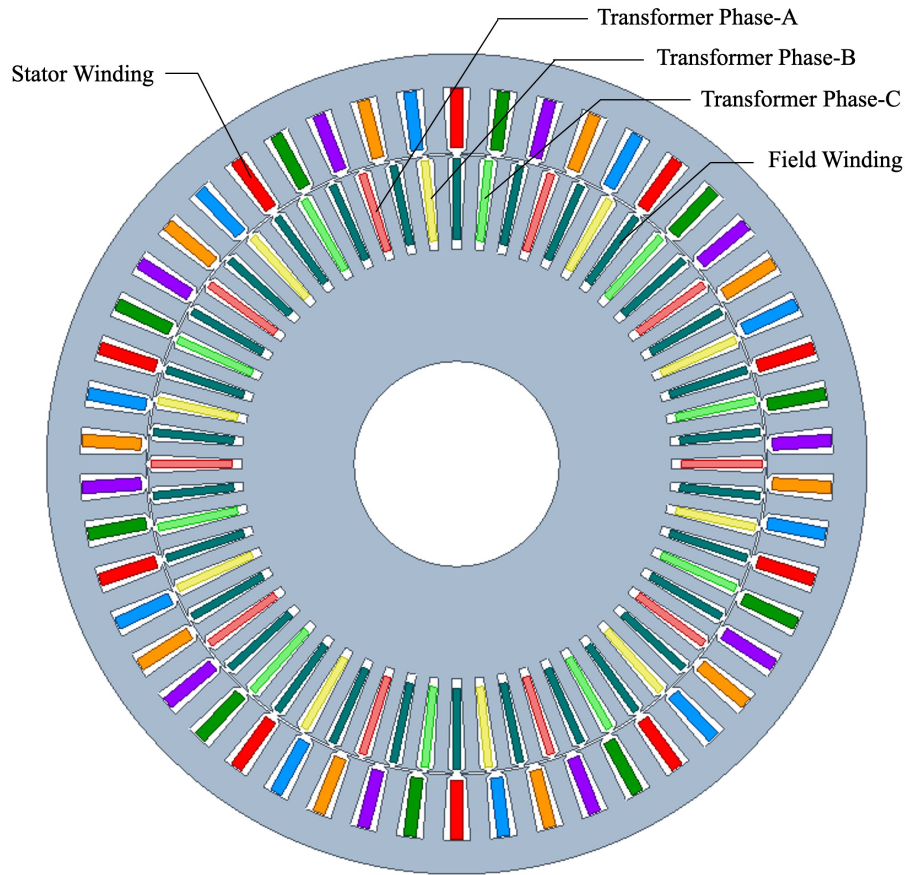
Figure 5.9: Initial approach using single-layer rotor winding structure

iron regions, resulting in saturation in those regions when both magnetic fluxes are superimposed during the operation of the proposed machine. Saturation of both teeth and the stator back-iron regions limit the excitation of the transformer windings, the field current production, and the torque capability of the machine. Figure 5.11 shows that the magnetic saturation of the teeth regions and the stator back-iron occurs more prominently with the fundamental stator fluxes which are responsible for exciting the transformer windings.

Additionally, the rotor windings using the distributed winding design increase conduction losses when compared to the concentrated winding design because of increased winding resistances of both the transformer and field windings. The single-layer rotor structure essentially results in a high number of slots in the rotor to include both the three-phase transformer windings
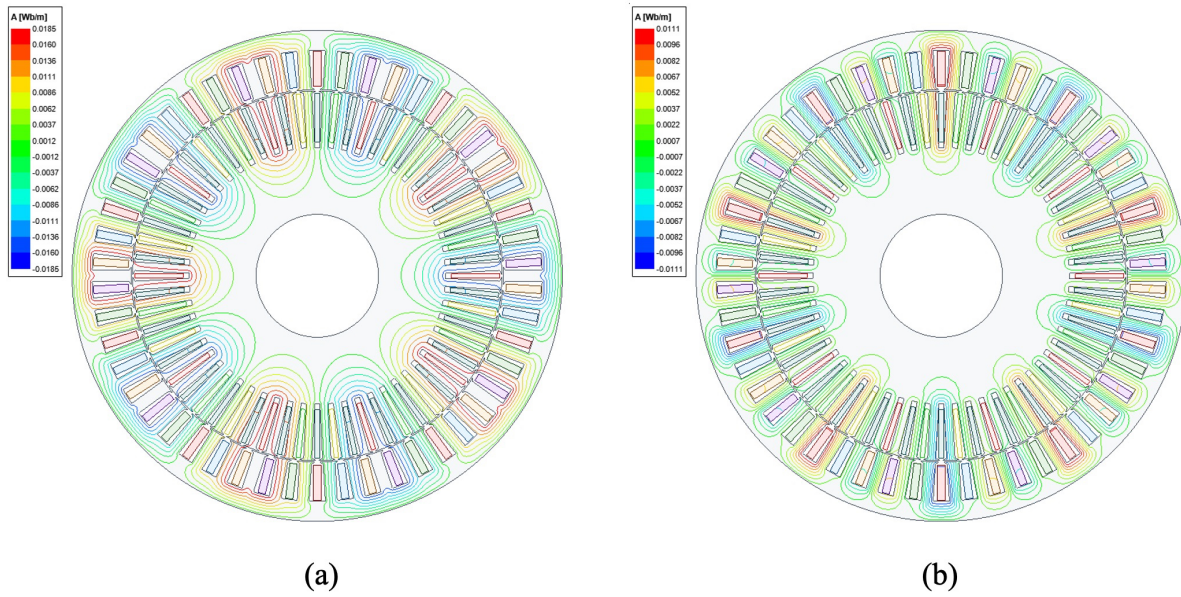
Figure 5.10: Flux line generated by (a) Fundamental spatial harmonic currents, (b) Third spatial harmonic currents
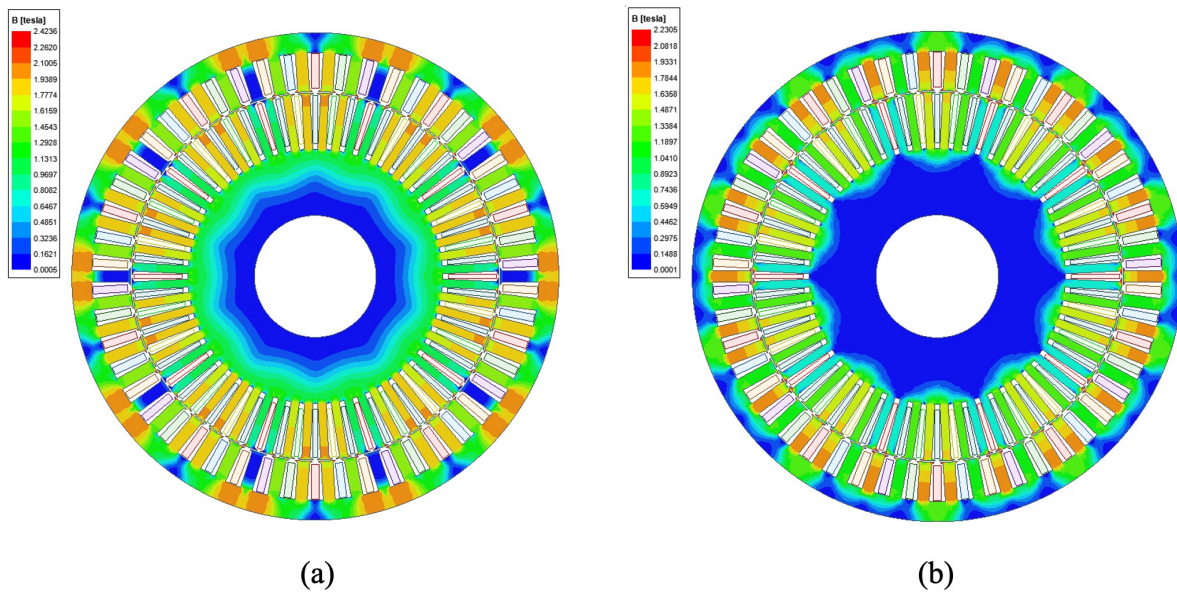

Figure 5.11: Flux density generated by (a) Fundamental spatial harmonic currents, (b) Third spatial harmonic currents

and the field winding, therefore reducing the windable slot area per copper. The resulting small slot area in the rotor makes the size of a copper thin and increases overall resistances. Furthermore,

the distributed winding design generally results in a long end-turn length per pole which makes the winding resistance large. One calculation of the phase resistance of the field winding with a certain number of turns per slot shows that the resistance of a field winding using the distributed winding design is almost five times greater than the resistance of a field winding using the concentrated winding design for the same outer diameter and axial length of the rotor.

5.2.3 Improved Approach with Multi-layer Rotor Winding Structure for Machine Design 2

The early approach with the single-layer rotor winding structure shows saturation in the stator and rotor irons which limits the performance of the machine. To improve the saturation issue, the machine is modified to have a multi-layer rotor winding structure. The improved rotor is shown in Figure 5.12, where both the transformer and field windings are arranged in a triple-layer layout. The three-phase transformer windings are wound using the distributed winding design, and the field winding is wound using the concentrated winding design. Specifically, the field winding is placed in the inner layer of the slot, and the transformer windings are placed in the outer layers of the slot in order to minimize leakage inductance in the transformer windings.

By implementing the multi-layer rotor winding structure, the total number of slots in the rotor is halved which effectively doubles the width of the rotor teeth and reduces the flux density in the rotor teeth. Figures 5.13 and 5.14 compare flux densities between the early approach with the single-layer rotor winding and the improved approach with the multi-layer rotor winding with independent spatial harmonic current excitations. The flux densities in the improved approach are significantly reduced in both excitation cases. Figure 5.15 shows the improvements in the field current and torque with the new rotor thanks to the increased width of the rotor teeth, therefore increasing the excitation of the transformer windings and torque.

The machine design 2 brings a number of issues that the machine design 1 does not have. One issue is that the core utilization of this approach is not ideal as the stator MMF at the third spatial harmonic is a dominant component used for producing torque. Because the rotating MMF at the
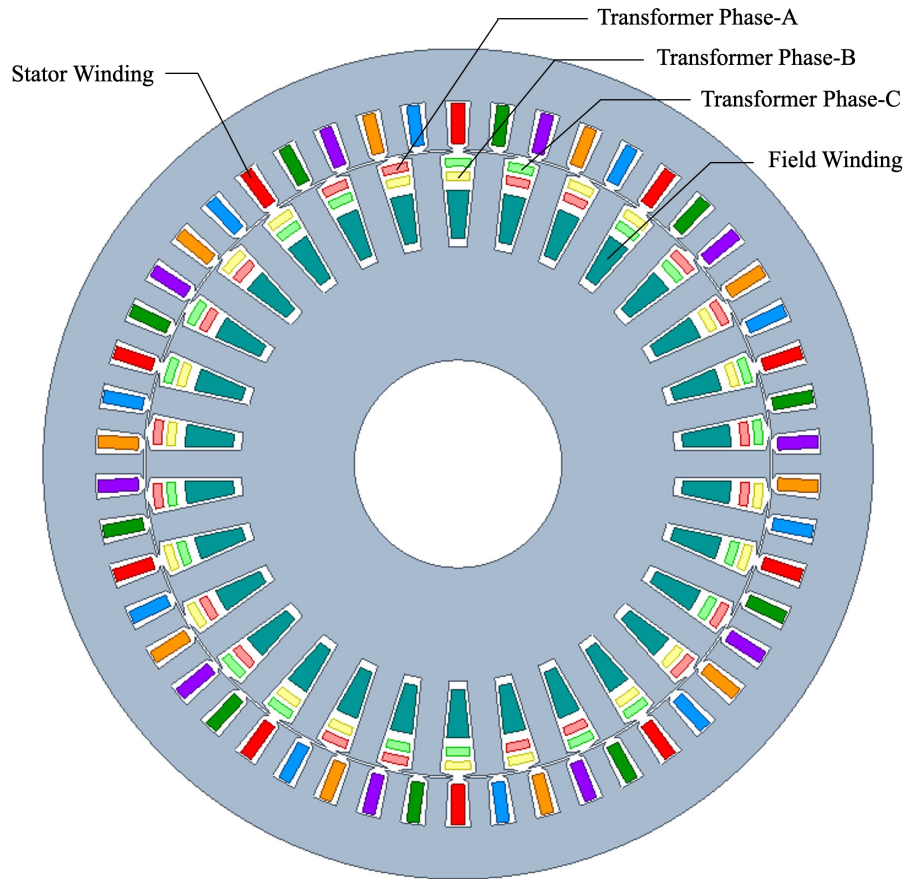
126

Figure 5.12: Improved approach using multi-layer rotor winding structure

third spatial harmonic has a much shorter pulse duration than the MMF at the fundamental spatial harmonic, this results in the majority of the flux densities in the machine cores being concentrated around the stator and rotor tooth regions. The finite element analysis simulations of this machine design show that the back-iron region of the rotor is not as well utilized as the tooth regions and the back-iron of the stator.

The multi-layer rotor winding structure results in both the magnetic fluxes due to the transformer and field windings being shared on the rotor teeth region. This makes the machine teeth regions reach the saturating threshold rather quickly and limits the harmonic couplings between the stator and transformer windings. Figure 5.10 shows how the two magnetic fluxes are imposed on the machine teeth region.

(a)   (b)
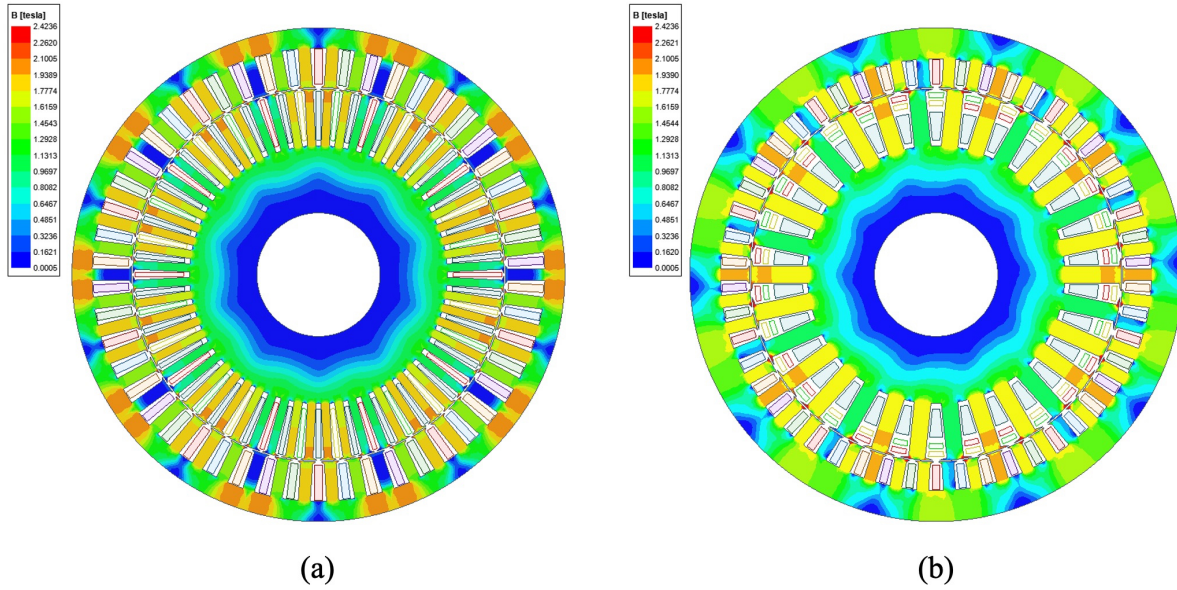
Figure 5.13: Comparison of flux density generated by fundamental spatial harmonic current in (a) Initial rotor, (b) Improved rotor

(a)   (b)
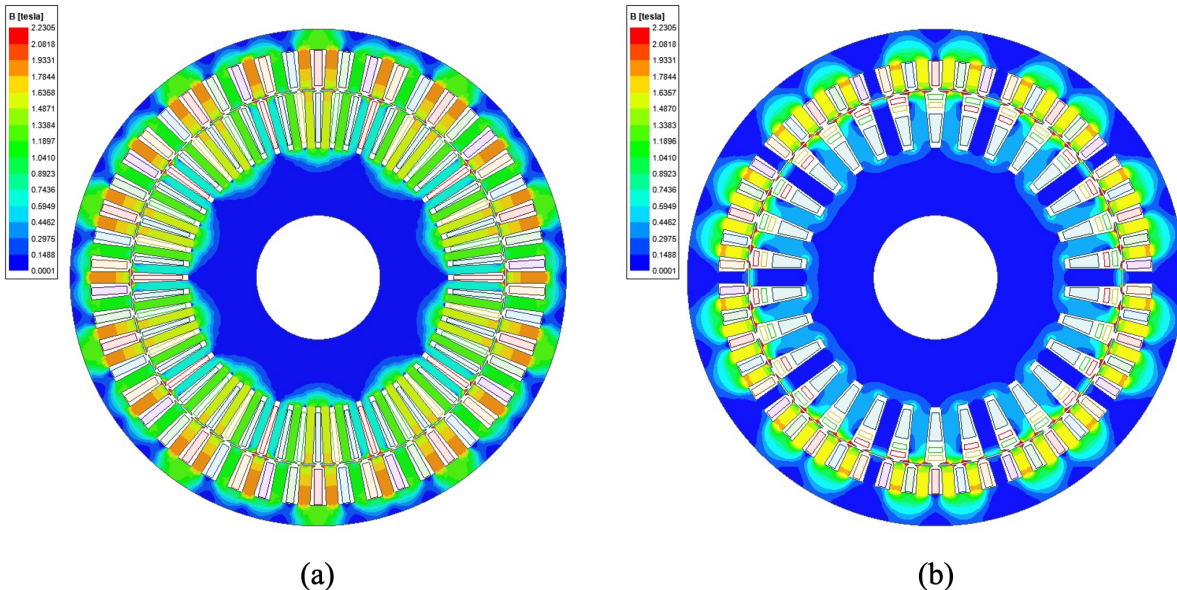
Figure 5.14: Comparison of flux density generated by third spatial harmonic current in (a) Initial rotor, (b) Improved rotor

Lastly, the machine design 2 using the rotating MMF at the third spatial harmonic to synchronize with the rotating frequency results in larger core losses than the machine design 1 as the
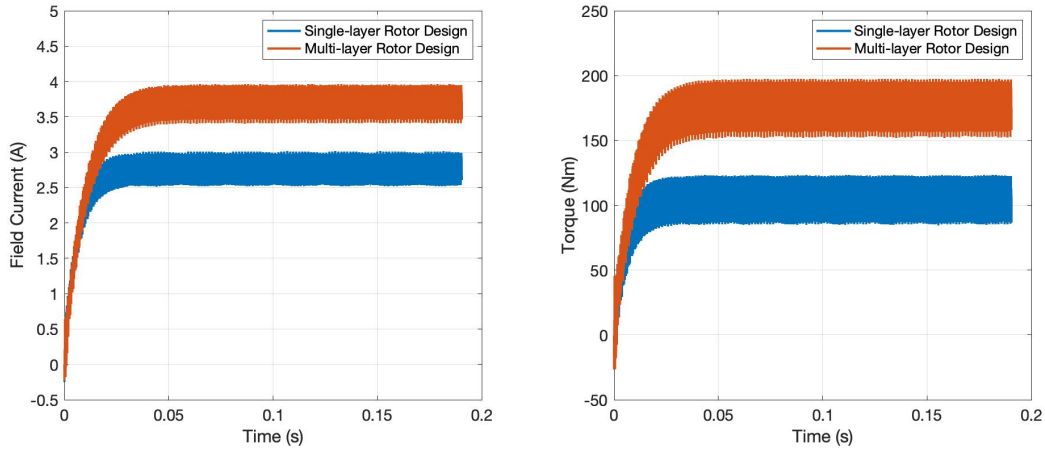
Figure 5.15: Comparison of field current and torque between single-layer rotor and multi-layer rotor using both fundamental and third spatial harmonic currents ($I_1 = 20$ A, $I_3 = 330$ A)

frequency used for the third spatial harmonic currents becomes three times that of the rotating frequency. In general, the core losses of the machine are proportional to the square of the rotating frequency for a given flux-linkage magnitude. Therefore, these core losses impact the overall machine efficiency negatively.

However, the three-phase transformer windings and relatively simple manufacturability of the machine design 2 are outweighed by their overall benefits.

5.2.4 Target Specification for Machine Design 2

The second machine design is tested for both liquid and forced-air cooling applications and built using the machine specifications based upon an existing stator from Magna, as shown in Table 5.2.

Table 5.2: Machine design 2 specifications for liquid (l.c.) and forced-air (a.c.) cooling applications

Parameters	Value (l.c./a.c.)
Stator outer diameter (mm)	220
Rotor outer diameter (mm)	165.6
Shaft outer diameter (mm)	55
Core length (mm)	100
Air-gap length (mm)	0.6
Turns per phase - Stator winding	6 / 4
Turns per phase - Rotor transformer winding	21
Turns per phase - Rotor field winding	250 / 265
Number of poles - Stator winding	10
Number of poles - Rotor transformer winding	10
Number of poles - Rotor field winding	30
Phase numbers - Stator winding	5
Phase numbers - Transformer winding	3
Slot numbers - Stator	50
Slot numbers - Rotor	30
Slot packing factor	0.5
Rated (base) speed (RPM)	2779
Maximum speed (RPM)	9094
DC bus voltage (VDC)	325 / 130
Maximum line-to-line voltage (V_{rms})	200 / 66.5
Maximum phase current (A_{rms})	390 / 111.2
Maximum current density per slot (A_{rms}/mm^2)	30 / 10
Winding temperature (°C)	120
Type of Iron	M350-50A

CHAPTER 6

Simulation Results

6.1 Machine Design 1 using Liquid Cooling Specification

### 6.1.1 Independent Harmonic Excitations at Rated (Base) Motor Speed

In order to verify the operation of the proposed machine topology accurately, the finite element analysis (FEA) software ANSYS Maxwell 2D and Circuit is used to develop a nonlinear magnetics model of the proposed machine design, which includes the diode rectifier circuit model in the rotor, based on the machine specification in Table 5.1. The phase resistances and inductances of all windings in the FEA model, which include end-turn effects, are calculated based on the operating temperature of 120°C using ANSYS Motor-CAD. Using the FEA tool, the capability of independent coupling with the rotor windings is simulated and validated. Additionally, desired operating conditions of the machine, where the stator harmonic components simultaneously couple with the transformer and field windings to produce a torque, are demonstrated at three key operating speeds.

The five-phase machine with a single-phase transformer winding design is simulated which has a ten-pole design in the stator design using the distributed winding type, and rotor windings using the concentrated winding type.

In the first operating condition, the stator windings are excited with third spatial harmonic currents only to induce voltage in the single-phase transformer winding in the rotor through the third spatial harmonic coupling at the base motor speed (2779 RPM). Figure 6.1 shows that the DC third spatial harmonic currents ($I_3 = 100$ A and $f_3 = 0$ Hz) excite the transformer winding
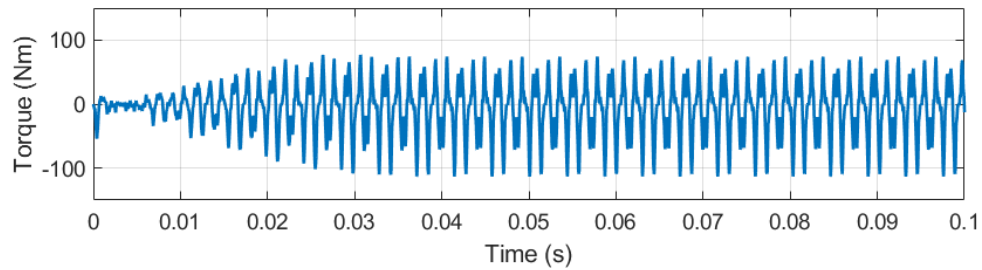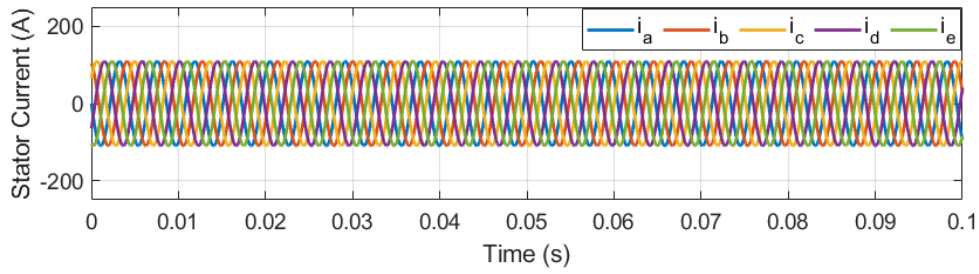
131
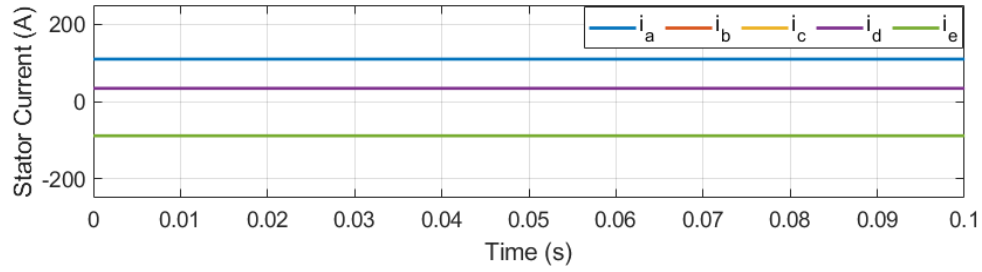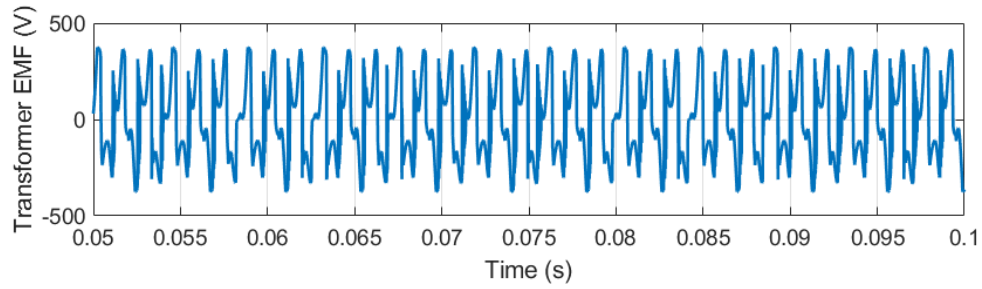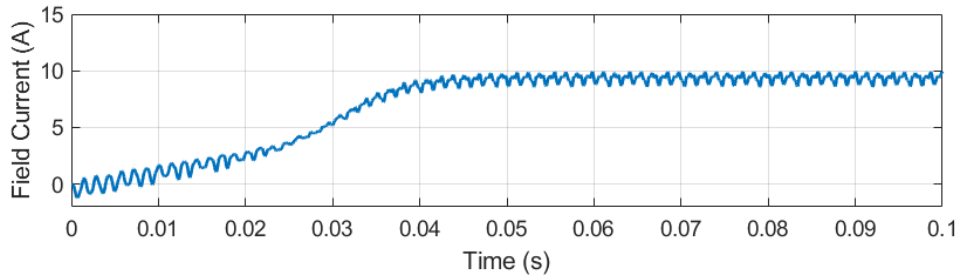
Figure 6.1: Simulation of third spatial harmonic current excitation at base speed (2779 RPM) for machine design 1. (a) Stator currents with DC third harmonic ($I_1 = 0$ A, $f_1 = 0$ Hz, $I_3 = 100$ A, $f_3 = 0$ Hz). (b) Induced transformer voltage. (c) Field current. (d) Electromagnetic torque.

and induce sinusoidal voltage and current, which then produce DC field current ($I_f = 9$ A) in the field winding through rectification. In this case, a small torque is being generated from the rotation of the rotor and the transformer windings that are induced as a result of the stator currents. Because the stator currents are DC, there is essentially no power flowing from the stator to the rotor. Therefore, the power generated by the torque is converted into electrical power by the transformer windings and used to generate the field current. This excitation does not produce the desired torque, as the fundamental spatial harmonic currents are not injected in the stator winding, but is meant to demonstrate that the field current can be produced by the third spatial harmonic component.

In the second operating condition, the stator windings are excited with the fundamental spatial harmonic currents only at the base speed. The stator windings are excited with AC fundamental spatial harmonic currents that are rotating synchronously with the rotor speed. Figure 6.2 presents FEA results of induced transformer current, field current, and torque. Although the transformer winding is mainly excited with the third spatial harmonic component, there are certain amounts of the voltage and current induced in the transformer winding because only one-third of the thirty poles of the transformer cores and windings could be fit in the machine design 1. There are increased common harmonics at additional spatial harmonics, as shown in Figure 5.3, which produce this transformer voltage, therefore generating torque.

In the third operating condition, both fundamental and third spatial harmonic currents are simultaneously applied to the stator windings to simultaneously couple with both rotor windings and produce the desired torque. Fig. 6.3 presents FEA results where peak torque is achieved under the voltage constraint. The optimum excitation parameters were determined using a parametric sweep in finite-element simulation. The magnitudes of the fundamental current and the third harmonic current are set to 312.1 A and 110 A, respectively. The resulting induced transformer voltages generate a DC field current of 7.5 A through rectification, which in turn produces torque of 275 Nm. It can be observed that a significant amount of torque ripple is produced due to having a single-phase transformer winding where the power transfer is oscillatory.
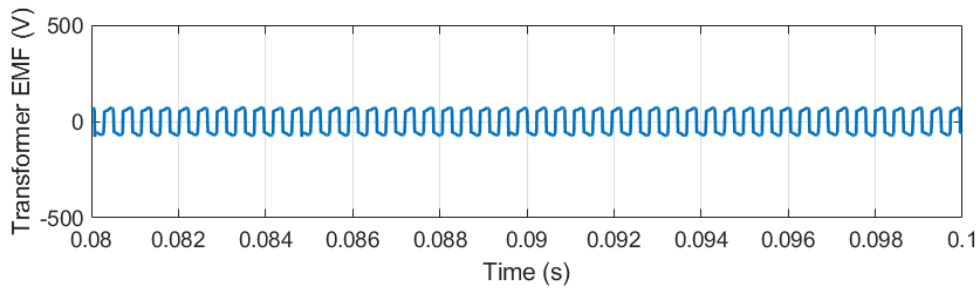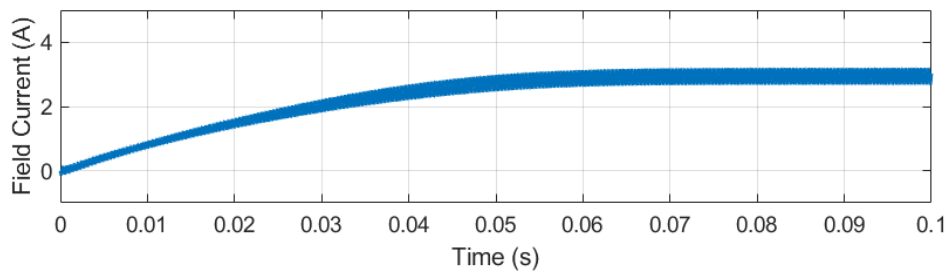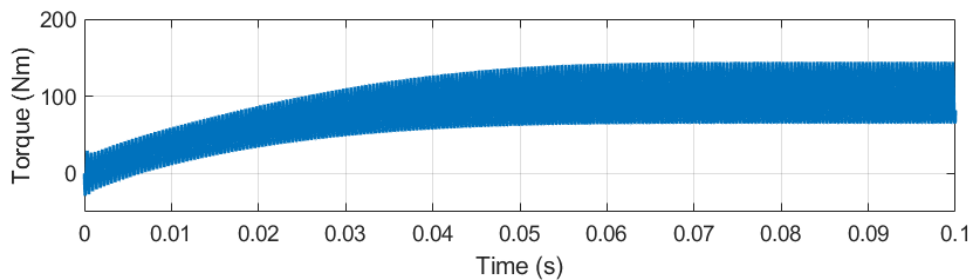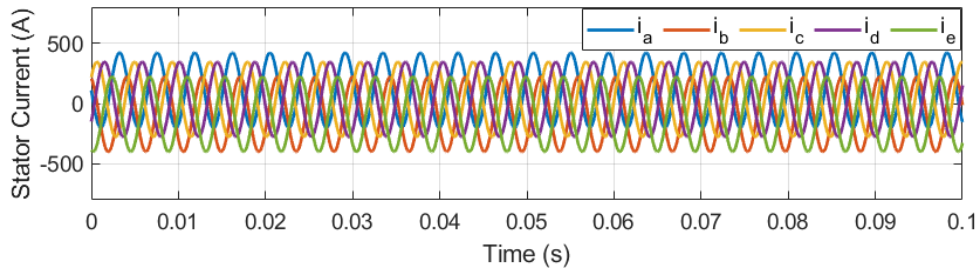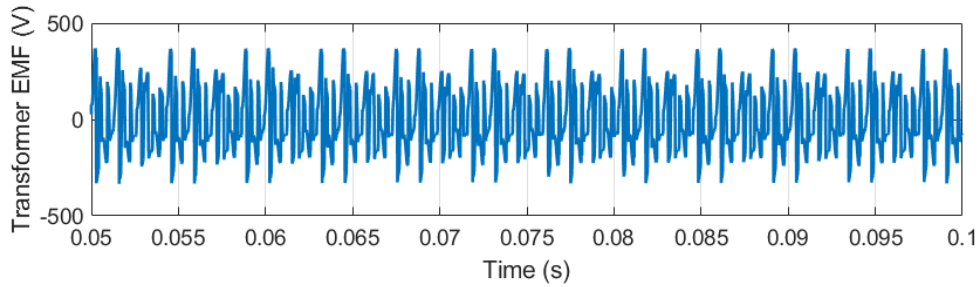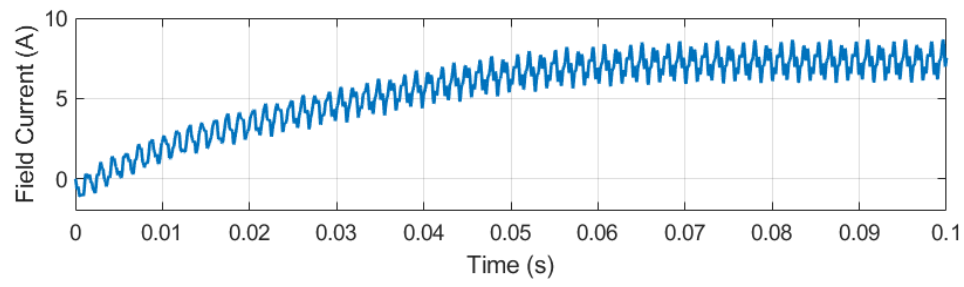
Figure 6.2: Simulation of fundamental spatial harmonic current excitation at base speed (2779 RPM) for machine design 1. (a) Stator currents with AC fundamental harmonic ($I_1 = 100$ A, $f_1 = 46.3$ Hz, $I_3 = 0$ A, $f_3 = 0$ Hz). (b) Induced transformer voltage. (c) Field current. (d) Electromagnetic torque.
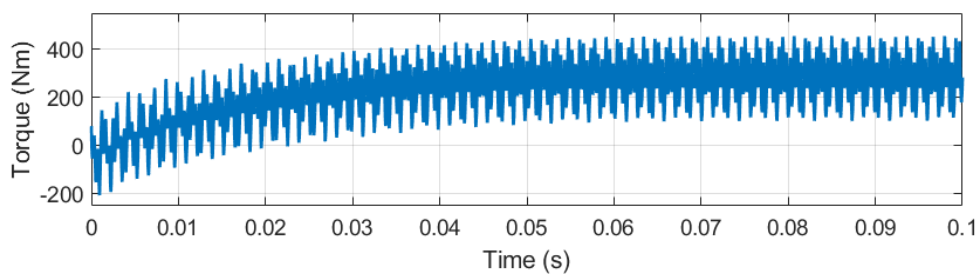
Figure 6.3: Simulation of both fundamental and third spatial harmonic currents at base speed (2779 RPM) for machine design 1. (a) Stator currents with fundamental and third harmonic ($I_1 = 312.1$ A, $f_1 = 46.3$ Hz, $I_3 = 110$ A, $f_3 = 0$ Hz). (b) Induced transformer voltage. (c) Field current. (d) Electromagnetic torque.

6.1.2 Torque Capability at Zero and Maximum Motor Speeds

Torque production at zero speed is an important feature for ensuring that the machine can start reliably. For the proposed machine approach for the zero-speed operation, an additional frequency component corresponding to the spatial harmonic currents exciting the transformer windings is injected in order to induce voltage in the transformer winding. Injecting the frequency component at low speeds is feasible as the voltage is not constrained.

Figure 6.4 presents FEA results for machine design 1 at zero speed. The peak torque rating of 275 Nm is met using AC third spatial harmonic currents ($I_3 = 120$ A and $f_3 = 1.2$ kHz) and the fundamental spatial harmonic currents ($I_1 = 308$ A).

Fig. 6.5 presents FEA results at the maximum speed of 9094 RPM. At the maximum speed, DC third spatial harmonic currents are used to minimize the stator voltages, therefore maximizing torque within the voltage constraint. At the operations above the base speed, the stator voltage is constrained due to the back-EMF of the machine. To ensure that the stator voltages stay within the voltage constraint, the machine model was excited using the voltage method instead of current including both fundamental and third harmonic components. The magnitudes of the fundamental direct- and quadrature-axis voltages, and the third harmonic voltage are set to 199.9 V, 6.8 V, and 7 V, respectively. The frequency of the third harmonic voltage is set to DC to minimize its effect on the overall stator voltage, and the frequency of the fundamental harmonic voltage is matched to the electrical rotor speed. The resulting induced transformer voltages generate a DC field current of 8 A through rectification, and a torque of 83 Nm. Note that the torque ripple increases as it is proportional to the rotating frequency.
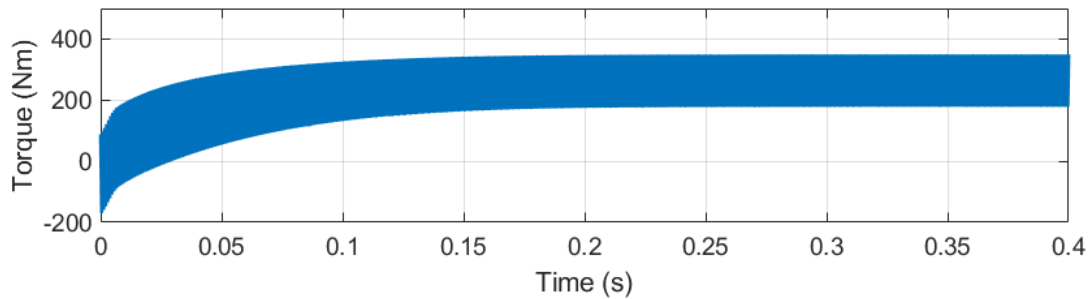
The simulation results of the machine design with the single-phase transformer winding achieve the CPWSR capability. However, the single-phase transformer design transferring an oscillating power from the transformer EMF to the torque results in significantly large torque ripples which cause mechanical vibrations and noises.
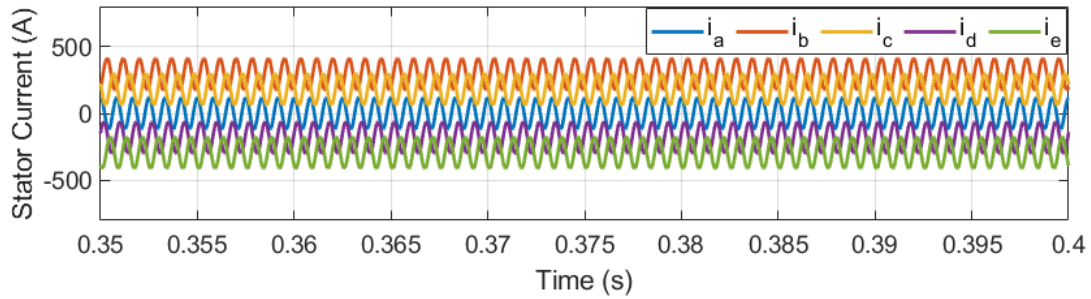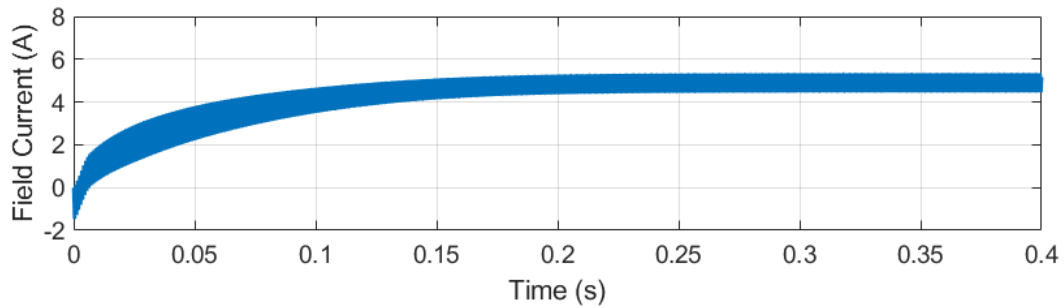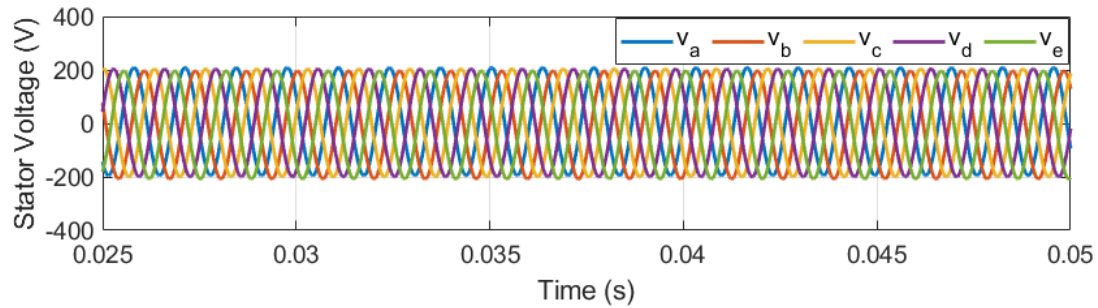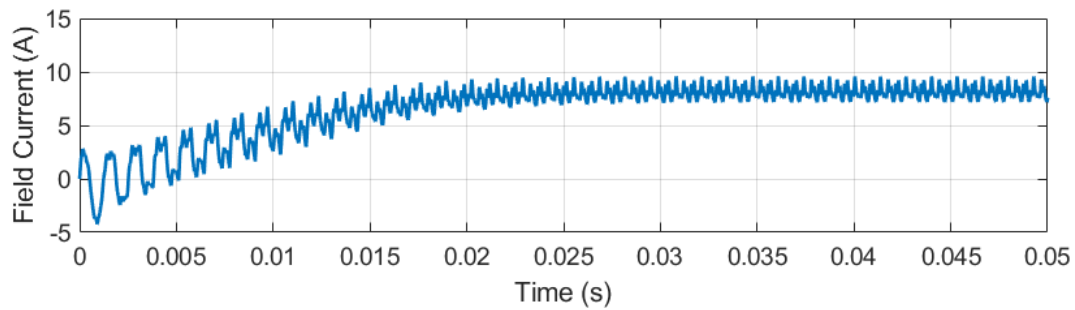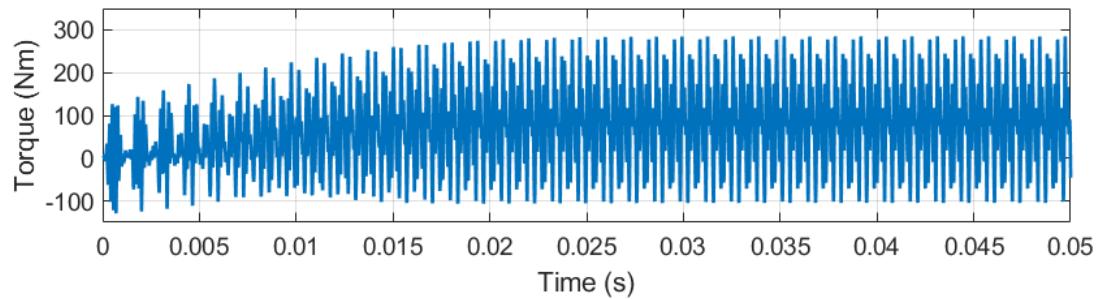
Figure 6.4: Torque production at zero speed for machine design 1. (a) Stator currents with fundamental and third harmonics ($I_1 = 308$ A, $I_3 = 120$ A, $f_1 = 0$ Hz, $f_3 = 1.2$ kHz). (b) Rotor field current. (c) Electromagnetic torque.

Figure 6.5: Torque production at maximum speed (9094 RPM) for machine design 1 using the liquid cooling specification. (a) Input stator voltages with fundamental and third harmonics ($V_{d1} = -199.9$ V, $V_{q1} = 6.8$ V, $V_3 = 7$ V, $f_1 = 151.6$ Hz, $f_3 = 0$ Hz). (b) Rotor field current. (c) Electromagnetic torque.

6.1.3 Load Points and Efficiency Tests

The efficiency of machine design 1 based upon liquid cooling specification is investigated using selected load points. The load points are selected due to the long FEA simulation time required for the proposed machine design in ANSYS Maxwell.

Tables 6.1 and 6.2 show the efficiency results at these load points. For the load points requiring speeds below the base speed (1, 2, 3, 6, 10, and 11), the FEA model is simulated using a current excitation method. For the load points requiring speeds above the base speed (4, 5, 7, 8, and 9), the FEA model is simulated using a voltage excitation method.

Among the load points, the machine achieves relatively high efficiency from mid- to high-speeds with a torque requirement below 50 Nm. This is because the proposed machine is capable of operating at low torque levels and high speeds more efficiently by simply reducing the rotor field current, whereas the PM machine requires significant amounts of stator current for field weakening at high speeds, which reduces its efficiency.

Configuration	Load Point 1	Load Point 2	Load Point 3	Load Point 4	Load Point 5
Speed (RPM)	1250	2750	500	8000	4000
Torque (Nm)	40	25	125	40	50
Bus voltage (V)	360	360	360	360	360
Excitation method	Current	Current	Current	Voltage	Voltage
Fundamental current magnitude (A_{rms})	33.2	28.3	102.6	86.8	71.1
Third harmonic current magnitude (A_{rms})	12.7	7.1	7.1	25.3	15.2
Total phase current magnitude (A_{rms})	35.6	29.2	102.6	90.4	72.7
DC field current (A)	1.7	1.4	1.7	4.2	2
Peak-peak torque ripple (%)	152	109.2	101.5	251.7	88.4
Stator copper losses (W)	352.5	236.8	2900	2300	1500
Rotor copper losses (W)	63.8	44.3	66.1	387.9	85.4
Total iron losses (W)	108	319.6	30.9	1500	424.9
Motor Efficiency (%)	90.8	92.3	68.4	88.9	91.4

Table 6.1: Efficiency tests using load points 1-5

Configuration	Load Point 6	Load Point 7	Load Point 8	Load Point 9	Load Point 10	Load Point 11
Speed (RPM)	1250	9500	9000	3000	2779	2779
Torque (Nm)	-30	80.5	42	250	137.5	275
Bus voltage (V)	360	360	275	325	275	325
Excitation method	Current	Voltage	Voltage	Voltage	Current	Current
Fundamental current magnitude (A_{rms})	41	123.3	78.3	220	130.2	220.7
Third harmonic current magnitude (A_{rms})	0.7	89	25.5	88.8	76	77.8
Total phase current magnitude (A_{rms})	41	152	82.3	237	150.8	234
DC field current (A)	1.2	8.2	4.5	4	5.1	7.3
Peak-peak torque ripple (%)	31.1	420	240	49.8	180	68.8
Stator copper losses (W)	468.7	6400	1900	15700	6300	15300
Rotor copper losses (W)	31.7	1500	451.5	368.9	590.5	1200
Total iron losses (W)	78.6	3200	1700	970.9	463.6	1200
Motor Efficiency (%)	85.6	87.6	90.5	82.3	84.4	82

Table 6.2: Efficiency tests using load points 6-11

6.2 Machine Design 2 using Liquid Cooling Specification

### 6.2.1 Independent Harmonic Excitations at Rated (Base) Motor Speed

Using the FEA tool, the capability of independent coupling with the rotor windings is simulated and validated for the second machine design using the liquid cooling specification based on Table 5.2.

In order to induce voltages in the three-phase transformer windings in the rotor through the fundamental spatial harmonic coupling, the five-phase stator windings are excited with fundamental spatial harmonic currents only. Figure 6.6 presents FEA results with only fundamental currents at the base motor speed (2779 RPM). The peak fundamental current I_1 is set to 100 A and the frequency of the fundamental current w_1 is set to zero. The fundamental currents excite the transformer winding and induce three-phase voltages and currents, which then produce a DC current in the field winding ($I_f = 3$ A) through rectification. In this case, a small torque is being generated from the rotation of the rotor and the transformer windings that are induced as a result of the stator currents. Because the stator currents are DC, there is essentially no power flowing from the stator to the rotor. Therefore, the power generated by the torque is converted into electrical power by the transformer windings and used to generate the field current. This excitation does not produce the desired torque, as the third spatial harmonic currents are not injected in the stator winding, but is meant to demonstrate that the field current can be independently produced by the fundamental spatial harmonic component.

Figure 6.7 presents FEA results with only third spatial harmonic currents at the base speed. The stator windings are excited with AC third spatial harmonic currents that are rotating synchronously with the rotor speed ($\omega_3 = 3\frac{N_p}{2}\omega_r$). Since the transformer windings are mainly excited with the fundamental spatial harmonic component by design, the induced transformer voltages using the third spatial harmonic currents are small when compared to those generated by the fundamental currents. These induced voltages are generated due to the slot harmonics of the stator and harmonic coupling between some sub-harmonic components (e.g., 7th, 13th, ...). As a result, the excitation
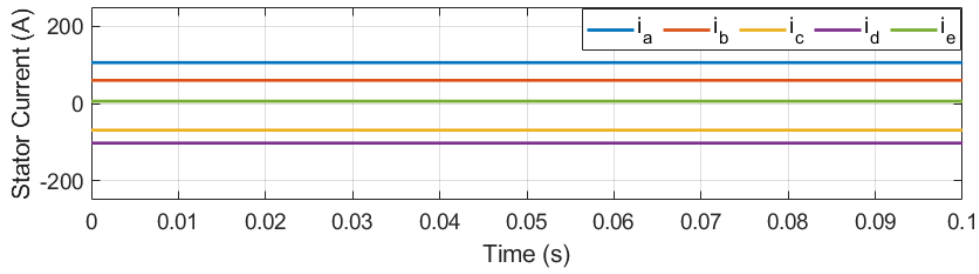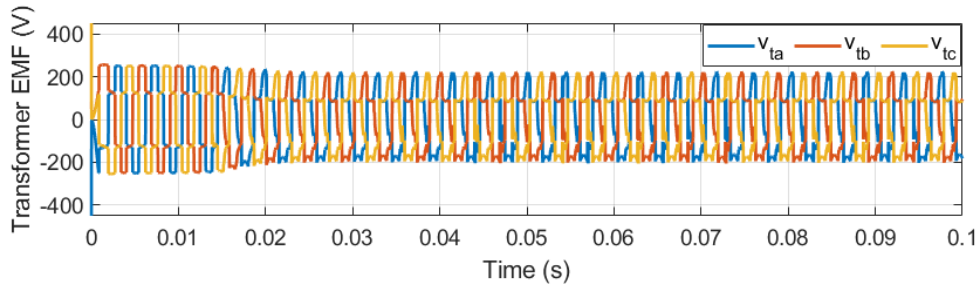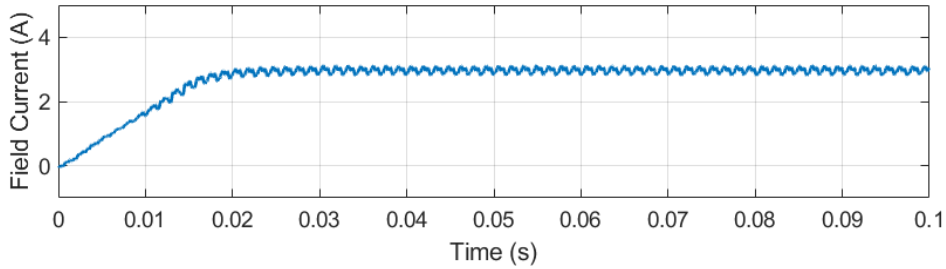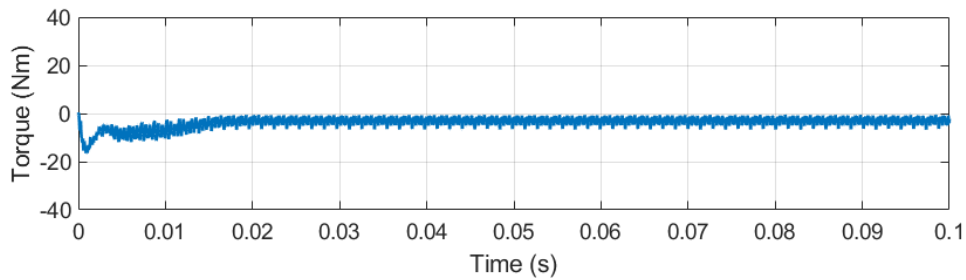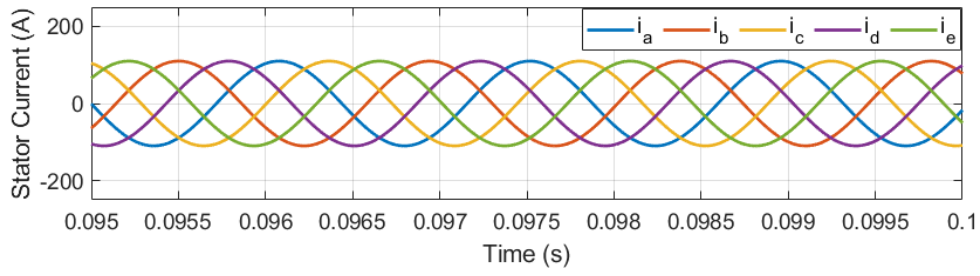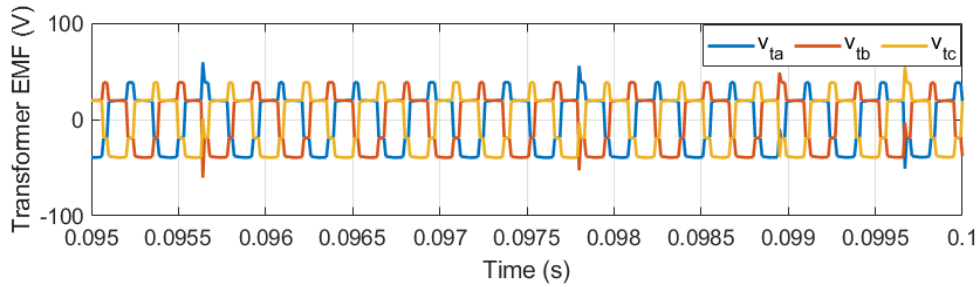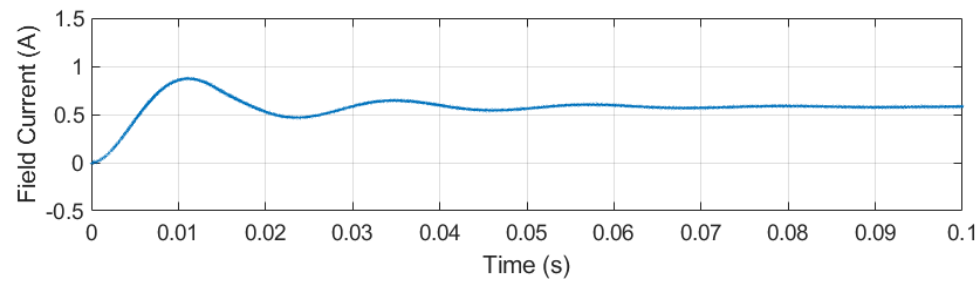
Figure 6.6: Simulation of fundamental spatial harmonic current excitation at base speed (2779 RPM) for machine design 2 using the liquid cooling specification. (a) Stator currents with DC fundamental harmonic ($I_1 = 100$ A, $f_1 = 0$ Hz, $I_3 = 0$ A, $f_3 = 0$ Hz). (b) Induced transformer voltages. (c) Rotor field current. (d) Electromagnetic torque.
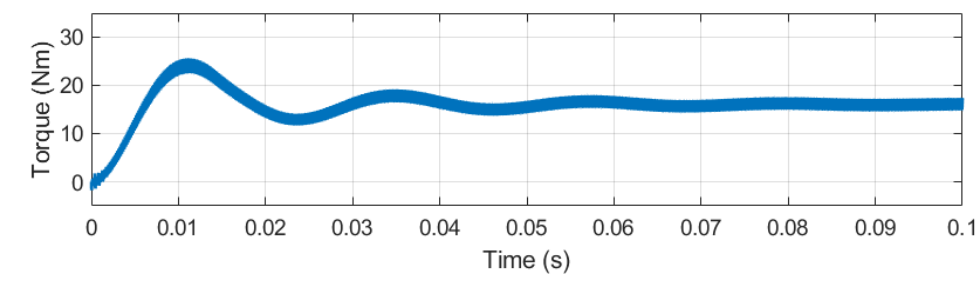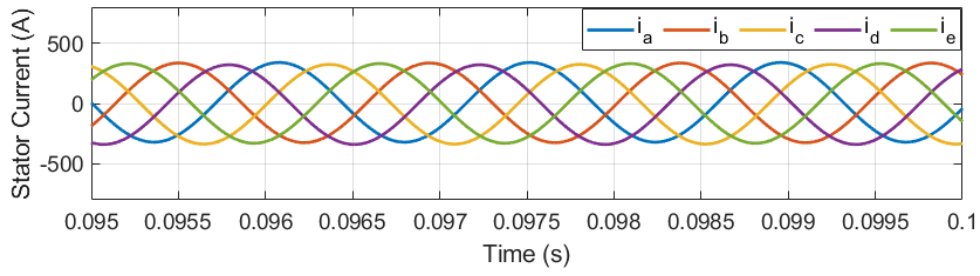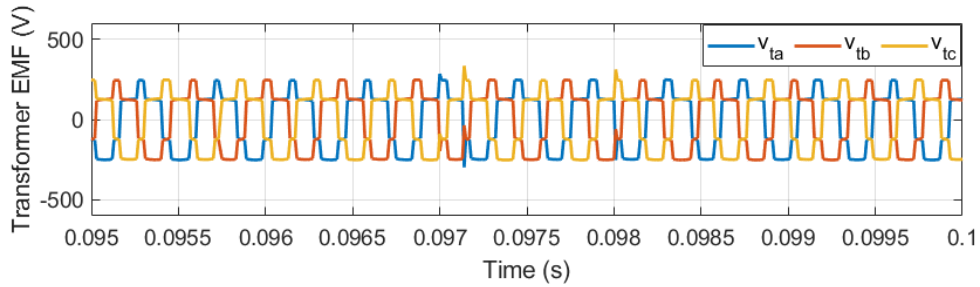
Figure 6.7: Simulation of third spatial harmonic current excitation at base speed (2779 RPM) for machine design 2 using the liquid cooling specification. (a) Stator currents with AC third harmonic ($I_1 = 0$ A, $f_1 = 0$ Hz, $I_3 = 100$ A, $f_3 = 139$ Hz). (b) Induced transformer voltages. (c) Rotor field current. (d) Electromagnetic torque.

produces a relatively small amount of field current and hence torque ($I_f = 0.6$ A and $\tau = 16$ Nm).

Finally, both fundamental and third spatial harmonic currents are simultaneously applied to the stator windings to produce the desired torque. Figure 6.8 presents FEA results where peak torque is achieved under the current and voltage constraint. The optimum excitation parameters were determined using a parametric sweep in finite-element simulation. The magnitudes of the fundamental spatial harmonic current and the third spatial harmonic current are set to 20 A and 330.3 A respectively. The fundamental spatial harmonic currents are set to DC to minimize its impact on the stator voltages. The resulting induced transformer voltages generate a DC field current of 3.9 A through rectification, which in turn produces torque of 170 Nm.
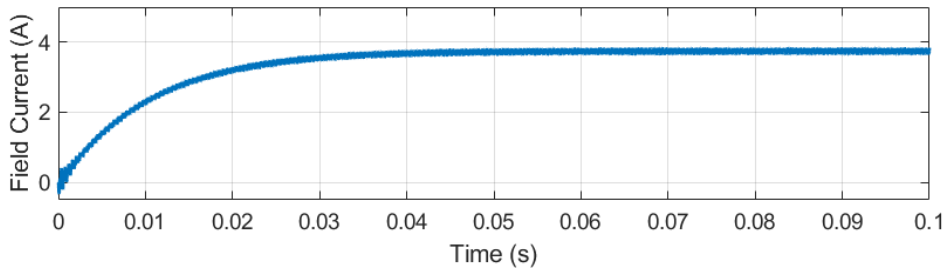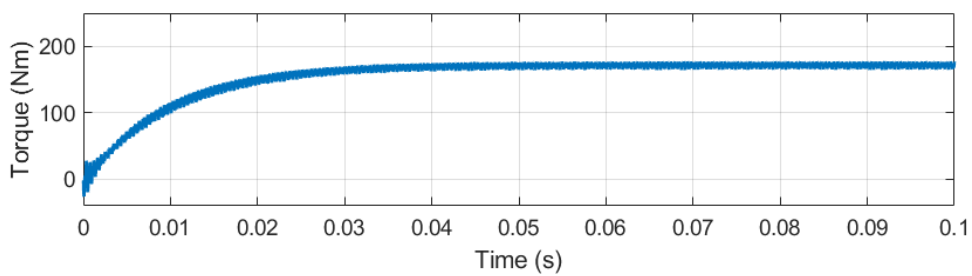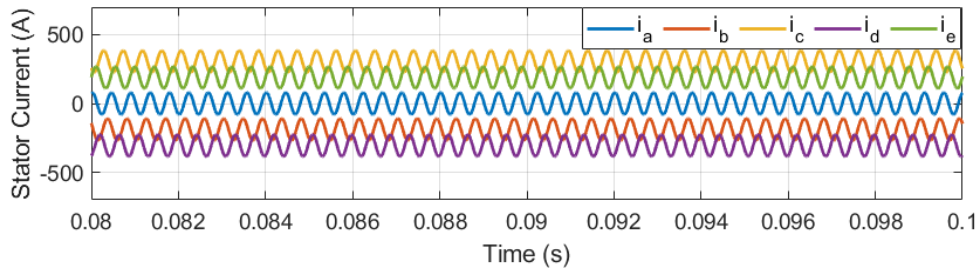
Figure 6.8: Simulation of both fundamental and third spatial harmonic currents at base speed (2779 RPM) for machine design 2 using the liquid cooling specification. (a) Stator currents with fundamental and third harmonics ($I_1 = 20$ A, $f_1 = 0$ Hz, $I_{d3} = 0$ A, $I_{q3} = 330.3$ A, $f_3 = 139$ Hz). (b) Induced transformer voltages. (c) Rotor field current. (d) Electromagnetic torque.

6.2.2 Torque Capability at Zero and Maximum Motor Speeds

Torque productions at zero speed and maximum speed are simulated for the second machine design using the liquid cooling specification. Figure 6.9 presents FEA results at zero speed. The magnitudes of the fundamental and third spatial harmonic currents are set to 80 A and 321 A, respectively. In order to induce voltages in the transformer windings at zero speed, the frequency of the fundamental currents (f_1) is set to -450 Hz. The resulting induced transformer voltages generate a DC field current of 3.8 A through rectification, and an average torque of 170 Nm is produced by the machine.

Figure 6.10 presents FEA results at the maximum speed of 9094 RPM. To ensure that the stator voltages stay within the voltage constraint, the machine stator was excited in ANSYS Maxwell using the voltage method instead of current including both fundamental and third harmonic components. The magnitudes of the fundamental voltage, and the third harmonic direct- and quadrature-axis voltages are set to 0.5 V, 190.8 V, and 60 V, respectively. The frequency of the fundamental voltage is set to DC to minimize its effect on the overall stator voltage, and the frequency of the third harmonic voltage is matched to the electrical rotor speed. The resulting induced transformer voltages generate a DC field current of 3.8 A through rectification, and produce torque of 75 Nm. Note that the torque ripple for the second machine design is significantly lower than that from the first machine design due to the three-phase transformer winding design.
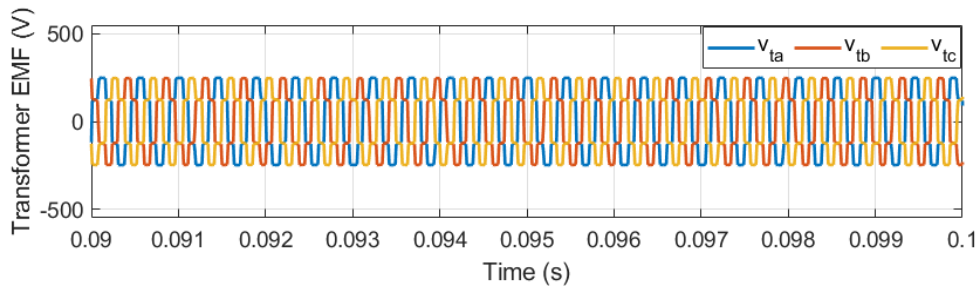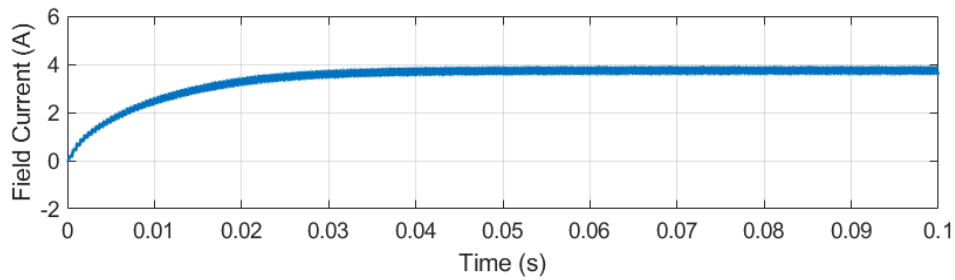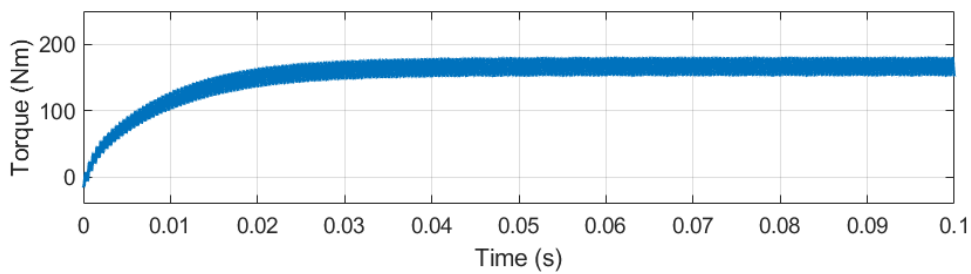
Figure 6.9: Torque production at zero speed for machine design 2 using the liquid cooling specification. (a) Stator currents with fundamental and third harmonics ($I_1 = 80$ A, $I_3 = 321$ A, $f_1 = -450$ Hz, $f_3 = 0$ Hz). (b) Induced transformer voltages. (c) Rotor field current. (d) Electromagnetic torque.
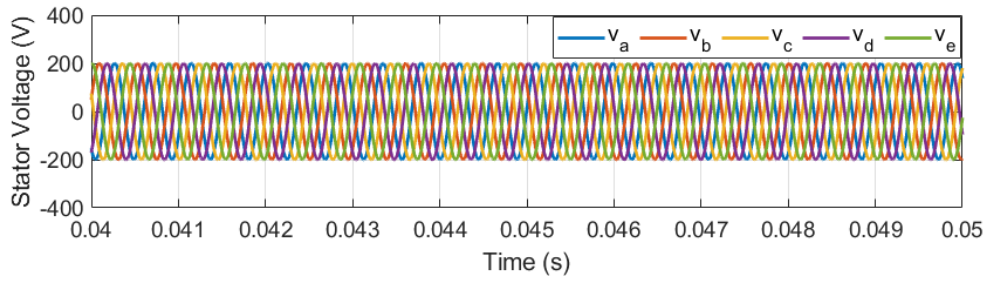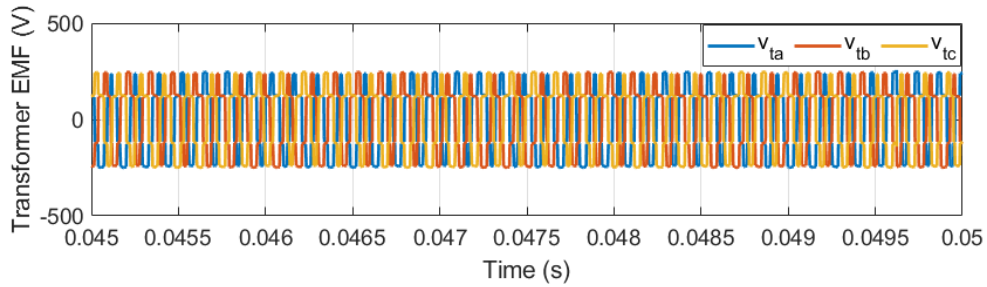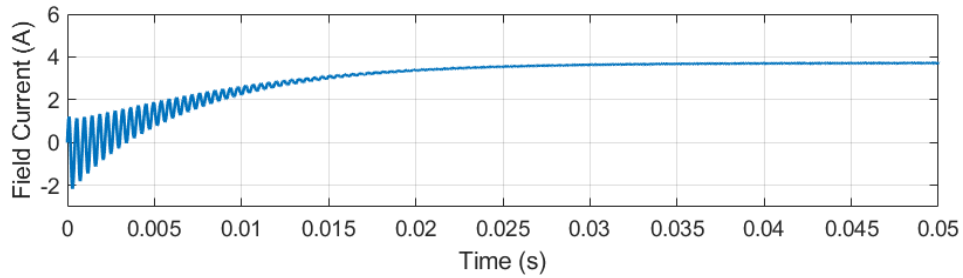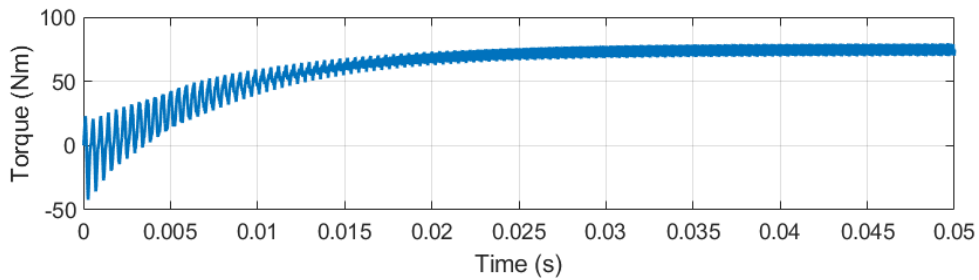
Figure 6.10: Torque production at maximum speed (9094 RPM) for machine design 2 using the liquid cooling specification. (a) Input stator voltages with fundamental and third harmonics ($V_1 = 0.5$ V, $V_{d3} = -190.8$ V, $V_{q3} = 60$ V, $f_1 = 0$ Hz, $f_3 = 455$ Hz). (b) Induced transformer voltages. (c) Rotor field current. (d) Electromagnetic torque.

6.2.3 Maximum Torque Per Ampere (MTPA) and Current Density

The simulations of the machine design 2 based upon the liquid cooling specification show significant improvement in the torque ripple. However, when compared to the machine design 1, its peak torque capability is decreased due to the saturation of the main torque flux which reduced the couplings of the transformer winding. In order to find the optimal torque capability of this machine design, the maximum torque per ampere (MTPA) is investigated with respect to different current densities. The result determines an optimal current density that produces the peak torque performance.

The machine is simulated at a fixed motor speed at 1400 RPM, and the magnitudes of both the fundamental and third spatial harmonic currents are adjusted proportionally based upon various current density levels. Figure 6.11 shows that the peak MTPA performance is achieved at the current density of 10 A_{rms}/mm^2. One of the reasons for the performance degradation above the current density of 10 A_{rms}/mm^2 is the saturation of teeth regions in the stator and the rotor. Figure 6.12 shows that the produced DC field current in the rotor saturates above the current density of 10 A_{rms}/mm^2. Note that this current density typically corresponds to forced convection applications [48]. Therefore, the second machine design is going to be simulated using the current density of 10 A_{rms}/mm^2 in the following sections.
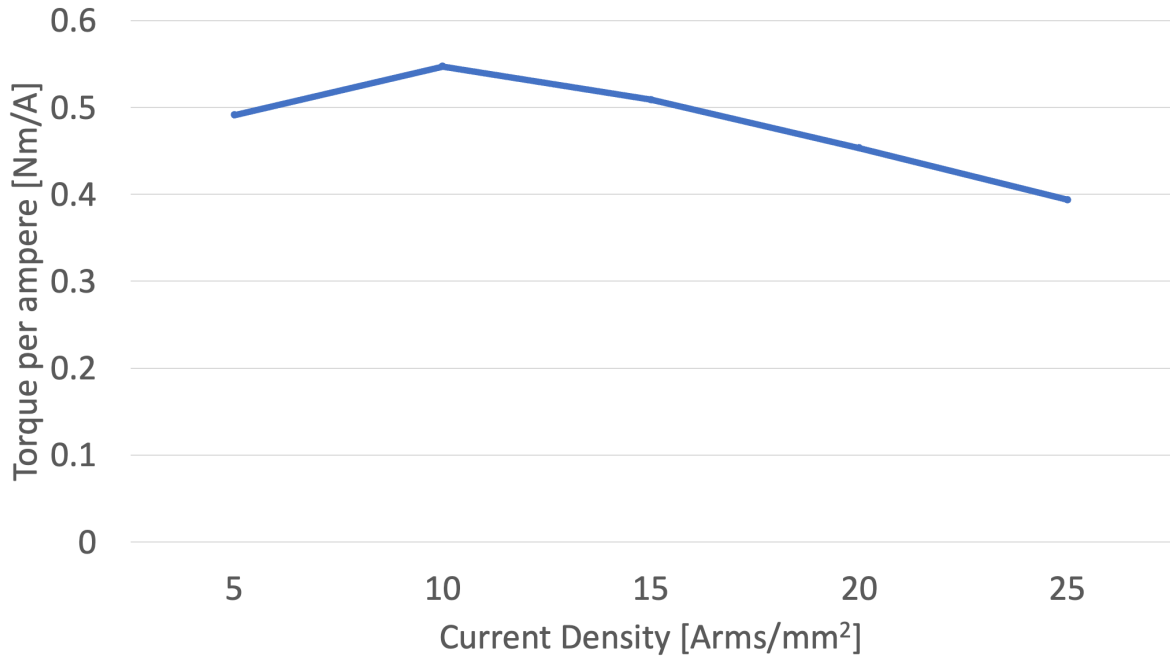
Figure 6.11: Maximum torque per ampere vs. current density at 1400 RPM
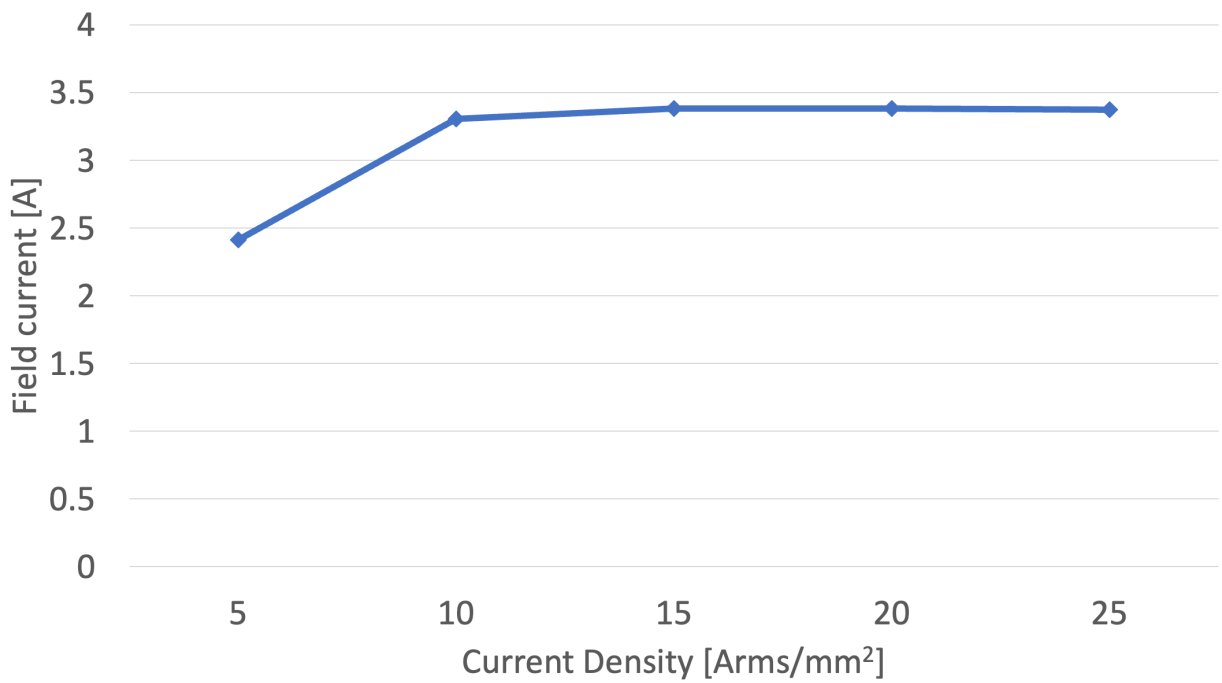

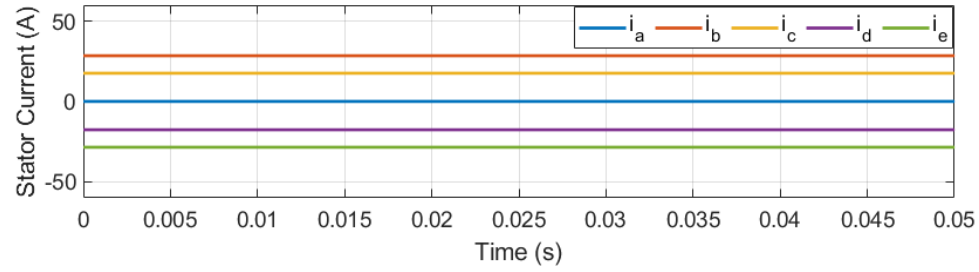Figure 6.12: Rotor field current vs. current density at 1400 RPM

151

6.3 Machine Design 2 using Forced-air Cooling Specification

### 6.3.1 Independent Harmonic Excitations at Rated (Base) Motor Speed

Using the FEA tool, the capability of independent coupling with the rotor windings is simulated and validated for the second machine design using the forced-air cooling specification based on Table 5.2.

In order to induce voltages in the three-phase transformer windings in the rotor through the fundamental spatial harmonic coupling, the five-phase stator windings are excited with fundamental spatial harmonic currents only. Figure 6.13 presents FEA results with only fundamental currents at the base motor speed (2779 RPM). The peak fundamental current I_1 is set to 30 A and the frequency of the fundamental current w_1 is set to zero. The fundamental currents excite the transformer winding and induce three-phase voltages and currents, which then produce a DC current in the field winding ($I_f = 2.1$ A) through rectification. In this case, a small torque is being generated from the rotation of the rotor and the transformer windings that are induced as a result of the stator currents. Because the stator currents are DC, there is essentially no power flowing from the stator to the rotor. Therefore, the power generated by the torque is converted into electrical power by the transformer windings and used to generate the field current. This excitation does not produce the desired torque, as the third spatial harmonic currents are not injected in the stator winding, but is meant to demonstrate that the field current can be independently produced by the fundamental spatial harmonic component.

Figure 6.14 presents FEA results with only third spatial harmonic currents at the base speed. The stator windings are excited with AC third spatial harmonic currents that are rotating synchronously with the rotor speed ($\omega_3 = 3\frac{N_p}{2}\omega_r$). For a fair comparison, the third spatial harmonic current I_3 is set to 90 A, which is three times of the current I_1 in Figure 6.13 to produce the same magnitude of the third spatial harmonic as the fundamental harmonic, as mentioned in Chapter 3. Since the transformer windings are mainly excited with the fundamental spatial harmonic component by design, the induced transformer voltages using the third spatial harmonic currents are small
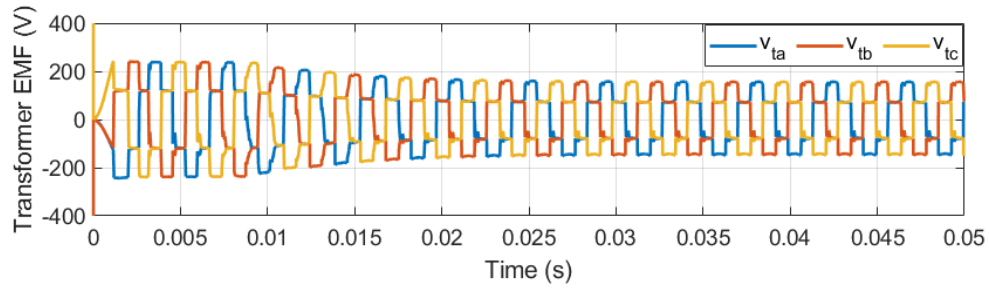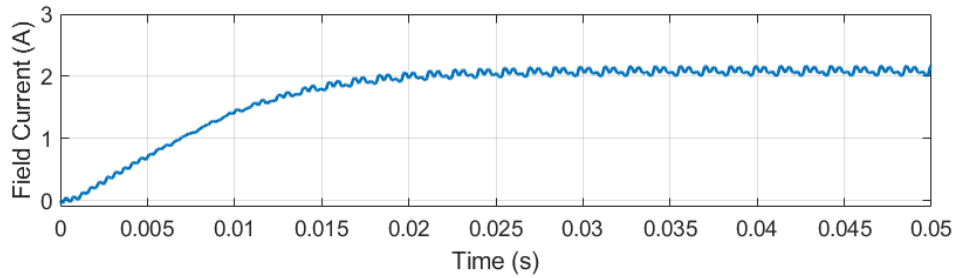
Figure 6.13: Simulation of fundamental spatial harmonic current excitation at base speed (2779 RPM). (a) Stator currents with DC fundamental harmonic ($I_1 = 30$ A, $f_1 = 0$ Hz, $I_3 = 0$ A, $f_3 = 0$ Hz). (b) Induced transformer voltages. (c) Rotor field current. (d) Electromagnetic torque.

Figure 6.14: Simulation of third spatial harmonic current excitation at base speed (2779 RPM). (a) Stator currents with AC third harmonic ($I_1 = 0$ A, $f_1 = 0$ Hz, $I_3 = 90$ A, $f_3 = 139$ Hz). (b) Induced transformer voltages. (c) Rotor field current. (d) Electromagnetic torque.

when compared to those generated by the fundamental currents. These induced voltages are generated due to the slot harmonics of the stator and harmonic coupling between some sub-harmonic components (e.g., 7th, 13th, ...). As a result, the excitation produces a relatively small amount of field current and hence torque ($I_f = 0.11$ A and $\tau = 2.2$ Nm).

Finally, both fundamental and third spatial harmonic currents are simultaneously applied to the stator windings to produce the desired torque. Figure 6.15 presents FEA results where peak torque is achieved under the voltage constraint. The optimum excitation parameters were determined using a parametric sweep in finite-element simulation. The magnitudes of the fundamental current and the third harmonic direct- and quadrature-axis currents are set to 30 A, 30 A, and 151.4 A, respectively. The frequency of the fundamental currents is set to -80 Hz, which maximizes the resulting current density in the field winding. The sign of the electrical frequency of the fundamental currents needs to be opposite that of the rotor speed since the frequency seen by the transformer windings is equal to the difference between the fundamental current frequency and the electrical rotor speed ($\omega_1 - \omega_{re}$). The resulting induced transformer voltages generate a DC field current of 3.3 A through rectification, which in turn produces torque of 86 Nm.

The air-gap flux density components by each winding excitation are presented in Fig. 6.16. For this simulation, a linear magnetic model is used to allow the superposition of the individual flux densities. The additions of the fundamental harmonic stator current and the induced transformer current show an effect on the overall air-gap flux distribution. At this operating point, the peak air-gap flux density is increased by the fundamental harmonic stator current but is almost unaffected by the induced transformer current. For high torque operations, the increased flux level due to the fundamental harmonic current influences torque production since certain parts of the magnetic cores experience saturation.
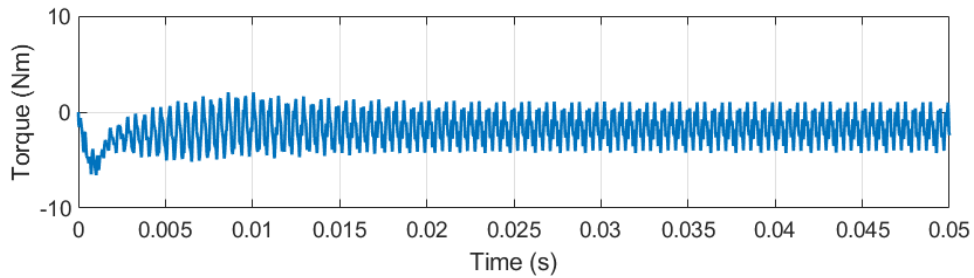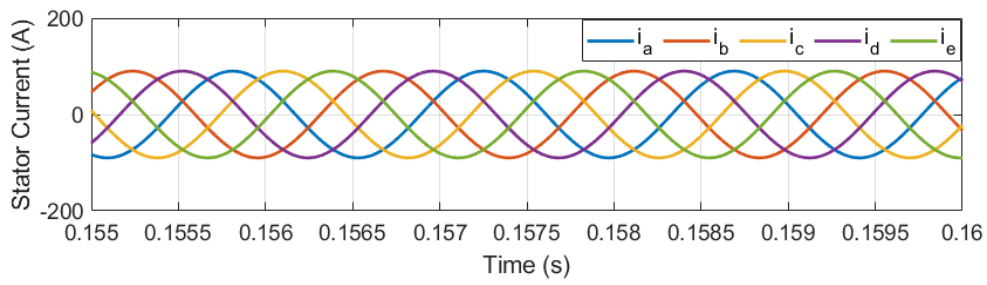
(a)

(b)

(c)
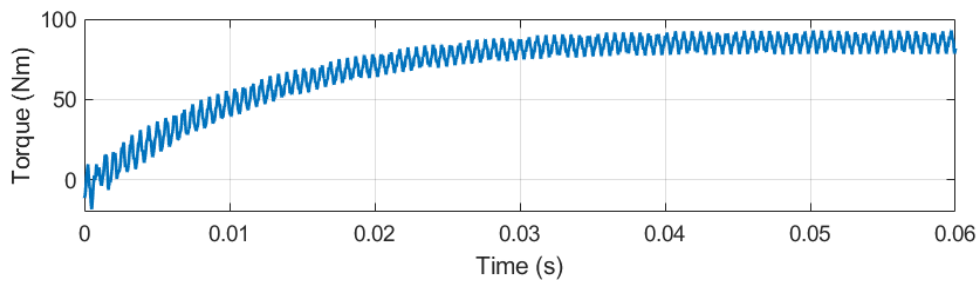
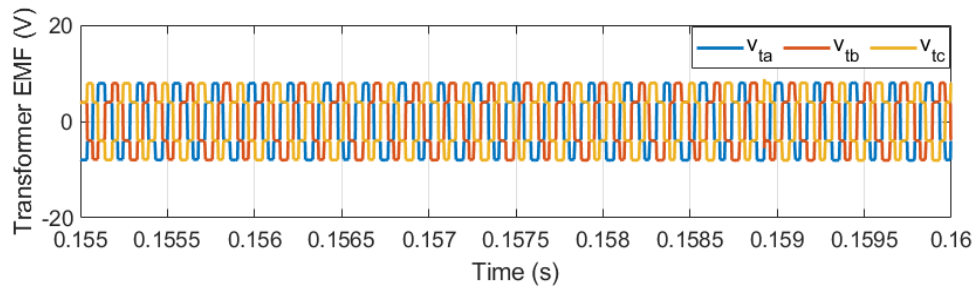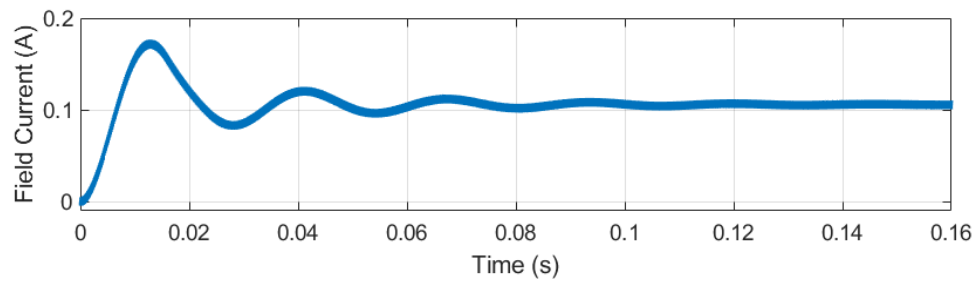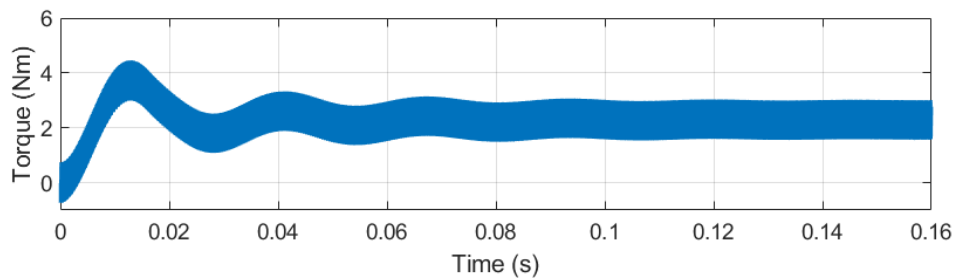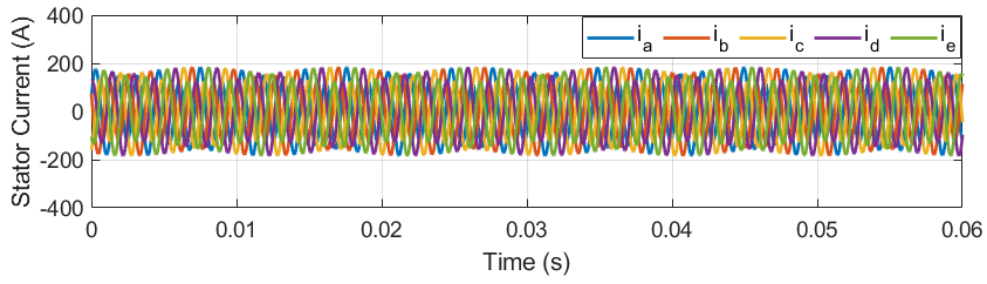(d)

Figure 6.15: Simulation of both fundamental and third spatial harmonic currents at base speed (2779 RPM). (a) Stator currents with fundamental and third harmonics ($I_1 = 30$ A, $f_1 = -80$ Hz, $I_{d3} = 30$ A, $I_{q3} = -151.4$ A, $f_3 = 139$ Hz). (b) Induced transformer voltages. (c) Rotor field current. (d) Electromagnetic torque.
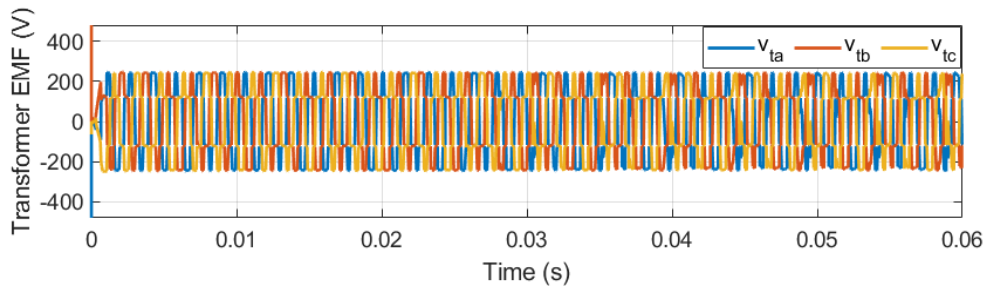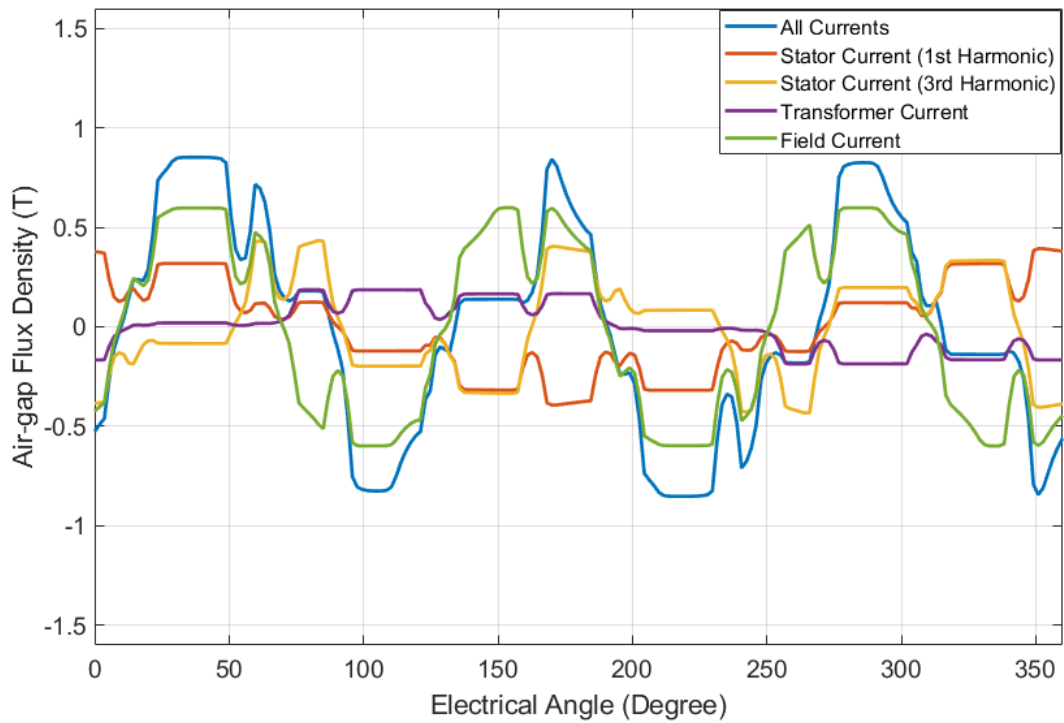
Figure 6.16: Air-gap flux density components due to different currents, linear magnetic model ($I_1 = 30$ A, $f_1 = 0$ Hz, $I_3 = -90$ A, $f_3 = 139$ Hz).

6.3.2 Torque Capability at Zero and Maximum Motor Speeds

Torque productions at zero speed and maximum speed are simulated for the second machine design using the forced-air cooling specification. Figure 6.17 presents FEA results at zero speed. The magnitudes of the fundamental and third spatial harmonic currents are set to 40 A and 152 A, respectively. In order to induce voltages in the transformer windings at zero speed, the frequency of the fundamental currents (f_1) is set to -100 Hz. The resulting induced transformer voltages generate a DC field current of 3.3 A through rectification, and an average torque of 86 Nm is produced by the machine.

Figure 6.18 presents FEA results at the maximum speed of 9094 RPM. To ensure that the stator voltages stay within the voltage constraint, the machine model was excited using the voltage method instead of current including both fundamental and third harmonic components. The magnitudes of the fundamental voltage, and the third harmonic direct- and quadrature-axis voltages are set to 0.2 V, 78.6 V, and 15 V, respectively. The frequency of the fundamental voltage is set to DC to minimize its effect on the overall stator voltage, and the frequency of the third harmonic voltage is matched to the electrical rotor speed. The resulting induced transformer voltages generate a DC field current of 3.3 A through rectification, and a torque of 34 Nm.
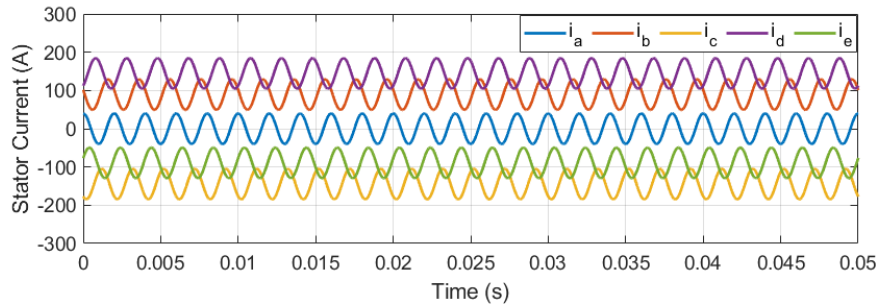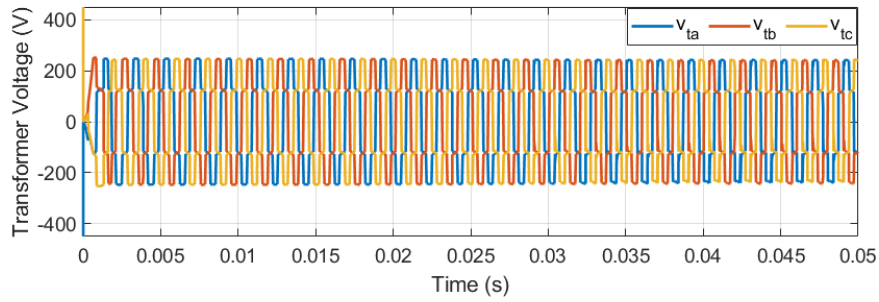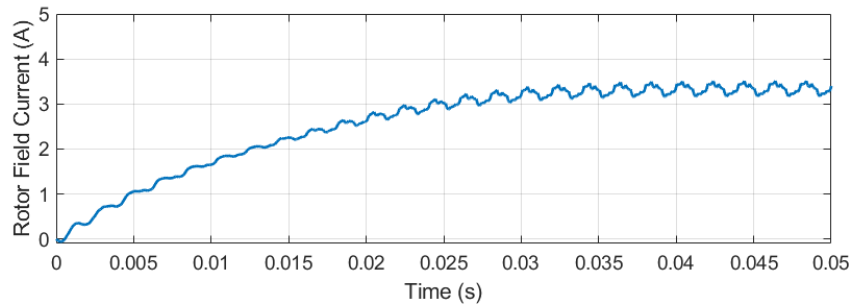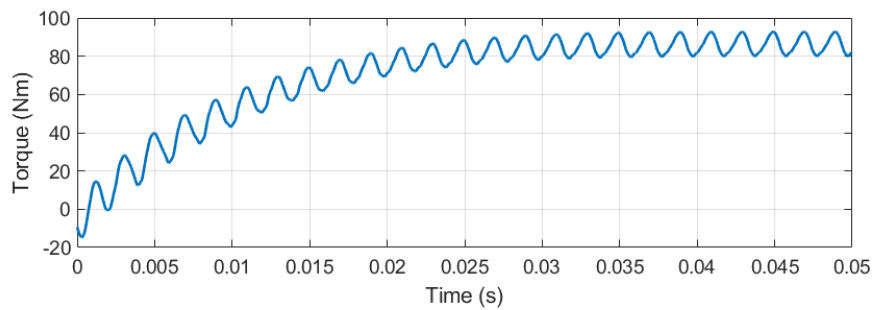
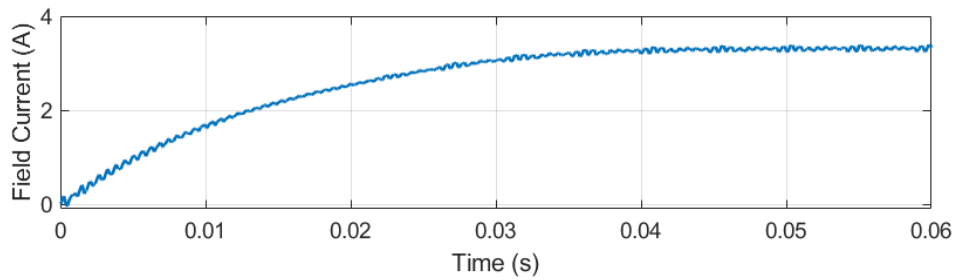Figure 6.17: Torque production at zero speed. (a) Stator currents with fundamental and third harmonics ($I_1 = 40$ A, $I_3 = -152$ A, $f_1 = -100$ Hz, $f_3 = 0$ Hz). (b) Induced transformer voltages. (c) Rotor field current. (d) Electromagnetic torque.
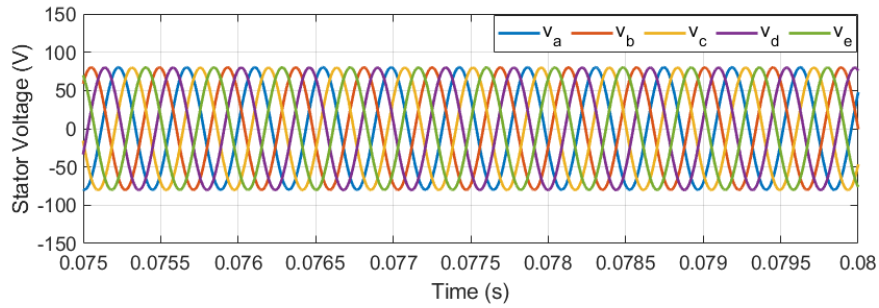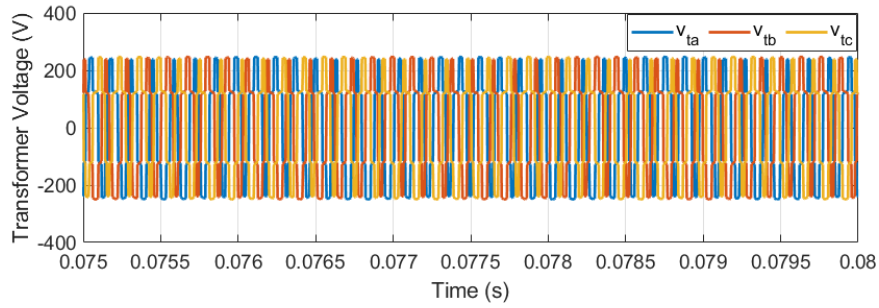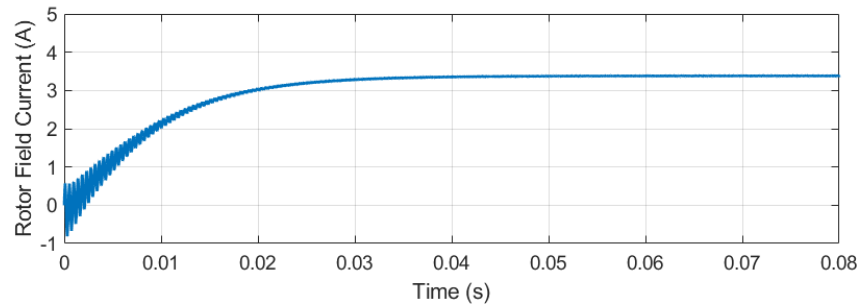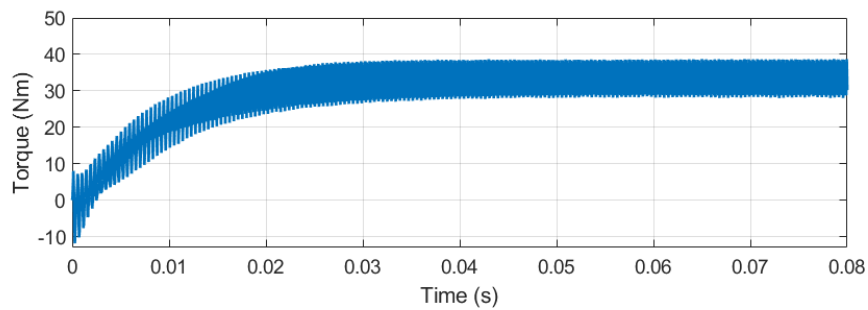
Figure 6.18: Torque production at maximum speed (9094 RPM). (a) Input stator voltages with fundamental and third harmonics ($V_1 = 0.2$ V, $V_{d3} = 78.6$ V, $V_{q3} = -15$ V, $f_1 = 0$ Hz, $f_3 = 455$ Hz). (b) Induced transformer voltages. (c) Rotor field current. (d) Electromagnetic torque.

6.3.3 Comparison of Torque and Power Characteristics with PM and IM

The torque and power capabilities of the proposed BSSFM are compared with an interior permanent-magnet machine (IPM) and an IM topology. In order to compare the BSSFM to existing machines that are commonly used in various industrial applications, a three-phase stator configuration is considered for both IPM and IM. These machines are created and simulated using the same ANSYS Maxwell FEA tool with a similar design specification of the BSSFM, as shown in Fig. 6.19. The IPM design is based on the machine used in the 2010 Toyota Prius [49]. For a fair comparison, the outer diameter and core length of the machine, air-gap length, the number of poles in the stator, and the type of iron are matched to the BSSFM. The number of turns in the stator windings for both IPM and IM is set so that all machines are driven by inverters with the same power rating. Additionally, the maximum current density rating is achieved in the windings of all machines for a fair comparison. The IPM and IM design specifications are listed in Table 6.3.

(a)   (b)
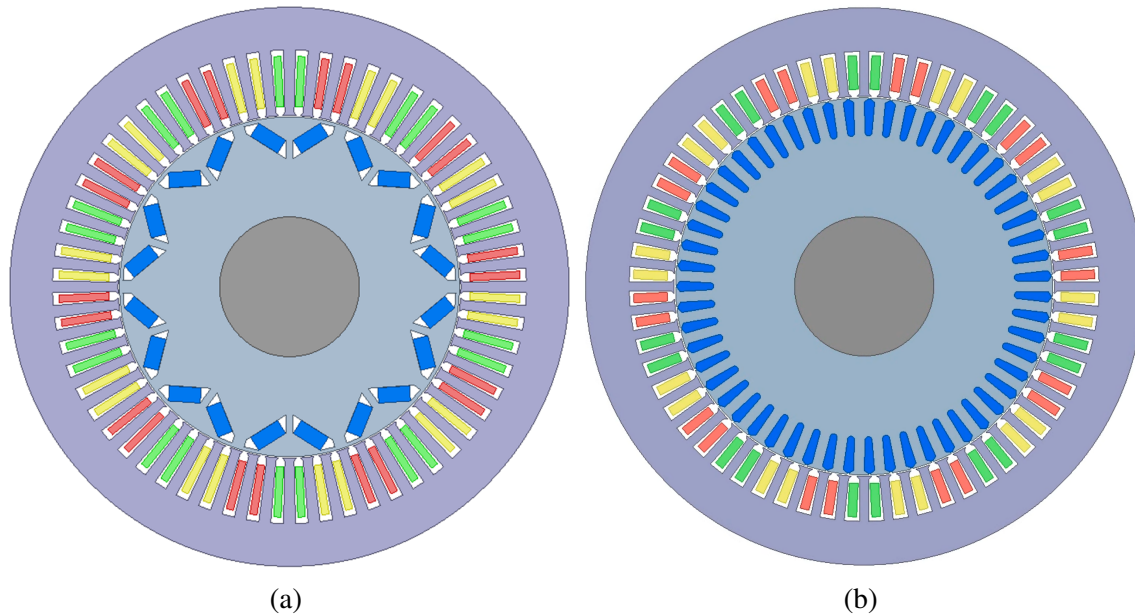
Figure 6.19: Cross sections of (a) IPM. (b) IM.

Fig. 6.20 compares the torque- and power-speed characteristics of the three machines under forced convection cooling conditions (i.e., J_{max} = 10 A$_{rms}$/mm^2). At low speeds, the proposed BSSFM performs similarly to the IM in the torque and power capabilities. However, the BSSFM

Table 6.3: Machine Specification of IPM and IM

	IPM	IM
Stator outer diameter (mm)	220	220
Rotor outer diameter (mm)	133.7	148.9
Shaft outer diameter (mm)	55	55
Core length (mm)	100	100
Air-gap length (mm)	0.6	0.6
Magnet dimensions (mm)	$12.5 \times 6 \times 100$	-
Turns per phase of stator winding	2	2
Number of poles of the machine	10	10
Phase numbers of the machine	3	3
Slot numbers - Stator	60	60
Slot numbers - Rotor	-	55
Slot packing factor	0.5	0.5
Type of Iron	M350-50A	M350-50A
Type of rotor bar conductor	-	Copper
Type of magnet	NdFe35	-

results in better performance than the IM above 3000 RPM with a CPWSR capability, showing the benefits of the capability of producing the rotor field using an independent spatial harmonic component.

In comparison to the IPM, the BSSFM produces lower peak torque due to the current density constraint imposed in the rotor windings, but shows comparable performance in both torque and power from the mid- to high-speed regions (above 4000 RPM). Moreover, the BSSFM shows a CPWSR capability similar to the IPM. It is also worth noting that the BSSFM is capable of operating at low torque levels and high speeds more efficiently by simply reducing the rotor field current, whereas the PM machine requires significant amounts of stator current for field weakening at high speeds, which reduces its efficiency.
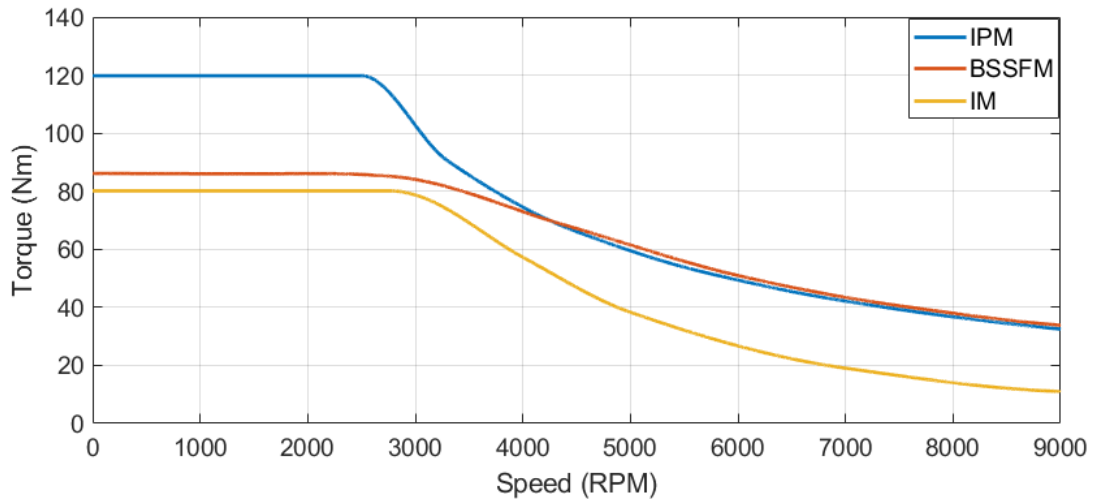
(a)
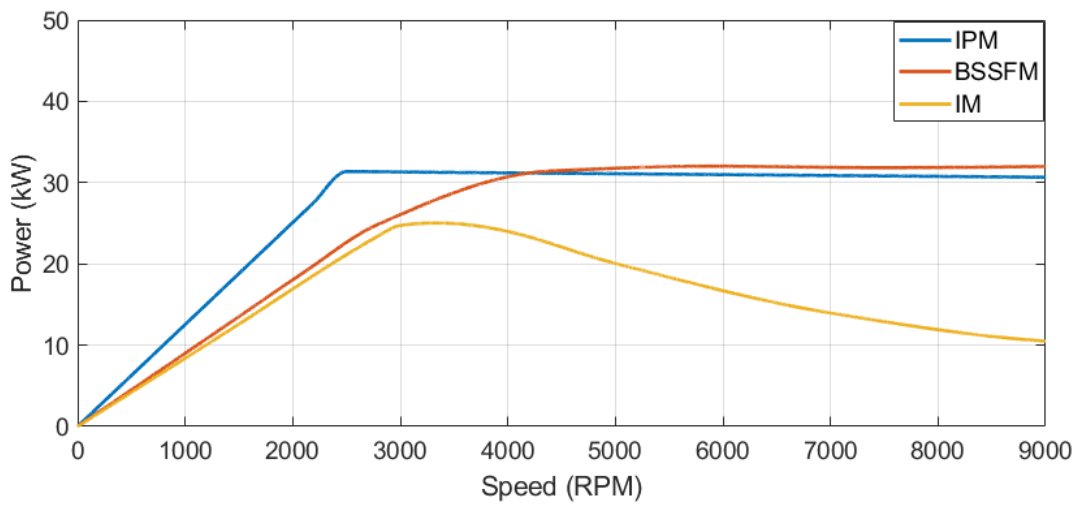
(b)

Figure 6.20: Torque- and power-speed characteristics of self-excited field winding machine and IM under forced convection condition. (a) Torque-speed. (b) Power-speed.

CHAPTER 7

Conclusion

7.1   Summary of Work and Contribution

This dissertation has presented a novel brushless excitation principle using independently controlled spatial harmonics and simulation results of two specific machine designs with a five-phase winding in the stator based upon the liquid and forced-air cooling specifications.

At the initial stage of this research, a procedure for modeling the proposed brushless machine topology was developed using the winding function theory to build a lumped-parameter model. Using the winding function approach, the self-inductances and mutual inductances of all machine windings were derived and used to establish a linear magnetic relationship of the flux-linkages and currents which incorporates the fundamental electromagnetic behaviors of the proposed machine topology. Using the modeling method, a linear magnetic model was developed as a simulation tool using a commercial software package of MATLAB and Simulink and used to validate the harmonic excitation scheme and develop several machine embodiments.

Next, a control algorithm was developed based upon the feedback control technique. Unlike conventional electric machines, the proposed brushless machine requires regulations of two sets of direct and quadrature stator currents corresponding to the two main spatial harmonic components to excite both the transformer and field windings in the rotor for the machine operations. To regulate these two sets of stator currents independently, specific Clarke and Park transformations for the five- or six-phase stator windings were developed. The established FOC-based current regulator

was implemented and tested in MATLAB and Simulink with a machine model for verification.

Using the MATLAB and Simulink tools, the machine operations of several embodiments and different winding designs were explored to characterize their effects on the performance of the proposed machine topology. Specifically, design parameters were investigated, such as the number of poles in all windings, distributed and concentrated winding designs, the number of phases for the rotor transformer, semiconductor materials (e.g., silicon-carbide diode) for the diode rectifier in the rotor, and harmonic couplings for all windings through spatial harmonic components. The simulation tools were used to set up an initial machine design quickly based upon the harmonic excitation principle and to establish the groundwork for further analyses and refinements using the FEA model.

In order to capture nonlinear machine behaviors, FEA models were developed using commercial software of ANSYS Electromagnetics Suite based upon the machine designs outlined in the previous step. The full machine designs were built using the ANSYS Maxwell 2D environment. The FEA diode rectifier model that was unique to the proposed machine topology was developed using ANSYS Circuit Design which was then combined with the Maxwell model.

Using the FEA simulation tools, machine designs were refined with a focus on geometric properties and performance parameters considering magnetic saturation. Based upon the FEA simulations, design iterations were performed by adjusting machine parameters, such as the number of poles, dimensions of the stator and rotor, air-gap length, the number of turns of all windings, and materials of the cores. For the excitation of the FEA model, the FOC-based current control schemes were used. The performance of the proposed machine was examined and validated by the specification of a comparably-sized permanent magnet machine. As a result of the design refinements, two machine designs were developed and their performances were investigated under both the liquid and forced-air cooling specifications.

7.2   Summary of Machine Performance and Designs

This dissertation has presented two machine designs of the brushless self-excited synchronous field-winding machine with a five-phase stator winding using independently controlled spatial harmonics. Simulation results of the two machine designs with respect to various performance metrics and different cooling specifications reveal the pros and cons of the two design approaches.

The machine design 1 has an advantage over the machine design 2 in terms of maximum torque capability and core utilization. In the liquid cooling condition, the machine design 1 achieved the maximum torque of 275 Nm which was 44% higher than that of the machine design 2. The transformer winding of this machine is wound on the dedicated cores that are separated from the main rotor core for the field windings, hence the magnetic flux loop by the transformer winding can be separated from the rotor field winding flux loop. Moreover, this design approach can optimize the geometric sizes of the transformer cores and the field-pole rotor cores separately, therefore achieving better core utilization of the machine.

However, the transformer winding of the machine design 1 had a difficulty in arranging it in a multi-phase configuration with a feasible rotor structure, leading to a single-phase transformer winding. With the single-phase transformer winding, the power transferring from the transformer to the torque became oscillatory, therefore resulting in a significant torque ripple. For instance, the peak-to-peak torque ripple at the base speed of 2779 RPM resulted in nearly 70% whereas the machine design 2 with a three-phase transformer winding achieved 15%. Moreover, the magnetic cores for the transformer winding brought a manufacturing concern regarding the fixture of these materials as they are physically separated from the main rotor core and not fixed to the main rotor structure.

The machine design 2 was created in order to resolve these issues in the machine design 1. The machine design 2 implemented a non-salient rotor and a typical winding slot shape for manufacturing ease. Furthermore, a three-phase transformer winding was used to reduce torque ripple significantly.

Although both issues were addressed in the design 2, this design approach showed a limitation

166

in terms of torque production under the liquid cooling condition. Inspection of the magnetic flux distributions revealed that the DC field current is constrained due to the magnetic saturation of the main torque-producing stator flux reducing the harmonic couplings of the transformer windings. Hence, the design 2 under liquid cooling condition results in the reduced peak torque performance compared to the design 1.

The MTPA test revealed that the second machine design achieved the peak torque capability at the current density of 10 A_{rms}/mm^2 which corresponds to the forced-air cooling condition. The FEA results showed that the proposed design achieved nearly 86 Nm of peak torque and 32 kW of output power under the forced convection cooling condition.

The performance of the BSSFM was compared to a similarly-sized IPM and IM under a similar design specification. Under forced convection cooling, the BSSFM revealed comparable torque production and power capability to the IM at low-speed ranges and performance close to the IPM from the mid- to high-speed ranges. The BSSFM showed the advantages of having the capability of an independent rotor field excitation better than IM topology as well as the CPWSR characteristic similar to PM topology, making the new design useful for variable-speed drive applications.

7.3 Future Work

The machine winding layout and magnetic core structure used in both machine designs are based on the standard distributed and concentrated winding for the stator and rotor for ease of manufacturability. This standard winding approach shows difficulties in maximizing the main spatial harmonic components and couplings with the rotor windings to achieve the peak torque performance close to the comparably-sized PM performance at the liquid cooling condition. To overcome these challenges, custom winding layouts and core structures for both the stator and rotor can be explored to improve the torque capability of this machine topology.

Additionally, for further reduction of the undesired couplings, an alternative winding approach can be exploited by removing a specific spatial harmonic component using a technique presented in Appendix 7.3.

The current transformer approach is based on the conventional inductive transfer which involves tuning a turning ratio between the stator and transformer windings. Simulation results showed that the generation of the DC field current in the field winding is affected by the total impedances of both the transformer and field windings and limited torque capability in certain operating conditions. The torque capability especially for the machine design 2 is reduced due to the reduced couplings of the transformer winding by the saturation of the torque-producing flux. Hence, a resonant transformer method, which requires less coupling, can be exploited in the rotor diode rectifier circuit to improve the efficiency of the transformer excitations and to increase the rotor field for better torque capability of the machine topology.

Lastly, the control strategy used for the proposed brushless machines is focusing on producing the peak torque performance at different operating speeds using the standard FOC-based synchronous current regulation approach with two sets of the direct- and quadrature-axis currents and the frequency associated with the transformer-exciting field. Therefore, optimal control strategies for various torque and speed operating points can be exploited to improve the machine efficiency.

APPENDIX

A Technique to Remove a MMF Spatial Harmonic Component using Pole Pitch Adjustment

Brushless operations of the proposed machine rely on spatial harmonic couplings between the stator winding and the two rotor windings. These couplings of the spatial harmonics occur when both MMF waveforms of the stator and the rotor windings have a common spatial harmonic. For example, when the stator MMF and the transformer MMF contain the third spatial harmonic component, the coupling occurs at this spatial harmonic and induces voltage in the transformer winding. Therefore, these common spatial harmonics between all windings are important in the operation of the proposed brushless scheme since they can create undesired harmonic couplings and cause saturation by increasing magnetic flux densities within the machine cores and torque ripples. Hence, reducing some of these undesired couplings could mitigate these negative effects and improve overall performance. In this section, a technique to reduce a spatial harmonic component in an MMF is introduced through optimization of the pole pitch of a winding.

The magnitudes of a spatial harmonic in an MMF are determined by the winding coefficients of the corresponding winding function. To demonstrate the technique, a winding function of phase-a of a five-phase stator winding in Equation (4.1) is considered. Without optimization of the pole pitch of the stator winding (e.g., $\epsilon = \frac{\pi}{6}$), the total MMF waveform of the five-phase stator windings and the spatial harmonic contents can be visualized in Figure 1.

It can be easily seen that the fundamental (first) and third spatial harmonics are the main spatial harmonics used for the operation of the proposed machine. Hence, the seventh spatial harmonic

Figure 1: Stator MMF and spatial harmonics. (a) Total stator MMF waveform. (b) Spatial harmonic contents using pole pitch of $\epsilon = \frac{\pi}{6}$

component in the stator MMF is redundant and can be removed by using a specific pole pitch as follows:

$$k_{s7} = \frac{sin(\frac{7\epsilon}{2})}{\frac{7\epsilon}{2}} = 0. \tag{1}$$

Hence, when ϵ is $\frac{2\pi}{7}$, the seventh spatial harmonic component in the stator MMF becomes zero eliminating a potential harmonic coupling with the rotor winding. The new resulting total MMF waveform of the stator winding and its spatial harmonic content is shown in Figure 2. The seventh spatial harmonic component is removed by using $\epsilon = \frac{2\pi}{7}$. This method can be also applied to other harmonic components in the rotor windings for further design optimizations.
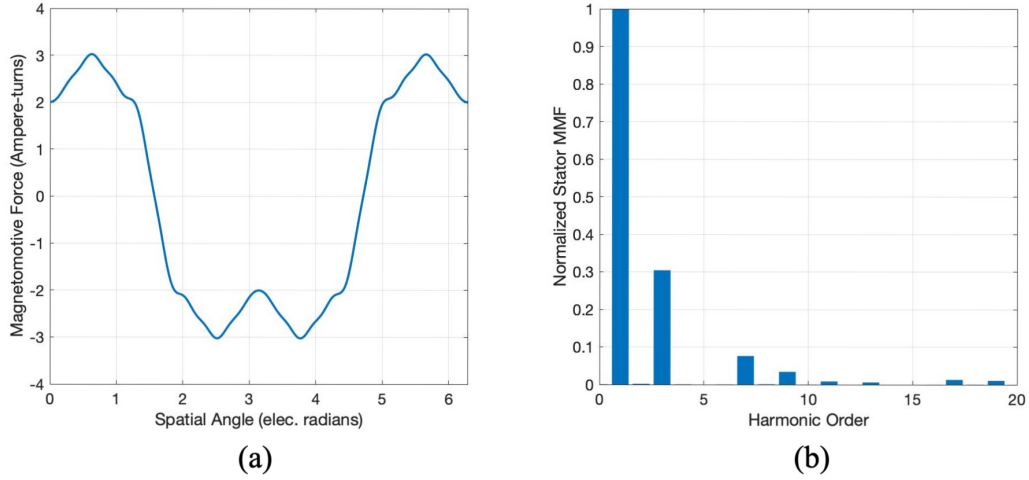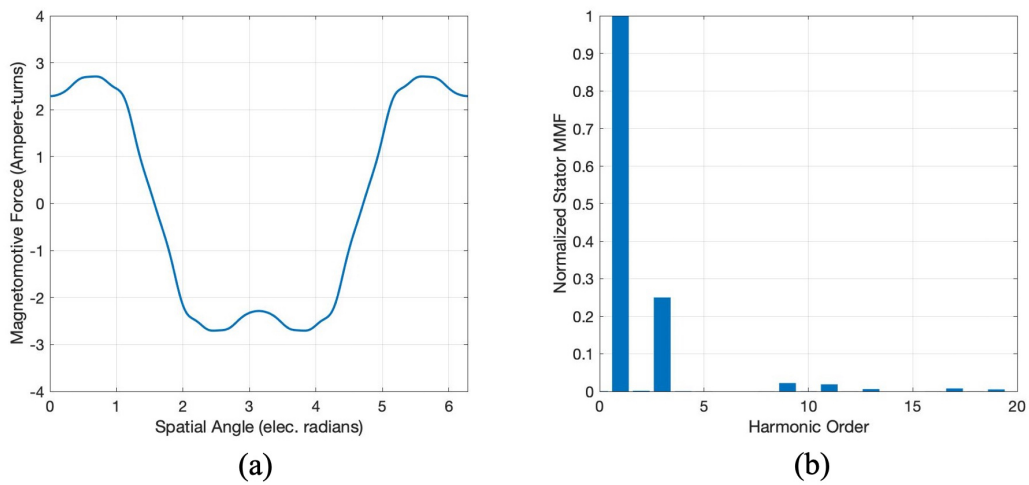
Figure 2: Stator MMF and spatial harmonics. (a) Total stator MMF waveform. (b) Spatial harmonic contents using pole pitch of $\epsilon = \frac{2\pi}{7}$

BIBLIOGRAPHY

[1] Jacek F. Gieras. *Electrical Machines: Fundamentals of Electromechanical Energy Conversion*. CRC Press.

[2] J. C. Michalowicz. Origin of the electric motor. *Electrical Engineering*, 67(11):1035–1040, 1948.

[3] V. V. Athani. *Stepper Motors : Fundamentals, Applications And Design*. New Age International (P) Ltd.

[4] Polytechnic Hub. Construction of 3-phase induction motor. `https://www.polytech nichub.com/construction-3-phase-induction-motor/`, 2018.

[5] Heath Hofmann. *Electric Machinery and Drives (Draft)*.

[6] Y. Guan, Z. Q. Zhu, I. A. A Afinowi, J. C. Mipo, and P. Farah. Comparison between induction machine and interior permanent magnet machine for electric vehicle application. In *2014 17th International Conference on Electrical Machines and Systems (ICEMS)*, pages 144–150, 2014.

[7] T. Matsuo and T.A. Lipo. Rotor design optimization of synchronous reluctance machine. *IEEE Transactions on Energy Conversion*, 9(2):359–365, 1994.

[8] K. Chau, W. Li, and C. H. Lee. Challenges and opportunities of electric machines for renewable energy. *Progress In Electromagnetics Research B*, 42:45–74, 2012.

[9] Tim Treadgold. Share Prices Rocket As The Rare Earth Rush Is Rebooted, 2020.

[10] D. Vindel, S. Haghbin, A. Rabiei, O. Carlson, and R. Ghorbani. Field-oriented control of a pmsm drive system using the dspace controller. In *2012 IEEE International Electric Vehicle Conference*, pages 1–5, 2012.

[11] R. Dutta, L. Chong, and M. F. Rahman. Analysis of CPSR in motoring and generating modes of an IPM motor. In *2011 IEEE International Electric Machines Drives Conference (IEMDC)*, pages 1474–1479, 2011.

[12] Kollmorgen. Four quadrant operation. `https://www.kollmorgen.com/en-us/de veloper-network/four-quadrant-operation/`, 2018.

[13] A.M. EL-Refaie and T.M. Jahns. Comparison of synchronous pm machine types for wide constant-power speed range operation. In *Conference Record of the 2005 IEEE Industry Applications Conference*, volume 2, pages 1015–1022, October 2-6, 2005.

[14] Research and Markets. Global permanent magnet motor market. https://www.researchandmarkets.com/reports/5332727/global-permanent-magnet-motor-market-by-type, 2021.

[15] A.K. Adnanes, R. Nilssen, and R.O. Rad. Power feed-back during controller failure in inverter fed permanent magnet synchronous motor drives with flux weakening. In *PESC '92 Record. 23rd Annual IEEE Power Electronics Specialists Conference*, pages 958–963 vol.2. IEEE, 1992.

[16] S. Han, T. M. Jahns, M. Aydin, M. K. Guven, and W. L. Soong. Impact of maximum back-emf limits on the performance characteristics of interior permanent magnet synchronous machines. In *Conference Record of the 2006 IEEE Industry Applications Conference Forty-First IAS Annual Meeting*, volume 4, pages 1962–1969, 2006.

[17] Strategic Metals Invest. Rare earth element and technology metals prices 2017 to 2022. https://strategicmetalsinvest.com/5-year-prices/, 2022.

[18] G.F.H. Allen. Brushless excitation systems for synchronous machines. *Electronics and Power*, 21(15):866–869, 1975.

[19] A. Griffo, R. Wrobel, P. H. Mellor, and J. M. Yon. Design and characterization of a three-phase brushless exciter for aircraft starter/generator. *IEEE Transactions on Industry Applications*, 49(5):2106–2115, 2013.

[20] Joseph Vithayathil. AC machine system with induced dc field, 1991.

[21] S. Nonaka. A new brushless excitation method for 4-pole three-phase synchronous generator with cylindrical-rotor. In *Proceedings of 1994 IEEE Industry Applications Society Annual Meeting*, volume 1, pages 23–30 vol.1. IEEE, 1994.

[22] Joseph Vithayathil. Brushless exciterless field system for ac synchronous machines, 2000.

[23] S. S. H. Bukhari, G. J. Sirewal, M. Ayub, and J. S. Ro. A new small-scale self-excited wound rotor synchronous motor topology. *IEEE Transactions on Magnetics*, 57(2):1–5, 2021.

[24] S. S. H. Bukhari, M. A. Shah, J. Rodas, M. Bajaj, and J. S. Ro. Novel sub-harmonic-based self-excited brushless wound rotor synchronous machine. *IEEE Canadian Journal of Electrical and Computer Engineering*, 45(4):365–374, 2022.

[25] M. Aoyama, M. Saito, T. Mizuta, Y. Miyama, and K. Ito. Proposal of novel line-start type self-excited wound-field synchronous motor with three-phase concentrated winding stator. *IEEE Open Journal of Industry Applications*, 1:236–247, 2020.

[26] M. Aoyama, M. Saito, T. Mizuta, Y. Miyama, and K. Ito. Experimental verification with loads of line-start type self-excited wound-field motor with three-phase concentrated winding stators. *IEEE Transactions on Energy Conversion*, 36(2):1234–1244, 2021.

[27] D. C. Ludois, J. K. Reed, and K. Hanson. Capacitive power transfer for rotor field current in synchronous machines. *IEEE Transactions on Power Electronics*, 27(11):4638–4645, 2012.

[28] A. Di Gioia, I. P. Brown, Y. Nie, R. Knippel, D. C. Ludois, J. Dai, S. Hagen, and C. Alteheld. Design and demonstration of a wound field synchronous machine for electric vehicle traction with brushless capacitive field excitation. *IEEE Transactions on Industry Applications*, 54(2):1390–1403, 2018.

[29] S. Nonaka and T. Kawaguchi. Excitation scheme of brushless self-excited-type three-phase synchronous machine. *IEEE Transactions on Industry Applications*, 28(6):1322–1329, 1992.

[30] S. Nonaka and T. Kawaguchi. A new variable-speed ac generator system using brushless self-excited type synchronous machine. In *Conference Record of the 1990 IEEE Industry Applications Society Annual Meeting*, pages 691–696 vol. 1. IEEE, 1990.

[31] K. Inoue, H. Yamashita, E. Nakamae, and T. Fujikawa. A brushless self-exciting three-phase synchronous generator utilizing the 5th-space harmonic component of magneto motive force through armature currents. *IEEE Transactions on Energy Conversion*, 7(3):517–524, 1992.

[32] C. Lin, M. Pathmanathan, P. Rodriguez, F. Bertoldi, M. A. Kabir, T. Janhunen, and P. Paloheimo. Self-excited synchronous machine using airgap harmonics. *IEEE Transactions on Industrial Electronics*, 68(8):6584–6594, 2021.

[33] A. Rovnan and H. Hofmann. Brushless, self-excited synchronous field-winding machine for variable-speed drive applications. *2006 International Conference on Electric Machines, Chania, Crete Island, Greece*, Paper No. 702, 2006.

[34] A. Zeynu and H. Hofmann. Design of field-oriented-control-based brushless, self-excited synchronous field-winding machine with combined finite element/rectifier model. In *2017 IEEE Energy Conversion Congress and Exposition (ECCE)*, pages 1830–1837, 2017.

[35] Lizhi Sun, Xiaolong Gao, Fei Yao, Quntao An, and Thomas Lipo. A new type of harmonic current excited brushless synchronous machine based on an open winding pattern. In *2014 IEEE Energy Conversion Congress and Exposition (ECCE)*, pages 2366–2373, 2014.

[36] L. Parsa. On advantages of multi-phase machines. In *31st Annual Conference of IEEE Industrial Electronics Society, 2005. IECON 2005.*, pages 6 pp.–, 2005.

[37] S. Sadeghi, L. Guo, H. A. Toliyat, and L. Parsa. Wide operational speed range of five-phase permanent magnet machines by using different stator winding configurations. *IEEE Transactions on Industrial Electronics*, 59(6):2621–2631, 2012.

[38] H. Xu, H.A. Toliyat, and L.J. Petersen. Rotor field oriented control of five-phase induction motor with the combined fundamental and third harmonic currents. In *APEC 2001. Sixteenth Annual IEEE Applied Power Electronics Conference and Exposition (Cat. No.01CH37181)*, volume 1, pages 392–398 vol.1, 2001.

[39] L. Parsa and H.A. Toliyat. Five-phase permanent-magnet motor drives. *IEEE Transactions on Industry Applications*, 41(1):30–37, 2005.

[40] T.A. Lipo. *Analysis of Synchronous Machines*. CRC Press.

[41] V. Kindl, Z. Ferkova, and R. Cermak. Spatial harmonics in multi-phase induction machine. In *2020 ELEKTRO*, pages 1–4, 2020.

[42] F. Yao, Q. An, X. Gao, L. Sun, and T.A. Lipo. Principle of operation and performance of a synchronous machine employing a new harmonic excitation scheme. *IEEE Transactions on Industry Applications*, 51(5):3890–3898, 2015.

[43] Z. Liu, Y. Li, and Z. Zheng. A review of drive techniques for multiphase machines. *CES Transactions on Electrical Machines and Systems*, 2(2):243–251, 2018.

[44] C. Kral, A. Haumer, and R. Whrnschimmel. Extension of the fundamentalwave library towards multi phase electric machine models. pages 135–143, 03 2014.

[45] C. Odeh, D. Kondratenko, A. Lewicki, and A. Jaderko. Modified spwm technique with zero-sequence voltage injection for a five-phase, three-level npc inverter. *Energies*, 14(4):1198, 2021.

[46] B. Prieto, M. Martínez-Iturralde, L. Fontán, and I. Elosegui. Analytical calculation of the slot leakage inductance in fractional-slot concentrated-winding machines. *IEEE Transactions on Industrial Electronics*, 62(5):2742–2752, 2015.

[47] H. Song and H. Hofmann. Robust, accurate systems-based power electronic circuit models in simulink. In *2018 IEEE 19th Workshop on Control and Modeling for Power Electronics (COMPEL)*, pages 1–8, 2018.

[48] Y. Yang, B. Bilgin, M. Kasprzak, S. Nalakath, H. Sadek, M. Preindl, J. Cotton, N. Schofield, and A. Emadi. Thermal management of electric machines. *IET Electrical Systems in Transportation*, 7(2):104–116, 2017.

[49] M. Olszewski et al. Evaluation of the 2010 toyota prius hybrid synergy drive system. *Oak Ridge Nat. Lab., US Dept. Energy*, 2011.